Influence of the inter-annual variability of snow physical properties on the ground thermal regime - through observations and modelling (Samoylov Island, Siberia)

Julia Martin (4523900)

Berlin, July 22, 2022

Master's thesis

Department Geoscience
University of Bremen
Supervision: Prof. Dr. Julia Boike
1. Reviewer: Prof Dr. Olaf Eisen
2. Reviewer: Prof Dr. Katrin Huhn-Frehers

Abstract

Automated measurements of snow physical properties in the remote Arctic are scarce, which poses a challenge not only for the investigation of the snow cover evolution throughout the season and years, but also for climate and permafrost modelling, as snow is a crucial parameter for the ground thermal regime. Here, I present the first-time analysis of a sophisticated automated snow measurement data set which was obtained in a Low Centre Polygon (LCP) complex on Samoylov Island, a permafrost site in the Lena River Delta, Siberia.

My work focused on analysing the inter-annual variability and seasonal evolution of the snow physical properties depth, density and temperature. I investigated the influence of on the ground thermal regime as well as snow-soil interactions within a time period of four years from 2014 to 2018.Furthermore, I used the data to validate the new ‹CryoGrid (CG) Community› version of the CG permafrost model for Samoylov Island with regard to the snow physical properties.

My processing routine included the quality check of the snow depth, snow temperatures as well as density time series and I compared the automated measurements with field observations to evaluate the sensor performances. Furthermore, I generated ‹CG Community› model runs with two versions of the Crocus snow scheme (Standard and Arctic) to validate the models' ability to reproduce the snow and ground thermal regime for the time span of the observations (2014 to 2018).

My results revealed great inter-annual variations in the snow cover extent and internal layering of the snowpack on Samoylov Island within the analysed time period. I found a great spatial variability of the snow depth, which was depended on the micro-topography of the LCP complex. The mean end-of-season (EOS) snow depth was the highest in the polygon centre (0.46 to 0.74 m) and the lowest on the polygon rims (0.32 and 0.53 m). The EOS density for the snowpack up to 0.3 m in the polygon centre was between 204 and 236 kg m^{-3}. The snowpack was characterized by the typical Arctic stratigraphy, consisting out of a basal low density layer (depth hoar) overlain by layers with a higher density (wind slab). The ratio of these layers was connected to the snow cover build-up from October to November, especially the timing and intensity of snowfall. The depth hoar layer evolution started in the early snow season in December and took place until January. It showed a connection to the soil freeze-back, as it was a concomitant of the decrease in soil volumetric water content. The density profile, especially the depth hoar fraction, showed a yearly variability which impacted the ground thermal regime.

A higher depth hoar layer thickness (about 0.15 m) was accompanied by stronger ground cooling compared to a year with lower depth hoar layer thickness (about 0.05 m).

The ‹CG Community› simulations were able to generate the snow depth variability and evolution. The simulations could not reproduce the measured density profile and had difficulties to generate its high inter-annual and seasonal variability. I found the results of the ‹CG Community› simulations using the Standard Crocus snow scheme to be in better agreement with the automated measurements on Samoylov Island. In combination with the Arctic Crocus snow scheme, the ‹CG Community› model run showed an underestimation of snow depth due to wind effects, which led to an overcompaction of the snowpack. Furthermore, the model runs revealed a high sensitivity to the snowfall rate in the forcing data.

My work highlights the complexity of the snowpack and how its inter-annual variability influences the ground thermal regime. I provide a validation of the ‹CG Community› model and outline the need to improve the implementation of snow physical processes in snow schemes and snow-soil models, respectively.

Acknowledgements

My deep gratitude goes to Julia Boike, who allowed me to learn, work and grow with the AWI Permafrost group in Potsdam. I am thankful for her beliefs in me and her ongoing support. I would also like to thank Sebastian Westermann who always answered my countless CG questions with a smile.

Furthermore, I acknowledge my colleagues and friends with whom I experienced those great adventures in the Arctic/office and who always stood by my side. A special thanks goes to Fred, Bill and Brian, who endured my writing journey and did not stop to add valuable comments (even though commenting in overleaf is painful). Thank you Inge, for the emergency rescue.

I want to thank Olaf Eisen and Katrin Huhn-Frehers for providing the reviews of my thesis.

Last but not least, I am grateful and humbled to have the unconditional support of my family.

Mom. I could not have done it without your limitless supply of love and pizza and patience.

Contents

List of Figures

List of Tables

List of Abbreviations

CG	CryoGrid
LCP	Low Centre Polygon
VWC	Volumetric Water Content
SPA-2	Snow Pack Analysing System
SWE	Snow Water Equivalent
PE	PolyEthylene
EOS	End-Of-Season
TDR	Time-Domain Reflectometry
ALTD	Active Layer Thaw Depth
RMSE	Root Mean Squared Error
MBE	Mean Bias Error

1 Introduction

Permafrost, defined as the ground domain (soil, sediments, rocks) which remains at or below 0 ℃ for at least two consecutive years (Van Everdingen, 1998) covers about 11 % of the total surface of the Earth's exposed land surface (Obu, 2021). It is a major component (Fig. 1) of the Northern Hemisphere (Zhang et al., 2008). It is globally experiencing an increase in temperatures (Biskaborn et al., 2019) as climate conditions are changing more rapidly in polar and high elevation regions (Pepin et al., 2015). Permafrost is a very sensitive system (Jorgenson et al., 2010) and its thaw has a huge impact on the Arctic ecosystem and its inhabitants. Alongside destabilization processes due to surface subsidence and slope instability (Osterkamp et al., 2009), changes also have great impact on wildlife and vegetation habitats (Sturm et al., 2001). Furthermore, permafrost acts as a positive feedback mechanism due to the emission of greenhouse gases (Burke et al., 2017).

A major consequence of thawing ice-rich permafrost is ground subsidence. When permafrost degrades, or ground ice thaws, the earth above the ground surface will subside due to the volume reduction of ice to water or lateral export of melt water. This process is called thermokarst, and it involves the formation of characteristic landforms (Olefeldt et al., 2016). A prominent type of thermokarst throughout the arctic is the ice-wedge degradation in the polygonal tundra leading to four degradation-specific polygon types: high-centered polygons with drained troughs or water-filled troughs, high-centered polygons with water-filled troughs and low-centered troughs with wet or water-filled centres (Nitzbon et al., 2019).

Permafrost thaw and the associated degradation types are influenced by a number of parameters such as the soil composition, the vegetation cover, hydrological features and the snow cover (Grünberg et al., 2020; Boike et al., 2021) and hence, to understand and model the permafrost thermal regime is a major research task. To do so, it is not only necessary to directly equip vital locations with observational instruments, but also to enable modelling.

In terms of climate modelling, snow is a crucial but complex variable. The snow mass is influenced by different drivers such as temperature, precipitation, sublimation as well as wind redistribution (Mudryk et al., 2020; Clark et al., 2011) and snow schemes lack

---

[1] `https://www.grida.no/resources/13519` [accessed:2022-06-27]

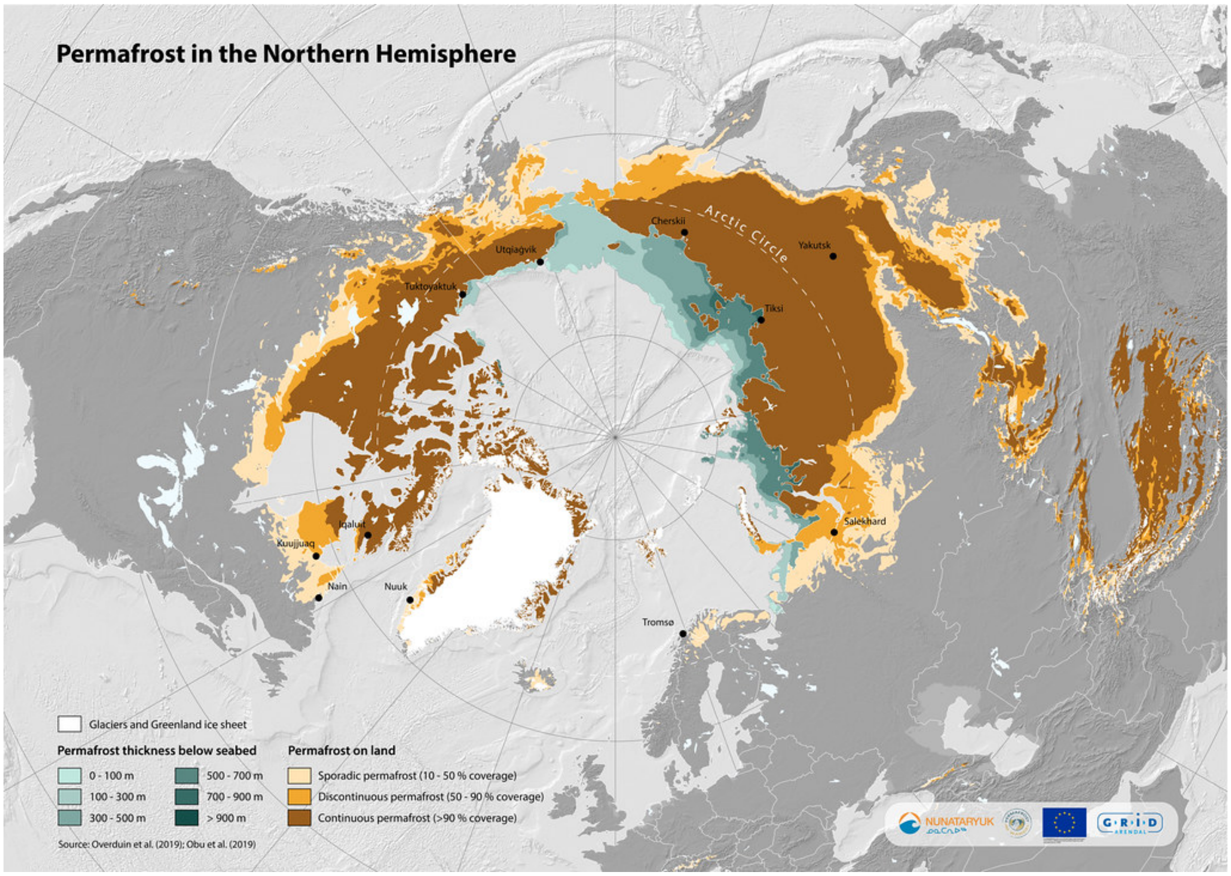

Figure 1: Circumpolar permafrost distribution map (GRID-Arendal/Nunataryuk 2020[1]). Modelled mean annual ground temperatures at the top of the permafrost for the Northern Hemisphere, based on Obu et al. (2019); Overduin et al. (2019).

the correct implementation of micro-structural processes e.g. inverted density gradients and more often use a parameterization approach (Krinner et al., 2018). Altogether, predictions about the extent and duration of the snow cover show higher confidence than predictions about the snow depth and Snow Water Equivalent (SWE) trends (Meredith et al., 2019).

A commonly used permafrost model (including the snow cover) is the land-surface model CryoGrid (CG) 3 published by Westermann et al. (2016), which was recently updated with the ‹CG Community› version (Westermann et al., 2022). The ‹CG Community› model simulates heat conduction and freeze-thaw processes with the upper boundary condition given by the surface energy balance.

Several improvements to the ‹CG Community› snow scheme were implemented in the recent past, including snow distribution processes (Nitzbon et al., 2021; Zweigel et al., 2021; Nitzbon et al., 2020). Also, the ‹CG Community› model was combined with the snow parameterization from the Crocus snow scheme (Vionnet et al., 2012) for a site on the Svalbard archipelago (Zweigel et al., 2021), which led to a better performance and adaptability to different landscapes. Despite the crucial role of the snow cover for the permafrost thermal state, numerical models still require large advancements (Langer et al., 2013). As revealed by a number of authors, the snow cover exerts a fundamental control on the thermal and hydrological regime of permafrost. Snow acts as an insulator thanks to its low effective thermal conductivity, reducing heat loss in winter (Zhang, 2005; Grünberg et al., 2020).

The amount of heat transferred through the snowpack varies depending on the microstructure, e.g. texture and physical properties such as density and wetness (Sturm and Johnson, 1992; Gouttevin et al., 2012). In spring, snow strongly reflects the solar radiation (i.e. a high albedo) (Stiegler et al., 2016) and the duration and extent of the snow cover regulates the soil temperature and melt-water supply (Boike et al., 2003). Despite large improvements of snow permafrost modelling, a current challenge is the implementation of the complex Arctic snow cover characteristics, such as basal ice layer formation, wind induced crusts/slabs development and especially the formation of basal depth hoar layers. The depth hoar layer properties lead to severe temperature differences in the ground thermal regime and also influence the freeze-back period (Zhang et al., 1996).

These Arctic snow cover characteristics result in a distinguished snow stratigraphy which is a composition of basal depth hoar overlain by wind slab (Domine et al., 2002, 2012; Sturm and Benson, 2004) as shown in Fig.2. This setup divides the snowpack into two layers, each having very different formation processes and physical properties. Wind slabs are dense, cohesive snow layers consisting out of wind packed rounded grains which are well-sintered (Fierz et al., 2009). The depth hoar layer formation is connected to the strong temperature gradient which occurs between the snow surface (in contact with the cold winter air) and the snowpack's base (directly above the warmer ground) as described in detail by Domine et al. (2018).

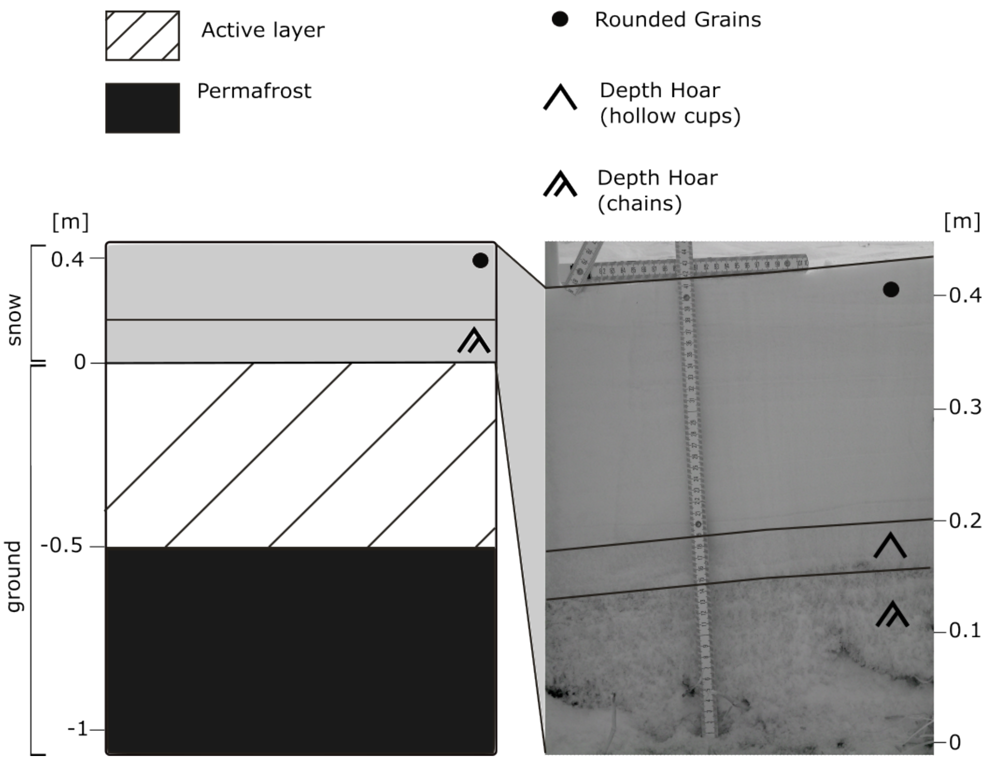

Figure 2: Cross-section for Arctic snowpack setup with basal depth hoar layer (hollow cups and depth hoar chains) and wind slab on top and ground domain underneath. Symbols for the grain types, follow Fierz et al. (2009). The active layer is the part of the soil which experiences seasonal thawing and freezing. Depth in [m]. The picture was taken during the Lena Spring campaign in April 2019 (Fuchs et al., 2021).

The temperature gradient induces a water vapour gradient which leads to sublimation at the top of snow crystals. The upward flux forces the water vapour to condense on the base of snow crystals above. As a result, larger, faceted, often hollow grains start to grow at the bottom of the snowpack (Zyungo Yosida, 1955). The soil moisture impacts the temperature gradient and with that the depth hoar formation (Davesne et al., 2021). On the one hand, the soil moisture determines the cooling behaviour of the ground and with that directly influences the strength of the temperature gradient in the snowpack. On the other hand, the temperature gradient between the basal snow and the ground can induce mass transfer from the soil profile to the snow, as described by Woo (1982) and Smith and Burn (1987).

The required thermal conditions for depth hoar formation primarily exist during the early snow season, and hence depth hoar is most prominent at the base of the snowpack. However, according to Domine et al. (2002) depth hoar layers are sometimes observed in the upper layers of the snowpack, and are typically called indurated depth hoar (Fierz et al., 2009). Furthermore, depth hoar layers highly vary in terms of thickness, texture and physical properties depending on the initial snow structure and undergo metamorphism during the entire snow season (Sturm and Benson, 1997). Depth hoar has a low thermal conductivity which makes the basal layer the most important insulator in terms of the ground thermal regime (Zhang et al., 1996). In contrast, wind slabs have a higher thermal conductivity consisting of closely packed, small rounded grains (Fierz et al., 2009).

Reproducing the snow physical properties e.g. the correct Arctic snowpack stratification can be difficult, even for dedicated snow models such as Crocus (Vionnet et al., 2012) and SNOWPACK (Bartelt and Lehning, 2002). They are particularly designed for modelling snow processes (Domine et al., 2019) but initially developed to reproduce the alpine snow cover properties with nominal upward water vapour flux. However, coupled snow-soil models can still show a strong performance for the soil thermal regime (Barrere et al., 2017) but this is most probably only bound to a good error compensation. Hence, there are recent efforts to improve the Crocus snow scheme by changes in the parameterization to better represent Arctic Conditions (Royer et al., 2021b).

In general, validating model performance is difficult as the remote character of the Arctic makes it challenging to measure and monitor snow and permafrost properties on a long-term scale and only a few such data sets are available (Boike et al., 2019). Furthermore, most detailed snow studies are carried out in Northern America and Europe and only a few accessible surveys of the snow physical properties in the Russian Arctic have been performed to date.

A detailed snow study using field data and resulting improvements for the SNOWPACK snow scheme (Bartelt and Lehning, 2002) was carried out in Siberia by Gouttevin et al. (2018). Their investigations showed a high spatial variability in snow physical properties depending on the polygonal micro-topography. They found snow depth to be more extensive on slopes and centres compared to rims and snow stratigraphy was characterized by a layer of basal depth hoar with faceted grains (mean density of $236\,\mathrm{kg\,m^{-3}}$) and wind slab layers on top (mean density of $356\,\mathrm{kg\,m^{-3}}$). However, the study was conducted during April in 2013 and no data about the snow physical properties in the Siberian Arctic have been published since then in the English literature. The lack of long-term observations of snow physical properties and the limited number of validation approaches, especially for the ‹CG Community› model, are the main motivations of this study.

My thesis aims to answer the questions, **how the snow physical properties affect the permafrost thermal regime in the high Arctic in northern Siberia** and **whether the current ‹CG Community› model is able to resolve those effects**. Thus, the objectives of my thesis are the following:

[1] To quantify the inter-annual snow cover variability at a Siberian permafrost site in terms of snow depth and density and the thermal profile for the years 2014 to 2020 with respect to long-term data series (2002 to 2017).

[2] To evaluate the performance of the ‹CG Community› model regarding its ability to realize the snow cover for a Siberian permafrost site and compare the performance to the field and automated measurements of the snow physical properties.

2 Data and methods

2.1 Study site

Northern Siberia is characterized by continuous permafrost (Fig.1) and has the largest river delta in the Arctic, the Lena River Delta (Fig.3 (a)). The Lena River is one of the longest rivers in the world and its' source is located in southern Russia.

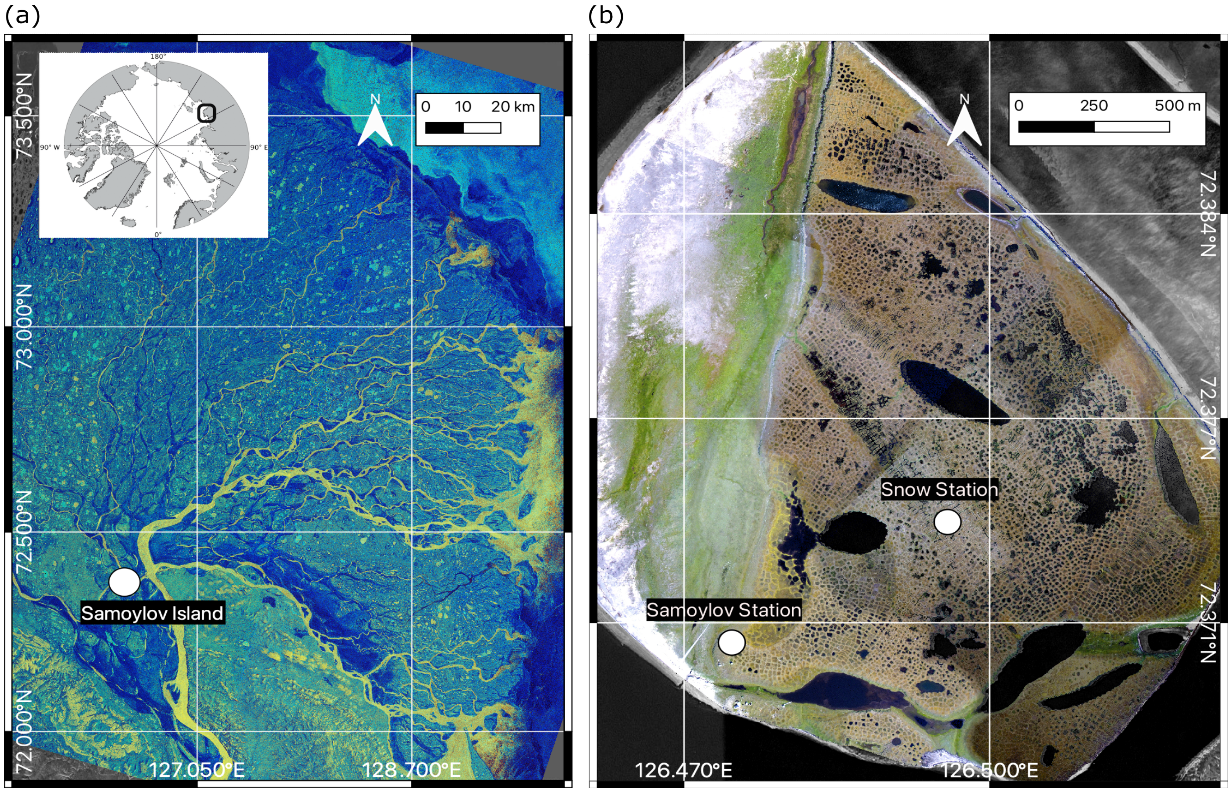

Figure 3: (a) false-colour image of the Lena River Delta taken on 14 January 2014 (Copernicus Sentinel-1 ESA[2]). (b) Aerial image (Muster et al., 2012) from 2007 of Samoylov Island with the research station (Samyolov station) located in the south-western part near the shore and the snow measurement station (snow station) located in the middle of the island in the wet polygon zone.

The river stretches about 4500 km and discharges into the Arctic Ocean, providing the main sediment input for the Laptev Sea (Are and Reimnitz, 2000). The Lena River Delta is a very fertile wetland during the short polar summer period and is a vital oasis for wildlife. Geomorphologically the delta can be separated into three river terraces

---

[2] `https://www.esa.int/ESA_Multimedia/Images/2019/06/Lena_River_Delta`accessed:2022-06-27]

(Grigoriev, 1993).

The first one (1-12 m a.s.l.) is the largest in area, dominating the central and eastern parts of the delta. The landscape is characterized by active floodplains, ice-wedge polygonal tundra and large thermokarst lakes (Schwamborn et al., 2002). It is the youngest and originated in the mid-Holocene (Schneider et al., 2009). Located on the first terrace in the south-western part of the delta, in one of the four main channels, is the Samoylov Island permafrost observatory (Fig.3 (b)). The second terrace (20-30 m a.s.l.) is in the north-western part of the delta and originated in the late Pleistocene to early Holocene (Schneider et al., 2009). It is characterized by large sand deposits with lower ice content and large thermokarst lakes. The southern part of the delta is dominated by the third terrace (30-55 m a.s.l.) which also is the oldest of the three (Late Pleistocene). Here, the ‹Yedoma Ice Complex› can be found (Schwamborn et al., 2002). It is an ice-rich and organic bearing type of permafrost deposit consisting out of tens of meters thick sediments interspersed with large ice-wedges and high amounts of excess ice.

2.1.1 Permafrost landscape

The main landscape features on Samoylov Island are the active flood plain in the western part and the river terrace in the eastern part of the Island (Boike et al., 2013). The latter is patterned by polygonal tundra with dry rims and wet depressed centres and troughs (Fig.4). The pattern ground of the polygonal tundra has its origin in thermal contraction processes. It starts with ground cracking in winter due to very low temperatures. This takes place in the active layer (part of the soil which experiences seasonal thawing and freezing) but also in the permafrost. In spring, melting snow and surface water collect in the cracks. It freezes and ice-wedges form. In the permafrost, these ice-wedges remain frozen throughout the summer. With yearly repetition their volume increases which leads to heaving and the development of the micro-topographic features rims, trough and centres of the polygonal tundra (Mackay, 2000).

Polygonal tundra is divided in dry and wet tundra depending on water saturation. Depressions such as LCP and the evolving water bodies are classified as wet tundra, whereas elevated features such as rims and high centre polygons are dry tundra features (Boike et al., 2013). Water filled polygon centres (polygonal ponds) are spread all over the island but large thermokarst water bodies dominate in terms of surface

Figure 4: Snow station located 72° 22.452′ N and 126°29.753′ E expanding over two wet, low-center polygons. The dark brown colour indicates moist regions in the micro-topography (centres and troughs) with sedges accompanied by mosses being the dominant vegetation types. In total, there are ten snow depth sensors mounted on a 15 m metal bar. The white squares are the aluminium target plates underneath each sensor to reduce the data noise produced by sedges. The smaller station in the east is the soil station located at 72° 22.451′ N and 126°29 757′ E. The two stations are accessible by wooden boardwalks. This aerial picture was taken in July 2015 as part of the study done by Schennen et al. (2016).

area (Boike et al., 2013). Thermokarst lakes form due to thawing of ice-rich permafrost and subsequently occurring subsidence (Jorgenson and Shur, 2007). Those landscape transitions are connected to the degradation state of the polygons and permafrost, respectively (Nitzbon et al., 2019).

On Samoylov Island, permafrost extends up to 400 to 600 m deep (Yershov et al., 1991) and can be found on Samoylov within the upper 1 m depth. The soil domain in permafrost environments is characterized by the ‹zero-curtain period› which describes the time when the soil domain has an almost constant temperature close to the freezing point, whereas the air temperature drops (Outcalt et al., 1990). This happens due to the delayed phase transition from water to ice because of latent heat release. It occurs during the freezing and thawing and is linked to the soil physical properties such as moisture content and texture.

2.1.2 Soil and vegetation

The soil profile which can be found on first terrace (Late Holocene) on Samoylov Island consists of alternating silt and sand layers with varying organic content (Boike et al., 2013) and is attributable to the mixture of aeolian and fluvial sediment input. Following the ‹US Soil Taxonomy[3]› the dominate soil types are the cryoturbated, permafrost-effected *Glacic Aquiturbel* common for permafrost soils as well as the non-cryoturbated, permafrost-effected and organic-rich *Typic Hostorthel* (Zubrzycki et al., 2013). The active floodplain in the western part of the island is characterized mainly by fluvial sedimentation and the soil type is the non-cryoturbated, sand-dominated permafrost-effected *Psammentic Aquorthel* (Zubrzycki et al., 2013).

Samoylov is part of the lowland tundra vegetation zone, with sedges accompanied by mosses and willow shrubs. The vegetation species vary depending on if they are hydrophilic (water saturated centres and troughs) or if they prefer less saturated environments such as polygon ridges. On the active floodplain areas, vegetation is mostly absent (Boike et al., 2013).

2.1.3 Climate and snow cover

The climate is continental Arctic with a mean annual air temperature (1998 to 2017) of –12.3 ℃ and minimum winter temperature below –30 ℃ with the lowest temperatures

---

[3] `https://www.nrcs.usda.gov/wps/portal/nrcs/main/soils/survey/class/taxonomy/` [accessed 2022-06-28]

measured in February (–32.7 ℃). Liquid precipitation occurs in the short summer period between May and September with on average 169 mm for 1999 to 2017 (Boike et al., 2019). The snow cover on Samoylov Island is rather thin but enduring and is present from the end of September to the end of May with an annual average thickness of 0.3 m but can exceed 0.8 m (Boike et al., 2016).

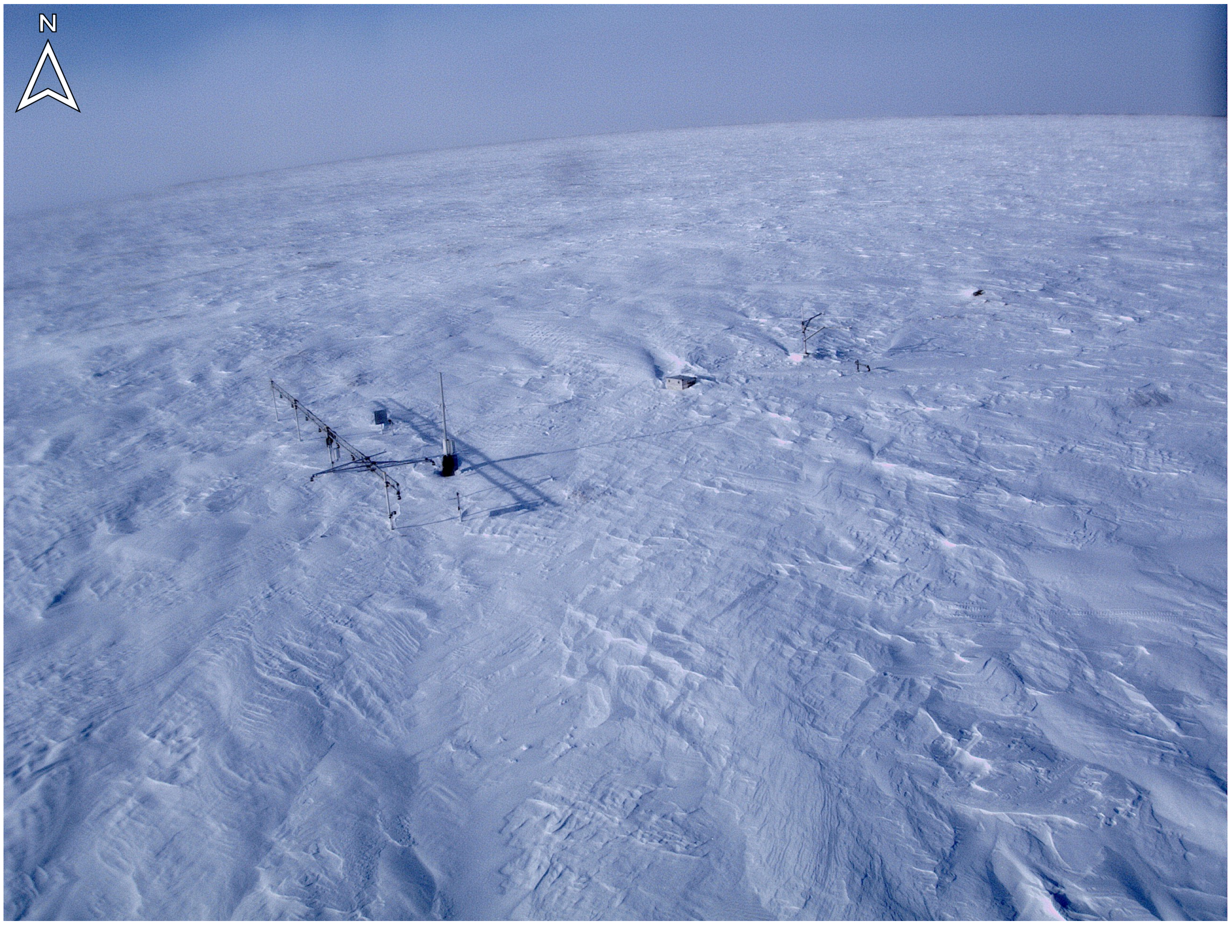

Figure 5: Time-lapse image from 17 April 2016 with ‹sastrugi› erosion patterns parallel to the wind direction (south-east). The ridges made out of hard snow, are several metres long and can reach several decimetres in height (Fierz et al., 2009). In the picture are the snow station (west) and the soil station (east).

In the tundra, wind redistribution of snow is an important process and leads to distinguished snow cover characteristics such as ‹sastrugi› which are shown in Fig.5. These erosion patterns form due to high wind speeds and are ridges of hard snow parallel to the wind direction. They can expand horizontally over several metres and several tens of centimetres vertically (Fierz et al., 2009). In general, the snowpack on Samoylov Island is composed out of basal depth hoar and dense wind slab on top and Boike et al. (2013) also described sediment-rich layers.

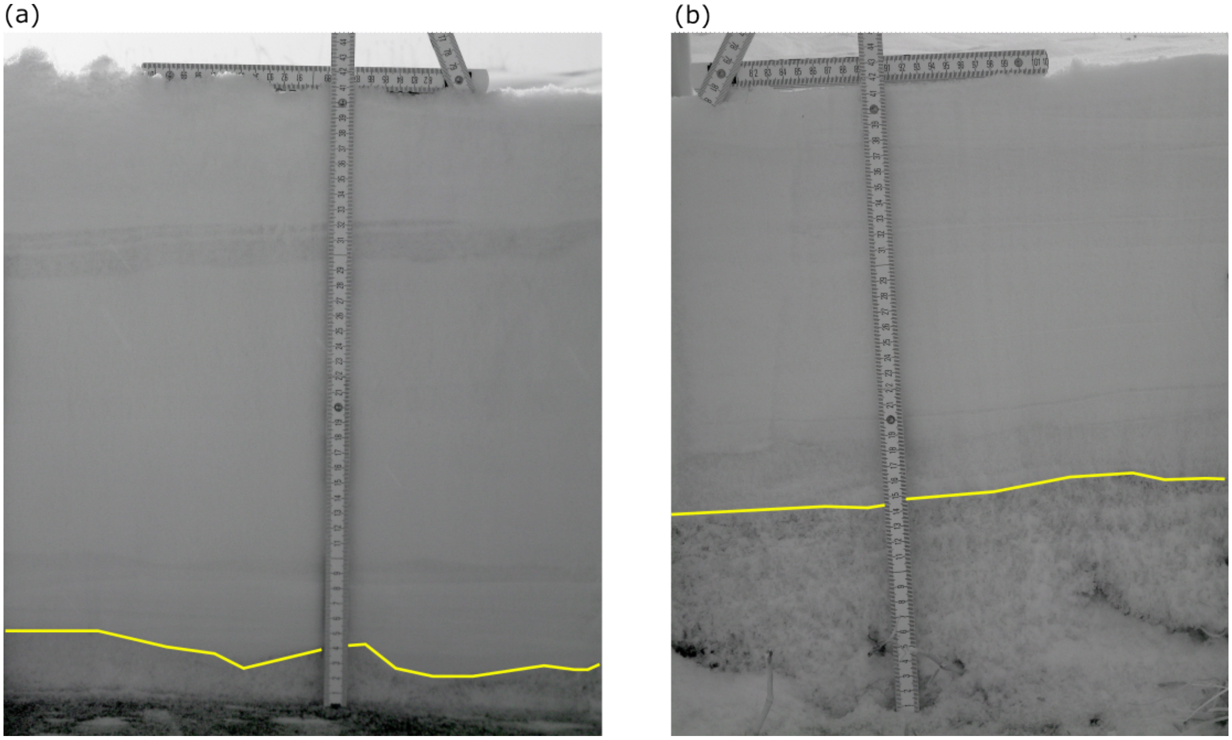

Figure 6: (a) snow profile in ice centre polygon (snow depth: 0.41 m, depth hoar thickness s/ total snow depth: 0.09) and (b) snow profile in grass-centre polygon (snow depth: 0.42 m, depth hoar thickness / total snow depth: 0.4). The yellow line divides the snowpack in the basal depth hoar layer and wind slab on top. Pictures were taken on Samoylov Island in April 2019 during the Lena Spring campaign (Fuchs et al., 2021).

The snowpack layering highly depends on the polygon micro-topography and as suggested by Gouttevin et al. (2018) can be differentiated into four micro-topography categories: grass-centres, ice-centres, rims and slopes. The pictures in Fig.6 show two snow profiles from Samoylov Island and demonstrate how the depth hoar to-total-snow depth ratio differed depending on the polygon centre type (ice- and grass-centre) in spring 2019.

The lower part of the snowpack in grass-centres is often interwoven with vegetation which can support the depth hoar formation (Domine et al., 2016a). Furthermore, frozen ground has a lower conductivity compared to ice which means there are lower temperatures in the ice-centre. Consequently, those generate a smaller temperature gradient (compared to the grass-centres) and given the same snow depth a smaller depth hoar layer is developed (Gouttevin et al., 2018). In this thesis the four classes are slightly different (no ice-centre) as they are based on the instrument setup of the snow station (Fig.4). Hence, these four micro-topographic classes were defined for my thesis: (grass-)centre, slope, rim and trough (between the two polygons of the LCP complex).

2.2 Instrumentation

In the following section, I am providing details about the instrumentation and data I used in this thesis. The data sets were chosen first and foremost to fit the validation purpose of the ‹CG Community› model output and hence include the snow physical properties snow depth, density and temperature, the soil temperatures and the Active Layer Thaw Depth (ALTD). Furthermore, I used soil Volumetric Water Content (VWC) and air temperature data sets. The majority of the parameters were measured at the snow station (Fig.8). Only the soil VWC as well as the second automated snow density measurement data set were obtained at the nearby soil station. The ALTD measurements were located in the southern part of the Island.

2.2.1 Soil observations

The ALTD was manually measured (with a simple metal rod) on a 150 point ‹CALM grid[4]› in operation since 2002. It is located about 1 km away in the southern part of the Island near the Samoylov Research station (Fig.3 (b)). For soil temperatures the sensor setup at the snow station was used. Soil temperatures were measured with Campbell Scientific T107 sensors with ±0.4 °C accuracy (–24 to 48 °C) in 0 m, 0.05 m, 0.1 m, 0.2 m, 0.4 m, 0.6 m, 0.8 m and 1 m depth.

For the soil VWC measurements the soil measurement station close by was used (72° 22.451′ N and 126° 29.757′ E) shown in Fig.4. Part of the installations in 2012 at the soil station was a Time-Domain Reflectometry (TDR) system to obtain the VWC of the soil. The VWC was measured in 0.14 m, 0.44 m, 0.72 m and 0.95 m depth with each a TDR probe connected to the Campbell Scientific TDR100 reflectometer.

The Campbell Scientific TDR probe (type CS605) has three rods with a length of 0.3 m and a diameter of 0.0048 m mounted parallel on an epoxy head. It is equipped with a RG58 cable (suitable for installations with less than 15 m length) which is connected to the TDR100 reflectometer. The probes were illustrated in Fig.7 (a). The rods of TDR

---

[4] `https://www2.gwu.edu/~calm/data/webforms/r51.htm` [accessed 2022-06-29]

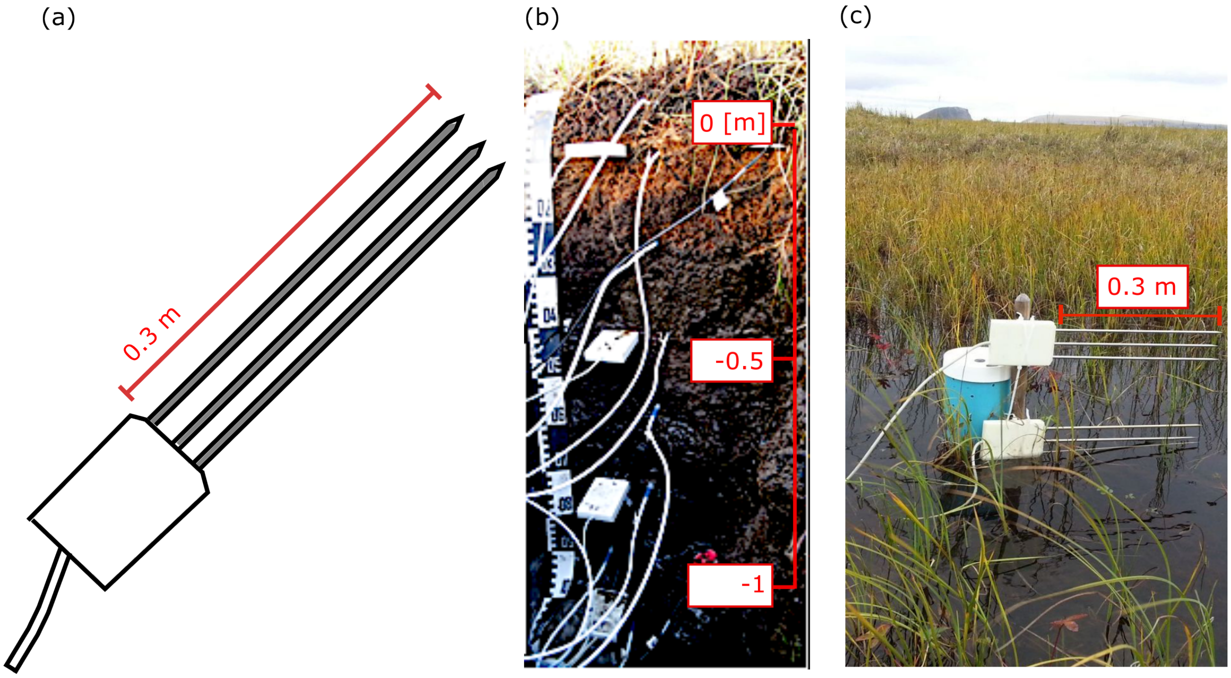

Figure 7: (a) sketch of the Campbell Scientific TDR probe (type CS605) with three 0.3 m rods mounted on an epoxy head and equipped with a RG58 cable. (b) soil profile to visualize the installation of the TDR probes for the VWC data set (soil station, August 2012). (c) TDR probe installation in 0.05 and 0.2 m height for snow density data set (soil station, August 2012).

probes were inserted directly into the soil profile (Fig.7 (b)) at the desired measurements depth. To obtain the VWC of the soil, a high frequency electromagnetic pulse is sent through the rod. The pulses' elapsed travel time is influenced by the travel distance (length of the rod) and the dielectric permittivity of the surrounding soil (which strongly depends on the soils' water content). From the reflected signal the dielectric permittivity of the soil is calculated and with that the VWC is equated (TDR100 reflectometer). The (frozen) soil is treated as a four-phase material (soil: solid matrix, interconnected pores: water, ice and air) and the detailed VWC calculations based on semi-empirical mixing model (Roth et al., 1990) can be found in Boike et al. (2018) (Appendix D1).

2.2.2 Snow observations

As part of the remote permafrost observatory, an advanced snow measurement station was set up in 2012 (Boike et al., 2019). The station was located about 1 km north-east of the Samoylov Research Station (Fig.3) at 72°22.452′ N and 126°29.753′ E (Fig.4). For the first time since the installation, I used the data from the snow station to investigate the inter-annual snow cover variability of the snow physical properties depth, density and temperature. Additionally, I processed a snow density data set from the nearby soil station as well as manual snow depth and density measurements, which were conducted on several locations on the island from field campaigns in 2018 and 2019.

The snow station was equipped with ten ultrasonic distance sensors mounted on a 15 m bar to capture the snow depth (Fig.8). The sensor setup covers an LCP complex consisting out of two wet polygons (Fig.4). An Snow Pack Analysing System (SPA-2) (Sommer Messtechnik, 2016) was installed in one of the polygon centres with three 5.5 m long horizontal strap sensors to obtain the snow density and moisture and a thermocouple installation was set up in between the straps of the SPA-2 to obtain the thermal profile of the snow (Fig.8,9). I also used the air temperature data set of the snow station in 0.8 m height in my thesis. The snow station was also equipped with four near-infrared surface temperature sensors and a sensor setup to monitor the crack width and timing in the polygon trough as well as in the centre with the SPA-2 but those data sets were not used in this thesis.

2.2.2.1 Snow depth The ten ultrasonic distance sensors (SR50A, Campbell Scientific) (Fig.8) cover four micro-topographic classes (centre, slope, rim and trough). The SR50A is an acoustic distance sensor which targets a aluminium plate laying on the ground beneath it. The plate ensures a flat surface and reduces noise caused by the vegetation, especially sedges (Boike et al., 2019). The sensor sends out ultrasonic (50 kHz) pulses and listens for returning echoes reflected by the aluminium target plate. The time from transmissions to return of an echo is used to calculate the distance based on the speed of sound. Most commonly, the SR50A is used for snow depth and water level measurements.

The snow height sensor covered an area between 1.3 m^2 and 0.6 m^2 depending on the height of the snow as the beam acceptance angle is 22°. In Fig. 8 the sensor setup is shown. There were in total five sensors measuring the snow depth in the two wet polygon centres of which four sensors were mounted in the same polygon centre as the SPA-2 installation. Two sensors were installed one each above the rims and two were mounted one each above the slopes. Only one snow depth sensor was mounted above the trough between the two polygons.

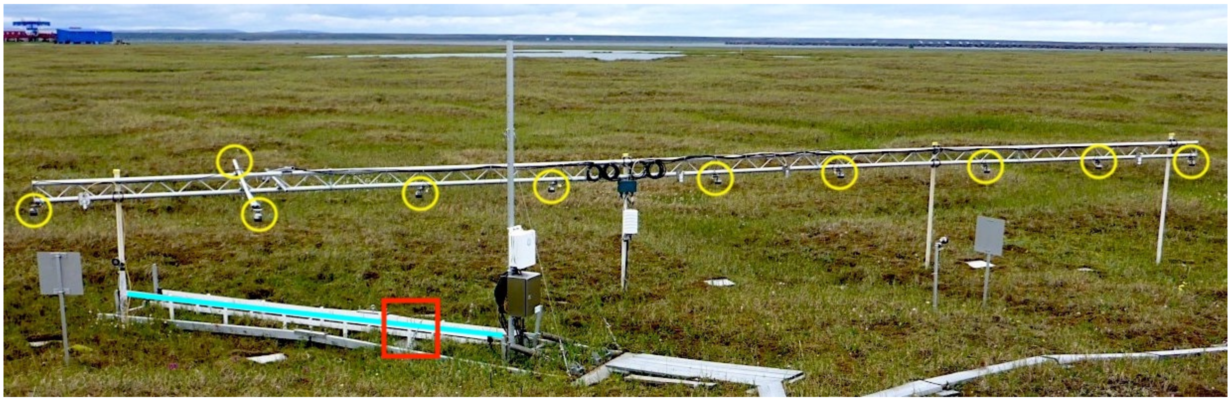

Figure 8: Snow station with SPA-2 unit in July 2016. The installation extends over two wet centre polygons and is equipped with ten acoustic distance sensors (snow depth) marked with yellow circles, an SPA-2 unit (marked in turquoise) and a thermocouple installation for snow temperature (marked in red). The soil temperature sensor setup is on the left side next to the station in the polygon centre, but not shown in the picture. The station also measures air temperature. Additionally, the near-infrared surface temperature and crack width and timing are measured (trough between polygons as well as in the centre with the SPA-2) but those data sets were not used in this thesis.

2.2.2.2 Snow density and SWE At the snow station an SPA-2 unit was set up in one of the two polygon centres encircled by four snow depth sensors (Fig.8). It provided the facilities to obtain the contents of liquid water and ice in the snowpack, the snow density, and the SWE (Sommer Messtechnik, 2016). As shown in Fig.9 the SPA-2 installation was made of three 5.5 m long strap sensors mounted at different heights (0.05 m, 0.15 m and 0.25 m) parallel to the ground.

In Fig.10 (a) a cross-section through one of the strap sensors is illustrated and shows the three copper wires, which were cast in a 0.06 m wide PolyEthylene (PE) flat band cable. The copper conductors have a low thermal capacity and the white PE insulation is less affected by heating due to solar radiation (Stacheder, 2005). The strap sensors each terminate in mounting boxes with which they were stretched to the aluminium frame. The measurement principle within the strap sensors is similar to the soil VWC measurements. Other than soil, snow has only the three components air, ice and water (wet snow). The components have different dielectric constants when measured with different frequencies. Along the strap sensors, the complex impedance is measured with a TDR (high frequency) and an impedance analyser (low frequency) to obtain the volumetric fractions of air, ice and water with a (horizontal) penetration depth of 0.04 m. The volumetric fractions are used to equate the output parameters: amount of liquid water, ice and air in the snow, the snow density [$\mathrm{kg\,m^{-3}}$] as well as the SWE [mm] (Sommer Messtechnik, 2016). The equations are not provided in detail in the manual.

Additionally, I calculated the snow density from the dielectric permittivity measurements of the TDR probe horizontally installed in 0.2 m at the soil station (Fig.7 (c)). The equation is in Sec.2.3. For both of the installations (SPA-2 and TDR probe in the snowpack) the major possible source of error is the formation of air gaps around the strap sensors and the TDR probe rods, respectively. For one thing, those provided the potential to alter the electron-magnetic signal, for another thing they are preferential flow paths for liquid water. For the SPA-2 unit an air gap correction algorithm (Stacheder, 2005; Huebner,

Figure 9: SPA-2 unit and thermocouple installation in July 2016. Three 5.5 m long strap sensors (SPA-2) to capture the snow density, SWE and volumetric water and ice content (marked in turquoise) were installed. The straps are mounted in 0.05, 0.15 and 0.25 m height and stretched to a aluminium frame. The thermocouple installation to obtain the snow thermal profile is located between the strap sensors (marked in red).

1999) is implemented in the software but can not be examined or adjusted by the user (Sommer Messtechnik, 2016). For the snow density calculations from the TDR probe the formation of air gaps was not taken into account.

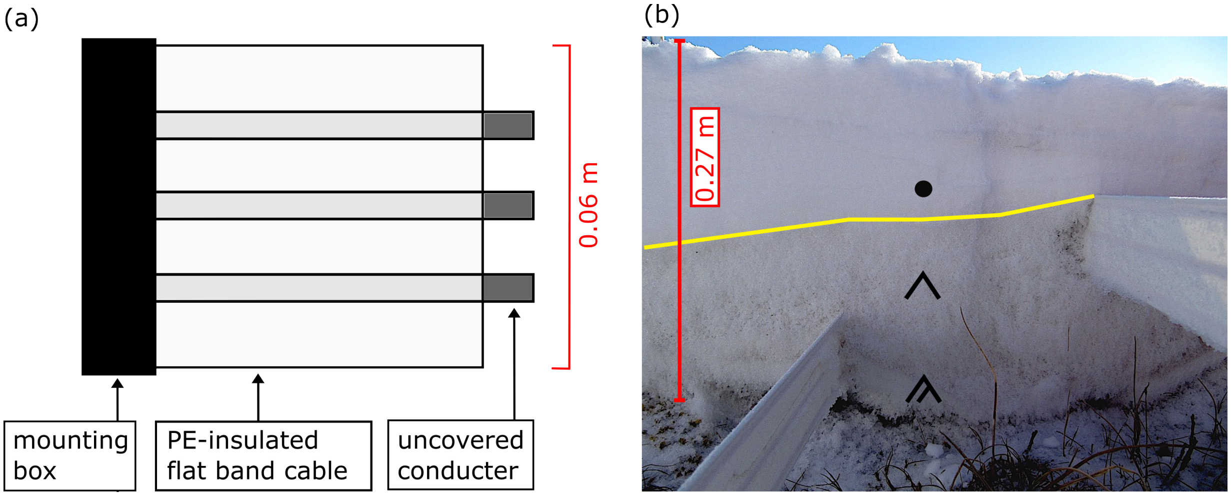

Figure 10: (a) illustration of a cross-section of one of the SPA-2 strap sensors (adapted after Staehli et al. (2004)). (b) SPA-2 unit in the snow in April 2013. The strap sensors in 0.05 and 0.15 m snow depth are shown. The total snow depth was 0.27 m an the snowpack was composed out of depth hoar to a depth of 0.15 m which was overlain by a wind slab (rounded grains). The yellow line separates the two layers. The grain classification was done following (Fierz et al., 2009). Next to the upper strap sensor (0.15 m) the depth hoar crystals indicate air gap and artificial depth hoar formation (darker colour).

2.2.2.3 Snow temperature The installation to obtain the temperature within the snowpack was a self-made construction with twelve thermocouples (type T for extremely low temperature applications, accuracy ± 1 ℃) vertically mounted on a square plate on the ground (Fig.11). The thermocouples had different lengths and were mounted convoluted in five centimetre steps to a maximum height of 0.5 m. A thermocouple can be used to obtain temperature differences as it produces a temperature-dependent voltage at the junction of two dissimilar metals. I used the snow temperature data set to obtain the thermal profile of the snow up to 0.5 m. To obtain the temperature gradient within in the snowpack the air temperature in 0.8 m height and the soil temperature in 0.05 m were used (Sec.2.3).

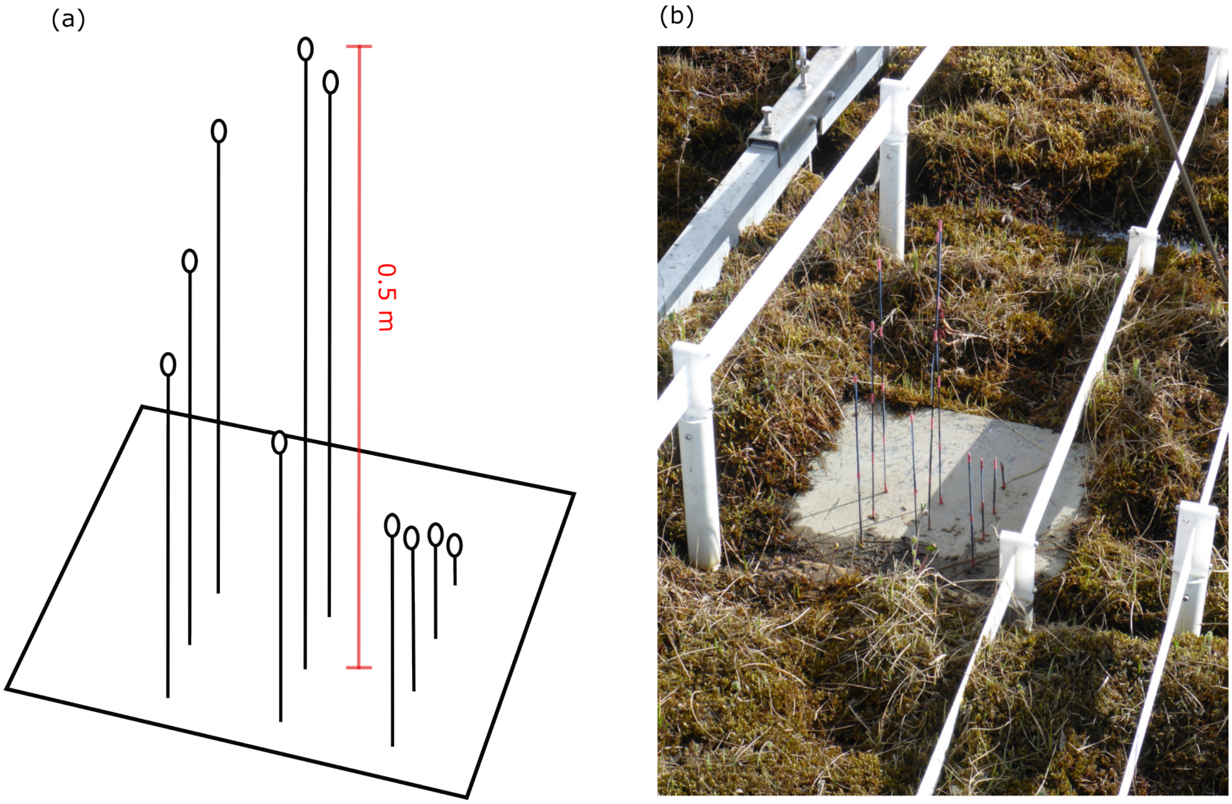

Figure 11: (a) sketch of the 10 thermocouples installed in 0.05 m steps from 0 to 0.5 m height. (b) thermocouple installation between SPA-2 straps in June 2018.

2.3 Data processing and calculations

The data used in this thesis were provided on a various temporal and spatial scales, ranging from half-hourly automated sensors measurements to manual measurements from field campaigns. My processing of the time series data included the following steps:

- automated quality analysis of time series
- physical consistency check and manual removal of outliers
- aggregation of the time series into daily averages

Both the snow and soil station provide half-hourly data output and I average the following automated sensor data sets in my thesis to daily resolution: soil temperature, soil VWC, snow depth, snow density, snow temperature. Therewith, I enabled a reasonable time step for the analyses and model validation. Additionally, I analysed snow profile data from two expeditions in 2018 and 2019 to obtain information on snow density and snow depth, respectively.

2.3.1 Active Layer Thaw Depth

From the ‹CALM grid› data set, I calculated the median ALTD for each last day of measurements (between late August to mid of September) per year from 2014 to 2017. I used all the 150 grid points, which covered all four micro-topographic classes (centre, slope, rim and trough).

2.3.2 Snow depth

The snow depth data set was quality controlled following Boike et al. (2019) (Sec. 3.1.5 and 3.1.6). I analysed the snow depth for a period of six years from 2014 to 2020 by calculating the mean as well as the standard deviation for each of the micro-topographical classes of the LCP complex: (grass-)centre (five sensors), slope (two sensors), rim (two sensors) and trough (one sensor). The data sets before 2014 had major data gaps during the winter time and were not used in my thesis. To characterize the snow cover per year two output parameters e.g. for modeling purposes, the maximum snow depth of the entire season as well as the End-Of-Season (EOS) snow depth were calculated for these classes. I defined the EOS snow depth as the average snow depth between the 15 April and 15 May (before the start of the melting season) of each year. To validate the automated snow depth sensor measurements against field observations I used the data obtained during the Lena River Spring campaign in April 2019 (Fuchs et al., 2021). This data was collected on Samoylov Island in close proximity to the snow station.

2.3.3 Snow density and SWE

To study the annual and inter-annual variability of the snow density, I calculated the average bulk density (ρ_{bulk}) for the entire snowpack by averaging the data of the three strap sensors from the SPA-2 unit in 0.05, 0.15 and 0.25 m height. This was done for four years from 2016 to 2020 as before 2016 no data was available due to technical failure of the SPA-2. I used the SPA-2 density output in combination with the average centre snow depth (average of 5 sensors z_{centre} [mm]). Only when the snow depth exceeded the strap sensor mounting height by at least 0.05 m I processed the density. With that, I guaranteed snow density measurements with a minimum of air influence due to a partially covered sensor.

I calculated the EOS density out of the SPA-2 density output. Additionally, following Eqn.(1), I calculated the SWE ($\mathrm{SWE_{bulk}}$[mm]) with ρ_{bulk} [kg m^{-3}], z_{centre} [mm] and the density of water (ρ_{water} [kg m^{-3}])

$$\mathrm{SWE_{bulk}} = \mathrm{z_{centre}} \frac{\rho_{\mathrm{bulk}}}{\rho_{\mathrm{water}}}. \tag{1}$$

For the seasons 2016/2017 and 2017/2018) I analysed the seasonal snow density evolution. Unfortunately, the data after 2018 had major data gaps and hence, was not suitable for detailed seasonal analyses. For the snow season 2016/2017, I compared the density output from the SPA-2 against the snow density calculated from the dielectric permittivity measurements from the TDR probe at the soil station. I calculated the snow density (ρ_{TDR} [kg m^{-3}]) following (Frolov and Macheret, 1999). The dielectric permittivity (ϵ) needs to be calibrated to air conditions. The minimum value of ϵ should equal 1 for ‹no snow› conditions (summer) and hence, prior I had to calculate the offset (x_{off}) for every measurement by subtracting each from 1. I applied the offset correction in Eqn.2

$$\rho_{TDR} = \frac{(\sqrt{(\epsilon + x_{off}) - 1})}{0.845}. \tag{2}$$

Also, manual density measurements from the spring 2018 campaign were used to validate the SPA-2 performance (Tab.7 and Tab.8). The data was obtained on the island, but not in the same LCP complex.

2.3.4 Snow and soil temperature

For analysis of the snow and ground thermal regime, I used the thermocouple and soil temperature installations from the snow station for the years 2014 to 2018. The snow temperature data sets before 2014 and after 2018 had major data gaps due to technical failure and hence, were not used. The soil data was used only for the years when snow temperature data was available. With the two temperature data sets I constructed the thermal profile starting at 0.5 m above the ground to –1 m below the ground surface. As I described earlier, snow temperatures were measured in constant 0.05 m steps.

The soil temperatures were measured with a narrow 0.05 m spacing in the upper part of the soil profile and below 0.2 m the sensors were installed with a 0.2 m spacing down to 1 m depth. To obtain an evenly spaced thermal profile I linearly interpolated each of the data sets with a 0.01 m spacing. The next processing step was to intersect the thermocouple sensor height with the daily snow depth to only take into account measurements of snow covered sensors. For that purpose, I used the centre snow depth sensor, next to the thermocouple installation, and if this sensor showed data gaps, the other centre snow depth sensors were used. Values $\geq$ –0.5 ℃ were deleted as liquid water should not be present in the snowpack during winter (compensation sensor accuracy).

To study the interaction between the upper snow layers and the air temperature, the air temperature sensor in 0.8 m height of the snow station was used. Additionally, I used the air temperature data set in combination with the soil temperature at –0.05 m depth to calculate the daily temperature gradient T_{grad} [K m^{-1}] in the snowpack following Eqn.(3) with T_{grad} [K], T_{soil} [℃], T_{air} [℃] and z_{centre} [m]

$$T_{grad} = \frac{(T_{soil} - T_{air})}{z_{centre}}. \tag{3}$$

The temperature gradient was applied when the snow depth measured by the nearest sensor exceeded 0.01 m.

2.4 CryoGrid permafrost model

With the following section I am providing an introduction about the genesis, structure and equations of the ‹CG Community› model. Additionally, I am summarizing the parameterization of the model runs performed in this thesis.

The first CG version ‹CG 1› was a climate-equilibrium model developed to obtain the permafrost distribution in Norway with a spatial resolution of 1 km^2 by incorporating the variations of interacting parameters snow, vegetation and soil characteristics (Gisnås et al., 2013). The second version ‹CG 2› represented the consistent further development of the first version addressed to model changes in the representation of the ground thermal regime under a non-steady-state climate (Westermann et al., 2013). Changes in temperature and energy were described by Fourier's law of heat conduction, latent heat generation and consumption were processed due to soil freezing and thawing, respectively. Furthermore, no movement of water or water vapor was implemented and changes in soil moisture occurred only due to freezing or thawing processes. There were no lateral heat fluxes between grid cells. In ‹CG 3› the surface-energy-balance as upper boundary conditions and improvements to the snow scheme were implemented

(Westermann and Langer, 2014; Westermann et al., 2016).

The ‹CG 3› version underwent several improvements and adaptations in the recent past. Nitzbon et al. (2019) developed a tile-based approach to model the ice-wedge degradation process by implementing lateral subsurface heat and water fluxes as well as snow distribution due to wind transport and additionally also included lateral sediment transport (Nitzbon et al., 2020). In ‹CG 3› the advanced snow scheme Crocus (Vionnet et al., 2012) was implemented (Zweigel et al., 2021) and with that microphysics parameterization was introduced.

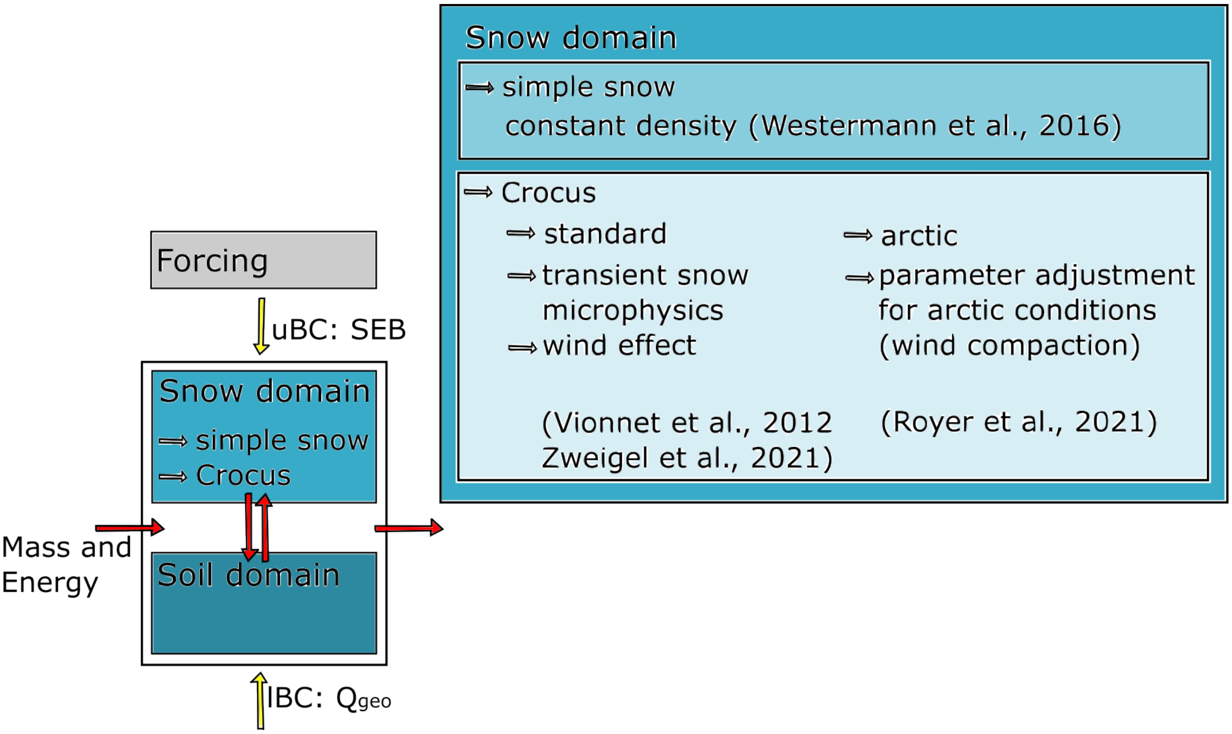

Figure 12: ‹CG Community› scheme based on Westermann et al. (2022). uBC: upper boundary condition, lBC: lower boundary condition.

Most recently, the ‹Arctic Crocus› version (Royer et al., 2021b) was implemented, tailored especially for Arctic snow processes such as increased wind compaction and vegetation trapping effect (to produce basal low density layers), as well as the inclusion of the thermal conductivity equation following (Sturm et al., 1997). The new model code, combining all the implementations, is the ‹CG Community[5]› release. In the ‹CG Community› model the different model components e.g. the snow or soil regime which can

---

[5] `https://github.com/CryoGrid/CryoGridCommunity_source`

be tailored together by the user (e.g. complex vs. simple snow scheme). The ‹CG Community› model chiefly realizes single-tile (1D) stratigraphies and multi-tile (3D) model runs are possible by combining several 1D stratigraphies (Westermann et al., 2022). Fig.12 sketches the skeleton of the model with boundary conditions. The base is a single tile with different classes for the snow regime above the surface and for the soil regime underneath assuming external reservoirs for lateral mass and energy exchange.

2.4.1 Snow classes

The snow cover in ‹CG Community› can be realized with either a simple snow scheme or with a sophisticated snow scheme including snow microphysics (Fig.12). Changes in snow depth are linked to the amount of SWE (for dry snow) within a grid cell which is defined by the user. The mobilisation of meltwater is bound to a user-defined field capacity.

The ‹CG Community› model is capable of processing the snow cover during the onset of the snow season as well as during the melting season. For one thing, snowfall and snow melt respectively trigger the establishment and removal of a snow class. The very shallow snow depth during the border seasons involves complex numerical processes (small grid cells and small time-steps) and hence, the snow class during those periods is treated as a so called ‹CHILD› class, which is not part of the CG stratigraphy setup until it reaches a certain grid cell size (and vice versa during the snow melt) (Westermann et al., 2022).

In my thesis, I only used the sophisticated snow class based on the equations of the Crocus snow scheme(Vionnet et al., 2012; Royer et al., 2021b) which was implemented in the ‹CG Community› model by Zweigel et al. (2021). The snow scheme is available either with ‹Standard› (Vionnet et al., 2012) or ‹Arctic› (Royer et al., 2021b) parameterization. The implementation of the Crocus snow scheme enriched the ‹CG Community› model with surface-energy-balance, snow microphysic processes and also the bucket-scheme snow hydrology (Westermann et al., 2022). The energy transfer (upper boundary) is based on the surface-energy-balance. For each grid cell it is based ‹on the spectrally resolved calculation of albedo and short wave penetration and absorption› (Westermann et al., 2022). New snow is parameterized with density, grain size, dendricity and sphericity in relationship with the input parameters air temperature and wind speed. Snow metamorphism laws based on Brun et al. (1992) were introduced including transient grain shape (dendricity, sphericity, grain size, historical information about the presence of liquid water or faceted crystals in time) and density. Metamorphism relies on temperature gradient within the snow, water content and overlaying snow layers (Westermann et al., 2022) and the influence of wind drift is taken into account as it affects the upper snow layers through densification. Accumulating snow density then becomes a function of the meteorological parameters, wind speed and air temperature (Vionnet et al., 2012). Evaporation and sublimation are realized in this class.

The thermal conductivity (k_{yen} [W m^{-1} K^{-1}]) is calculated based on the equation by Yen (1981) (exponential relationship Eqn.(4)) with ρ [g cm^{-3}] the density of snow and ρ_{water} the liquid water density

$$k_{yen} = k_{ice}\left(\frac{\rho}{\rho_{water}}\right)^{1.88}. \tag{4}$$

As I mentioned before, within the Crocus snow class the user has the possibility to choose between the ‹Standard Crocus› scheme and the ‹Arctic Crocus› scheme. The latter had adjusted parameters better suited to Arctic snowpack conditions published by Royer et al. (2021b). Adjustment of their study implemented in the ‹CG Community› model are the adaptation to the fresh snow density parameterization (doubled effect of wind), as well as the overall increased snowpack densification due to wind compaction (tripled), as the influence of the wind effect by Vionnet et al. (2012) is assumed to be too low. In the ‹Arctic Crocus› scheme, a new maximum for wind impacted density was introduced (600 kg m^{-3}) almost twice value of the ‹Standard Crocus› scheme 350 kg m^{-3} in Vionnet et al. (2012)). In the ‹Arctic Crocus› scheme the thermal conductivity (k_{sturm}) is based on the equation by Sturm et al. (1997) (Eqn.(5))

$$\begin{aligned} k_{sturm} &= 0.138 - 1.01\rho + 3.233\rho^2\{0.156 \leq \rho \leq 0.60\} \\ k_{sturm} &= 0.023 + 0.234\rho\{\rho < 0.156\}. \end{aligned} \tag{5}$$

Not implemented in the Crocus class of the ‹CG Community› model is the vegetation height parameter. This parameter takes into account the vegetation trapping effect. It is simulating a basal low density layer i.e. depth hoar by disabling the wind compaction and increasing the snow viscosity at heights below the vegetation height (Royer et al., 2021b).

2.4.2 Ground classes

The soil domain classes require user-defined soil properties, which are the volumetric mineral (θ_m), organic (θ_o), water (θ_w) and ice (θ_i) content as well as the field capacity (θ_{fc}). Also, the layer depths need to be adjusted individually and the porosity $\phi = 1 - \theta_m - \theta_o$ is also set by the user. Per grid cell the enthalpy state e [Jm^{-3}] and temperature following Eqn.(6) are integrated for every time step, taking into account the volumetric heat capacity c [JK^{-1}m^3], the temperature T [celsius$C$], the volumetric latent heat of water freezing L_{sl}^{vol} [Jm^{-3}] and the sum of water and ice contents θ_{wi}. More detailed explanations can be found in Westermann et al. (2022).

$$e(T, \theta_w) = cT - L_{sl}^{vol}(\theta_{wi} - \theta_i)) \tag{6}$$

I use the surface energy balance (Eqn.(7)) as the upper boundary condition for both the snow and the soil class. The energy flux $F_{ub}(t)$ in the uppermost grid cell follows

$$F_{ub}(t) = S_{in}(t) - S_{out}(t) + L_{in}(t) - L_{out}(t) - Q_h(t) - Q_e(t), \tag{7}$$

using short-wave radiation (S_{in}, S_{out}), long-wave radiation (L_{in}, L_{out}) and sensible (Q_h) as well as latent heat (Q_e). The last two are defined positive when the surface is cooling (Westermann et al., 2022). As the incoming short- and long-wave radiation is provided, the other variables are based on the following calculations. The outgoing short-wave radiation is computed using the surface albedo (α_s)

$$S_{out} = -\alpha_s S_{in}. \tag{8}$$

Outgoing long-wave radiation L_{out} is based on Kirchhoff's and Stefan-Boltzmann Law (Eqn.(9)) using the Stefan-Boltzmann constant ω_{sb} [kgs^{-3}K^{-4}], the freezing temperature of free water and the surface emissivity σ $[-]$

$$L_{out} = \epsilon\sigma_{sb}(T + 273.15K)^4 + (1 - \epsilon)L_{in}. \tag{9}$$

The sensible (Q_h) heat flux (Eqn.(10)) is calculated using the air temperature at a certain height T_{air} (h) and the temperature of the first grid cell with respect to the air density ρ_{air} [kgm^{-3}], air heat capacity c_p [Jkg^{-1}] at constant pressure and aerodynamic resistance r_a as detailed described in detail by Westermann et al. (2016)

$$Q_h = \frac{\rho_{air} c_p}{r_a}(T_{air} - T_1). \tag{10}$$

The latent heat flux Q_e (Eqn.(11)) takes into account the latent heat($L_{lg,sg}$ [JKg^{-1}]) of evaporation (lg) and sublimation (sg) with different approaches for the reduction factor f $[-]$, the resistance r_e [sm^{-2}] and specific humidity above the surface q_1 (see Westermann et al. (2022))

$$Q_e = \rho_{air} L_{lg,sg} \frac{f}{r_e}(q_{air} - q_1). \tag{11}$$

The ground thermal heat flux Q_{geo} [Wm^{-2}] at the lower boundary (lowermost grid cell) is simply obtained through a user-defined constant heat flux F_{lb} [Wm^{-2}].

In the subsurface, the change of enthalpy is calculated via the continuity equation (Eqn.(12)) (Westermann et al., 2022) requiring the vertical coordinate z [m], the flux emerging from heat conuction j_{hs} and the flux due to heat advected by water j_{hw}

$$\frac{\partial e}{\partial t} = -\frac{\partial j_{hc}}{\partial z} - \frac{\partial j_{hw}}{\partial z}. \tag{12}$$

Soil freezing characteristics are bound to the soils' temperature and liquid water content (Westermann et al., 2022). There are currently three hydrology mechanisms in the ‹CG community model› (Westermann et al., 2022):

[1] no flow (i.e. constant water plus ice contents)

[2] the bucket scheme (gravity driven water flow downwards)

[3] vertical water flow following the Richards equation

I used the bucket scheme [2] for the first 10 m of the soil domain. Deeper layers are hydrological inactive. In the bucket scheme, water is either immobile (bound to the soil matrix) or in a gravity driven downward flow. The parameter defining the threshold between the immobile and flowing water state is the field capacity (θ_{fc}) which has to be defined by the user. For unsaturated soil conditions, the vertical water flux (j_w^v) follows

$$j_w^v = \begin{cases} -K_w & for\ \theta_w > \theta_{fc} \\ 0 & for\ \theta_w \leq \theta_{fc} \end{cases} \tag{13}$$

with K_w [ms^{-1}] the hydraulic conductivity which is calculated with the user-defined saturated hydraulic conductivity following

$$K_w = K_{w,s}/\Phi. \tag{14}$$

In saturated conditions no vertical water flux occurs except when evaporation leads to water loss. The calculations can be found in more detail in Westermann et al. (2022). In the deeper soil layers (>10 m) I used the no flow water scheme ($j_w = 0$) where rainfall, snowmelt and evaporation do not influence the sum of water and ice contents (Westermann et al., 2022).

2.4.3 Forcing

I used two different forcing data sets for the model runs in this thesis. The first one is ERA-Interim forcing data for the Lena Delta region with 3-hourly averages of air temperature in 2 m height [℃], rainfall [mm], snowfall [mm], surface pressure [Pa], incoming short wave radiation [W m^2], incoming long-wave radiation [W m^2], windspeed 10 m height [m s^{-1}] and specific humidity [g kg^{-1}]. The ERA-Interim reanalysis product covers the time span from 1979 to 2019 and has a spatial resolution of about 80 km or 0.75°. The RCP2.6, RCP4.5 and RCP8.5 scenario data of the Community Climate System Model (CCSM4) were applied as decadal anomalies to the ERA-Interim data to generate the projected time span (Koven et al., 2015). The CCSM4 (spatial resolution of 1.25° EW x 0.9° NS) model grid was interpolated to fit the ERA-Interim grid. The data can be downloaded on the website from the NCAR Climate Data, Gateway[6]. In this work, the forcing file is named ‹ERA19›.

The second forcing file is the one used and described in detail by Westermann et al. (2016). It is part of the ‹CG Community› model code. It is based on an in-situ data set of incoming short wave and long-wave radiation, air temperature, absolute humidity and wind speed from Samoylov Island. Time series data gaps were filled with ERA-Interim reanalysis. Precipitation rates were obtained directly from the reanalysis, as now in-situ data is available. In my work this forcing file is named ‹ERA44›.

---

[6] `https://www.earthsystemgrid.org`[accessed 2022-07-05]

2.4.4 CG Standard Crocus

For the first model, run I set up the soil stratigraphy as shown in Tab.1, representing the soil profile of a polygon centre on Samoylov Island following Nitzbon et al. (2020). I used the field capacity as a setting parameter rather than a realistic portrayal of the layer field capacity and is set constant for the entire soil profile. The snow domain uses the Standard Crocus scheme (Vionnet et al., 2012) with the conductivity function of Yen (1981) and a maximum density of 500 kg m^{-3} to still represent realistic wind compaction conditions. I run the model first with the ERA-Interim forcing data based completely on reanalysis products. I refer to this run as **CG Standard Crocus ERA19** in my thesis (A.4). The parameter file for the model run I run the parameter again with the forcing data based on the automated meteorological measurements (Boike et al., 2013) as used by Westermann et al. (2016) and I refer to this run as **CG Standard Crocus ERA44** (A.4).

Table 1: Soil stratigraphy for a low polygon centre on Samoylov Island, based on Nitzbon et al. (2020) with constant field capacity.

depth [m]	ϕ	θ_m	θ_o	soil type	θ_{fc}
0	0.85	0	0.15	sand	0.5
0.1	0.75	0.1	0.15	sand	0.5
0.2	0.65	0.25	0.1	silt	0.5
1	0.55	0.26	0.19	silt	0.5
10	0.45	0.5	0.05	sand	0.5
30	0.1	0.9	0	sand	0.5

2.4.5 CG Arctic Crocus

To compare the snow scheme performance with different parameterizations, I set up another model run using the Arctic Crocus version (Royer et al., 2021b) with particular settings for the wind related processes, new snow density, compaction dynamics and the snow thermal conductivity function following Sturm et al. (1997). The soil parameterization is the same as for the Standard Crocus model run (Tab. 1). I named the third model run **CG Arctic Crocus ERA19** (A.4).

2.5 Validation

I separated the model validation routine into different steps. First, to evaluate the model performance regarding the soil thermal and hydrological regime, a CG Standard Crocus ERA19 run was compared with the ALTD data from the CALM grid located on Samoylov Island. The ALTD from the 15 September of each modeled year was used for the comparison. I run the CG Standard Crocus ERA19 setup with three different adjustments (trial runs) for θ_{fc} and compared each of them with the manual ALTD data set to obtain the final soil profile parameters shown in Tab. 1. In the first trial run I used the θ_{fc}-profile as shown in Tab.2. In the second trial run, I set θ_{fc} to 0.4 as suggested by (Nitzbon et al., 2020). For the last trial run, I used θ_{fc} of 0.5. From each trial run I extracted the EOS ALTD (mid-September of each year) and compared it with the field observations.

Table 2: Field capacity (θ_{fc}) profile used in the first model setup to check if the model set up is able to reproduce the Samoylov site conditions.

depth [m]	soil type	θ_{fc}
0	sand	0.1
0.1	sand	0.2
0.2	silt	0.3
1	silt	0.3
10	sand	0.3
30	sand	0.1

From here on, I used the results of each of the three model setups for the validation routine (CG Standard Crocus ERA19, CG Standard Crocus ERA44 and CG Arctic Crocus ERA19). To investigate the inter-annual and seasonal variability of the snow depth, I compared the modelled snow depth of the three model runs with the average snow depth measured with the sensors in the centre of the LCP complex of the snow station. Additionally, I calculated the EOS and maximum snow depth for each snow season per run. To evaluate the model performance I calculated the Root Mean Squared Error (RMSE) and the Mean Bias Error (MBE) for each run for the three snow parameters snow depth, density and temperature as well as the soil temperature. I used the automated measurements as reference data.

For the last steps of the validation routine, I directly compared the models' snow density output with the SPA-2 density measurements for the 2016/2017 season and the

2017/2018.For the density comparison, I set the snow season dates to the 15 October until the 31 May for both the sensor and the model data set. I did this to ensure a fully covered SPA-2 sensor. For the density comparison in 0.05, 0.15 and 0.25 m snow height I processed the model data so, that in total the density at 0.05 m around the sensor height were taken into account e.g. for the comparison in 0.15 m depth the generated densities from 0.13 to 0.17 m were used for the box plots.

I compared the modelled thermal snow profile outputs for a time span of four years (2014 to 2018) with the automated measurements. For the snow temperature comparison, I only used model temperatures at the same height (0.05 to 0.5 m in 0.05 m steps) as the measured temperatures. Furthermore, to ensure comparability, I applied the dates (snow onset and melting begin) which I determined from sensor data set to the model data set.

3 Results

This chapter contains the results of my studies. First, I present the results of the inter-annual variability of the snow physical properties snow depth, temperature and density as well as soil properties (temperature and VWC) within the 6-year-record from 2014 to 2020. Second, I compare these characteristics with the results of my model runs from 2014 to 2018.

3.1 Snow depth

For the 6-year record (2014 to 2020) I analysed the yearly variability of the snow depth and calculated the EOS snow depth as well as the maximum snow depth for each one of the micro-topographical classes in the LCP complex (centre, slope, rim and trough). The overall trend as displayed in Fig.13 was an increase in snow depth from 2014 (maximum centre snow depth 0.44±0.03 m, centre EOS snow depth 0.51±0.04 m) until 2018 2017/2018 (maximum centre snow depth 0.74±0.05 m, centre EOS snow depth 0.6±0.06 m). In 2018/2019 the snow depth decreased to a maximum centre snow depth of 0.39±0.04 m and a centre EOS snow depth of 0.46±0.07 m.

The manual field measurements from the 2019 spring campaign (green dots in Fig.13 (a)) were in the same range as the automated measurements of this season even though they were not obtained in the same LCP complex. The last season 2019/2020 showed again a slight increase in snow depth (maximum centre snow depth 0.53±0.01 m, centre EOS snow depth 0.61 m). I summarized the results in Tab.3. The six years showed an inter-annual variability of the snow cover onset (Fig.13 (a)). The years from 2014 to 2016 showed a gradual increase in snow depth, whereas from 2017 to 2019 the snow depth abruptly increased. For example in the 2017/2018 season the snow depth abruptly increased up to 0.2 m in beginning-October, then stagnated until mid-November from whereon a more gradual build-up took place for the rest of the season.

I found a high spatial variability within the snow depths records. The snow depth in all years was the deepest in the centre and trough location and the shallowest on rims (Fig.13). The mean EOS snow depth in the centre was between 0.39 m (2018/2019) to 0.63 m (2016/2017) and the mean EOS snow depth on the rims was between 0.22 m (2018/2019) to 0.43 m (2016/2017), respectively. I found the same spatial variability in the maximum snow depth which for each snow season was also recorded within the centre and trough areas of the LCP complex (Fig. 13) between 0.46 m (2018/2019) to 0.74 m (2017/2018). Sensors installed above the rims recorded the lowest maximum snow depth values for each year between 0.32 m (2014/2015) to 0.53 m (2017/2018).

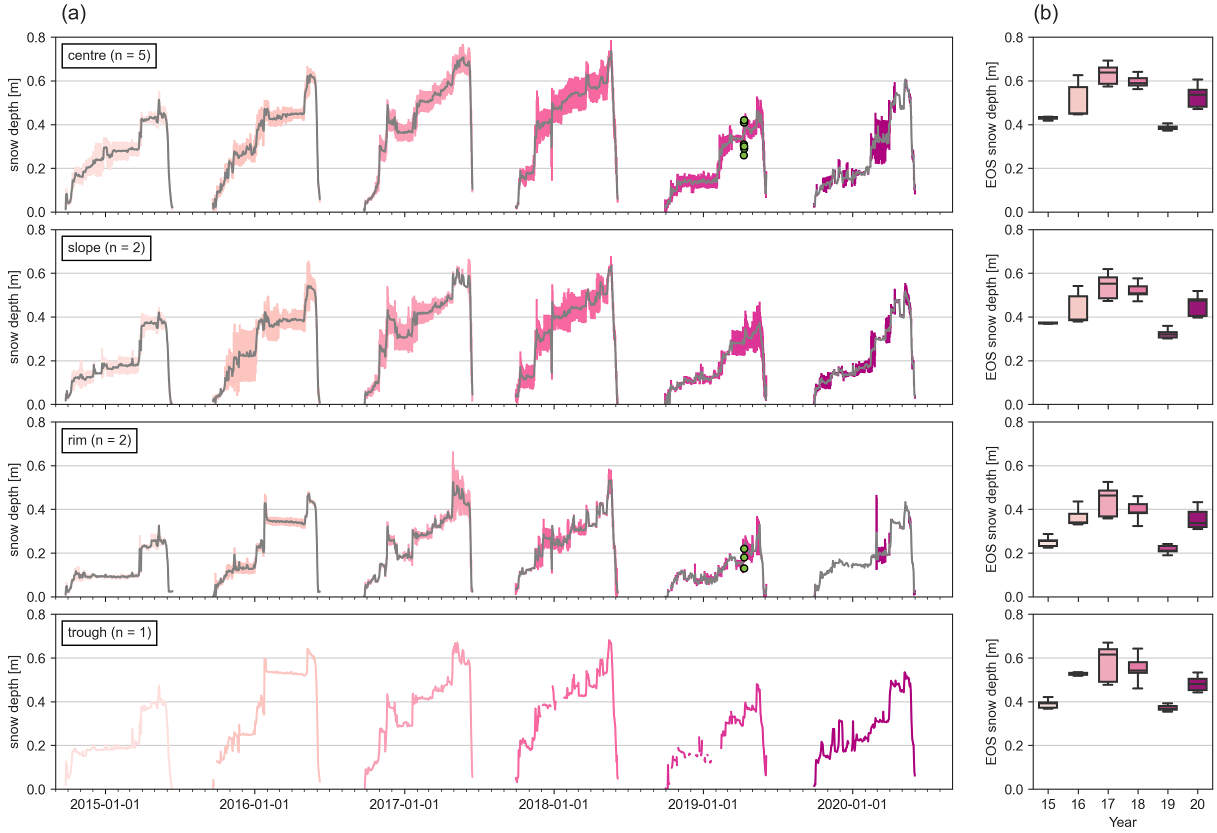

Figure 13: (a) Mean snow depth (grey line) and standard deviation (shades of pink) for the micro-topographic locations in the LCP complex. Number of sensors (n) used to calculate the mean snow depth are given in the legends. Green dots are manual validation measurements from the 2019 spring campaign (Fuchs et al., 2021). (b) EOS (End Of Season) snow depth between 15 April to 15 May for each year. The colours match with the colours used in (a).

Table 3: EOS (End Of Season) and maximum snow depth in [m] per snow season (2014 to 2020). The means were calculated for each micro-topographical sensor set: five sensors for the centre, two for the slope and two for the rim. There is only one sensor measuring snow depth in the trough. Rows with * are missing the standard deviation as there was only one sensor contributing to the data set.

season	**location**	EOS depth$_{\text{mean}}$ [m]	EOS depth$_{\text{std}}$ [m]	maximum depth$_{\text{mean}}$ [m]	maximum depth$_{\text{std}}$ [m]
2014/2015	centre	0.44	0.03	0.51	0.04
	rim	0.25	0.02	0.32	0.01
	slope	0.37	0.03	0.42	0.03
	trough*	0.39		0.47	
2015/2016	centre	0.51	0.03	0.62	0.03
	rim	0.37	0.01	0.5	0
	slope	0.44	0.06	0.54	0.11
	trough*	0.55		0.64	
2016/2017	centre	0.63	0.04	0.71	0.05
	rim	0.43	0.06	0.53	0.14
	slope	0.54	0.01	0.62	0.02
	trough*	0.57		0.67	
2017/2018	centre	0.6	0.06	0.74	0.05
	rim	0.41	0.01	0.53	0.05
	slope	0.52	0.05	0.63	0.05
	trough*	0.55		0.68	
2018/2019	centre	0.39	0.04	0.46	0.07
	rim*	0.22	0.03	0.33	
	slope	0.32	0.07	0.38	0.1
	trough*	0.38		0.5	
2019/2020	centre*	0.53	0.01	0.61	
	rim*	0.35	0.04	0.43	
	slope	0.46	0.01	0.52	0.04
	trough*	0.48		0.53	

3.2 Thermal profile

In Fig. 14 I plotted the thermal profile of the snowpack and soil down to 1 m for the snow seasons 2014 to 2018. In general, the measured temperatures were in range from –50 ℃ in the snowpack to 15 ℃ in the soil during the summer.

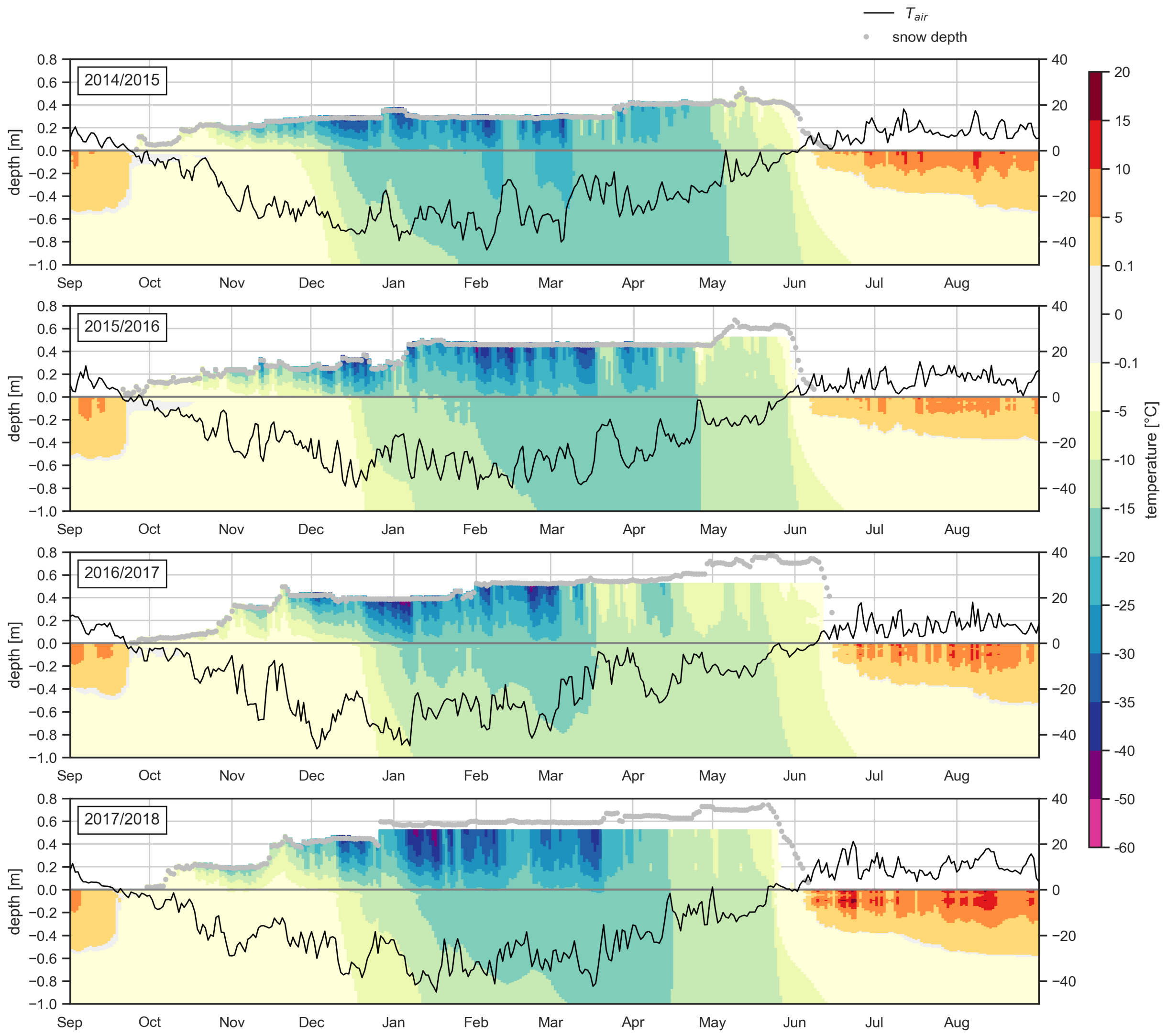

Figure 14: Thermal profile for the snow cover and soil (2014 to 2018). The snow temperatures were only measured up to 0.5 m height. The snow depth (dotted light grey line) was from the centre sensor closest to the thermocouple installation. The ground surface is the grey line and the black graph is the air temperature in 0.8 m (right axis). The discrete colour bar for the snow and soil temperatures was set to 5 ℃ steps, except for the 0 ℃ sector, where a narrower spacing of 0.1 ℃ was used to accurately depict the zero curtain. Temperatures between –40 and –60 are displayed in 10 ℃ steps.

For all four years the thermal profile followed the same general pattern. During the end of the summer season, in September, with still positive air temperatures, the soil temperatures down to 0.2 m were between 5 and 10 ℃. Below, soil temperatures down to 0.5 m were between 5 and 0.1 ℃. Then there was a small belt with temperatures around 0 ℃. The soil temperature in 0.5 to 1 m depth were between –0.1 to –5 ℃ and rapidly started to dominate the entire soil domain until mid-December. The thermal regime of the snow started to develop with the drop in air temperature below 0 ℃ at the end of September. Associated was the change from liquid to solid precipitation, which implied the onset of the snow cover at the end of September/beginning of October.

In the growing snowpack from October to November, temperatures between –0.1 and –5 ℃ were measured. Beginning in November, the snow temperatures began to drop following the decrease in air temperature to between –35 and –40 ℃ in December. A curtain structure developed within the snowpack, where the upper snow layers showed faster cooling than the lower layers near the soil surface. In the beginning of January, the coldest snow temperatures were measured between –40 and –50 ℃. This coldest period of the winter season lasted until the end of March and then snow temperatures slightly started to increase again following an increase in air temperature roughly until the beginning of May (–20 to –15 ℃). Further increase in the air temperature induced warming in the snowpack (–15 to –10 ℃) until the beginning of June in each year. The last increase in temperature (up to –0.1 ℃) occurred during the short period until the air temperature reached 0 ℃ and the snow melt took place (mid-June).

The snow temperature was largely determined by the air temperature. Yet, cooling events (–30 to –50 ℃), which were found to affect the upper part of the snowpack were not transferred to the basal snow layer below 0.1 m and did not reach the soil. It was only in the 2014/2015 season that soil temperatures dropped to –20 to –25 ℃. In all other years, winter soil temperatures remained between –15 to –20 ℃.

In contrast to the early temperature fluctuations (October to December) within the snowpack, the thermal regime of the ground stayed stable until mid-December and within a temperature range from –0.1 to –5 ℃. In December soil temperatures started to decrease due to lower air temperatures and a thin snow cover between 0.3 m in 2014/2015 and 0.4 m in 2017/2018. The first drop was in the middle of December (–5 to –10 ℃). It was followed by a second decrease (–10 to –15 ℃) in early January. Both reached 1 m soil depth. As within the snowpack, a curtain pattern occurred in the soil domain.

The upper soil layers reacted faster to temperature decrease than the lower parts. In the upper soil layers, a third decrease in temperature started to happen around January when the decreasing snow temperatures slowly reached the soil surface, leading to the lowest soil temperatures for the entire soil column (–15 to –20 ℃), which reached the lower soil domain between February and March. The time and penetration depth of the low temperatures within the deeper soil domain were strongly variable for each season. Common to all was the abrupt temperature increase in mid-April/beginning-May, followed by a period of temperatures between –15 to –10 ℃ until June and then further warming until it reached again the dominating temperature range (–0.1 to –5 ℃). Only the upper part of the soil (0 to –0.4 m) experienced further warming (up to 0.1 to 5 ℃), closely tracking air temperatures. In the soil layers near the surface, maximum temperatures of up to 20 ℃ were measured in the summer of 2017/2018.

The first winter season in 2014/2015 had the shallowest snow cover with a maximum snow depth of 0.51±0.04 m (Tab. 3). During the core winter zone (December to March) the lowest surface snow temperatures were between –30 and –40 ℃ and in February and March temperatures between –20 to –25 ℃ reached the soil to a depth of 0.4 m. Temperatures in this range were only recorded in the soil in this year. In this season, the soil domain was characterized by the longest period with temperatures between –15 to –20 ℃ from the end of December to mid-May. Occasionally, during the summer period, in the upper soil layers (down to 0.2 m) positive temperatures in range of 10 to 15 ℃ were measured. The ALTD at the end of the season (end of August) was about 0.5 m deep.

The maximum snow depth in the snow season 2015/2016 was 0.63±0.03 m and the lowest surface temperatures were between –40 to –50 ℃. The temperature minimum within the basal snow layers (between –20 to –25 ℃) during the core winter zone did not reach the soil domain. The coldest temperatures within the soil were measured from February to the beginning of May (–15 to –20 ℃). The ALTD at the end of the summer was shallow and did not exceed 0.3 m. In the upper soil layers temperatures between 5 and 10 ℃ were found mostly during August.

In snow season 2016/2017 the maximum snow depth was 0.71±0.05 m and the coldest surface temperatures were between –40 and –50 m. In contrast to the other seasons, the core winter zone was shorter and followed by an early warming period due to an increase in air temperature. The snowpack temperature directly increased to a temper-

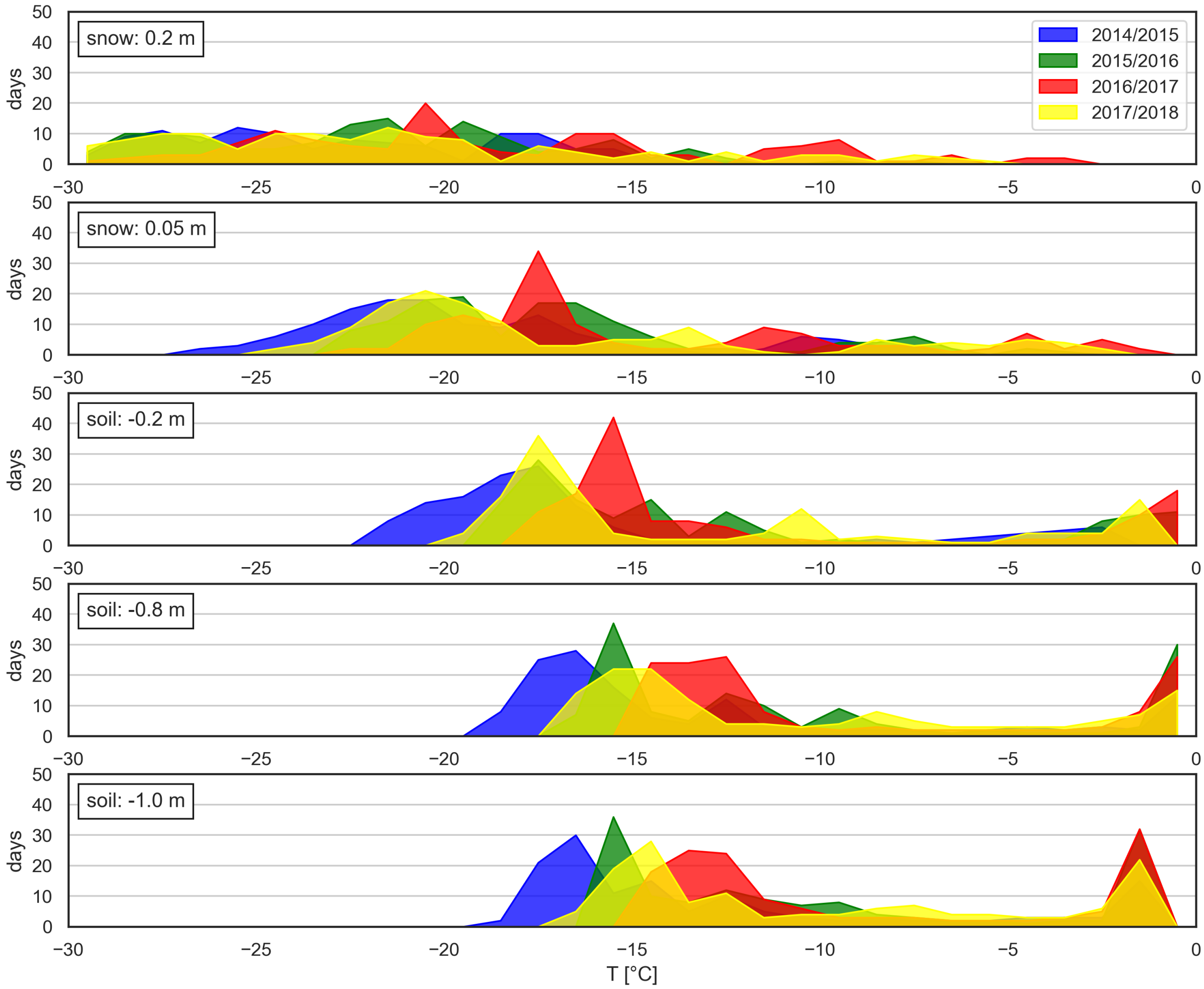

Figure 15: Temperature distribution in 0.2 and 0.05 m (snow) height as well as 0.2, 0.8 and 1 m soil depth for all years (2014 to 2018). The y-axis is the number of days when temperatures were measured.

ature between −10 to −0.1 ℃. This season did not have the first warming trend (temperatures between −20 and −15 ℃) which occurred in the other seasons and which lasted until the beginning of May. Hence, the period with snowpack temperatures between −20 to −15 ℃, which were able to reach the soil domain, was not only significantly shorter, lasting from January to mid-March (usually from January until May), but also soil layers below 0.8 m were not affected by the minimum temperatures. The ALTD in late August was about 0.5 m and the highest temperatures in the upper soil throughout the summer were between 10 to 15 ℃.

The last season (2017/2018) had the deepest maximum snow depth of 0.74±0.05 m.

The lowest snow temperatures in the upper snowpack were between –40 and –50 °C and the minimum temperature range for the soil was –15 to –20 °C. The duration of this low temperature period was similar to the first two seasons. The highest summer soil temperatures with periods in June between 15 and 20 °C down to 0.2 m soil depth were measured in this season. The ALTD reached about 0.6 m.

To better visualize the depth-depended temperatures differences for each year, I plotted the temperature abundances (from 11 November to 31 March for each year) in the snow (0.2 and 0.05 m height) and soil (0.2, 0.8 and 1 m depth) in Fig.15. In the first year (2014/2015), which had the shallowest maximum snow depth (0.51 m, Tab. 3), temperatures down to –20 °C characterized the soil domain down to –1 m. It was followed by the 2015/2016 and 2017/2018 seasons (with a maximum snow depth of 0.62 and 0.74 m, respectively) were soil temperatures around –17.5 °C occurred down to 1 m depth. In 2016/2017 the soil temperatures in 1 m depth were higher (–15 °C) despite a maximum snow depth of 0.71 m similar to the 2017/2018 season. In general, the temperature signal in the basal snow layer (0.05 m) already showed the distribution pattern which reached the deeper soil in 1 m. Furthermore, the data showed that a shallow snow depth resulted in the lowest ground temperatures, but a deep snow depth did not necessarily result in the highest ground temperatures (Fig.15).

3.3 Snow density

This chapter is about the inter-annual variability in the density evolution and SWE, respectively. A slight decrease in density was observed from 236 kg m^{-3} in 2016/2017 to 204 kg m^{-3} in 2019/2020 (Fig.16 (a)). Within the four years, the highest ρ_{bulk} was found in the snow season 2016/2017 (236±67 kg m^{-3}, Tab.4). The highest EOS SWE (148±3 mm) was also recorded in the snow season 2016/2017. The lowest EOS SWE was measured in 2018/2019 (83±2 mm). This correlated with the maximum snow depth results (Tab.3).

3.3.1 Seasonal variability

In this section, I am presenting the results of the seasonal snow density and temperature gradient analyses from 2016 to 2018. Both seasons overall showed the same pattern. The temperature gradient had the highest fluctuations when the snow cover was less than 0.2 m (20 to 200 K m^{-1} in 2016/2017; 5 to 100 K m^{-1} in 2017/2018). This period

Table 4: EOS ρ_{bulk} and EOS SWE results for 2016 to 2020. The micro-topographical location is the centre of the LCP complex. The mean EOS snow depth (Tab. 3) was used to calculate the EOS SWE.

season	**location**	ρ_{bulk} [kg m^{-3}]	ρ_{std} [kg m^{-3}]	SWE$_{\text{mean}}$ [mm]	SWE$_{\text{std}}$ [mm]
16/17	centre	236	67	148	3
17/18	centre	215	116	129	6
18/19	centre	213	54	83	2
19/20	centre	204	50	108	2

was about one month in 2016/2017 and only a few days in 2017/2018. In 2016/2017 with beginning-December the temperature gradient slowly decreased throughout the season to 0 K m^{-1} by beginning-March. In the second year (2017/2018) when the snow depth stagnated for about a month from mid-October to mid-November, the temperature gradient showed a slight increase up to 100 K m^{-1} and afterwards started to decrease throughout the season until it was about 0 K m^{-1} by mid-March (Fig.17).

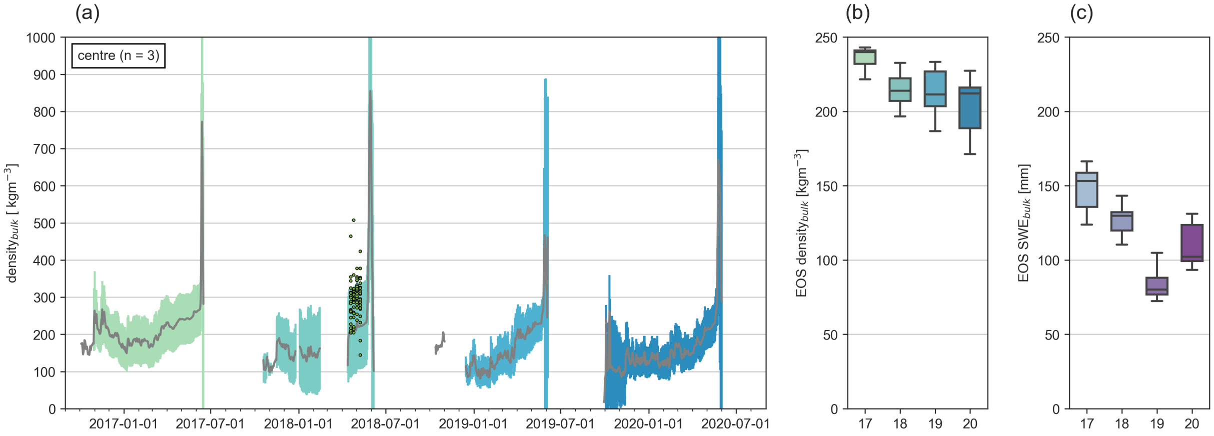

Figure 16: The snow density was measured in three (n = 3) different heights (0.05 m, 0.15 m and 0.25 m) and averaged to obtain the bulk density ρ_{bulk} (a), where grey indicates the mean density and shades of blue, the standard deviation for each year. The manual density measurements (green dots) were taken in the 2018 spring campaign (Tab.7 and Tab.8) and were not located in the snow station's LCP complex. The EOS ρ_{bulk} is displayed in (b). The mean snow depth (Tab.3) measured by the sensors above the centre of the LCP complex was used to calculate the EOS SWE (c).

As the temperature gradient, the snow density showed an inter-annual as well as a seasonal variability. In the first season, the initial density measured by the SPA- 2 sensor mounted in 0.05 m height was between 150 kg m^{-3} and 200 kg m^{-3} from October to December. By end-December, the density started to decrease to 100 kg m^{-3} in beginning-January. From January there was a stagnation until beginning-March, when the density increased again to 200 kg m^{-3} by mid-June (melting period). This last increase in density was contemporaneous with an increase in snow depth from about 0.5 m in March to the maximum snow depth of the season, about 0.7 m. The SPA-2 sensors mounted at 0.15 and 0.25 m started recording the snow density in mid-November, when the snow depth abruptly exceeded 0.25 m, covering both sensors. There was a short but prominent period with alternating values in the second half of November, which probably occurred due to the still existing air signal influence. Both sensors followed the same density evolution pattern of the 0.05 m sensor, but the initial density was almost twice as high (250 kg m^{-3}). The TDR measurements (soil station nearby) measured a similar snow density as the upper SPA-2 sensors between November and March (around 200 kg m^{-3}). The slightly lower values during November can be explained with the spatial variability, which probably also caused the disagreement of about 50 kg m^{-3} from March to June between the sensors. All sensors showed a strong signal of the snow melt event.

During the snow season 2017/2018 the lower SPA-2 sensors (0.05 and 0.15 m depth) were covered in snow (0.2 m) by beginning-October but started recording a snow density about 100 kg m^{-3} not before mid-October due to technical failure (Fig.17). Contemporaneous with an increase in snow depth to 0.4 m in mid-November, the density also increased up to 150 kg m^{-3}. Also, the upper SPA-2 strap sensor in 0.25 m started to record density measurements (around 250 kg m^{-3}). With beginning-December until mid-February, the lower strap sensors showed a slight decrease in density back to 100 kg m^{-3} whereas the upper strap sensor recorded an increase in density up to almost 300 kg m^{-3}. Due to technical failure, there were no measurements between mid-February to mid-April. The density in the lower snowpack increased up to almost 200 kg m^{-3} by the end of the season. In the upper snowpack the density was almost twice as high (360 kg m^{-3}). All strap sensor clearly recorded the melting in beginning-June. Furthermore, the manual bulk density field measurements (green dots in Fig.17) obtained during the spring campaign in April/May 2018 (Tab.7 and 8) were in the same range as the automated density measurements even though they were not located in the same LCP complex.

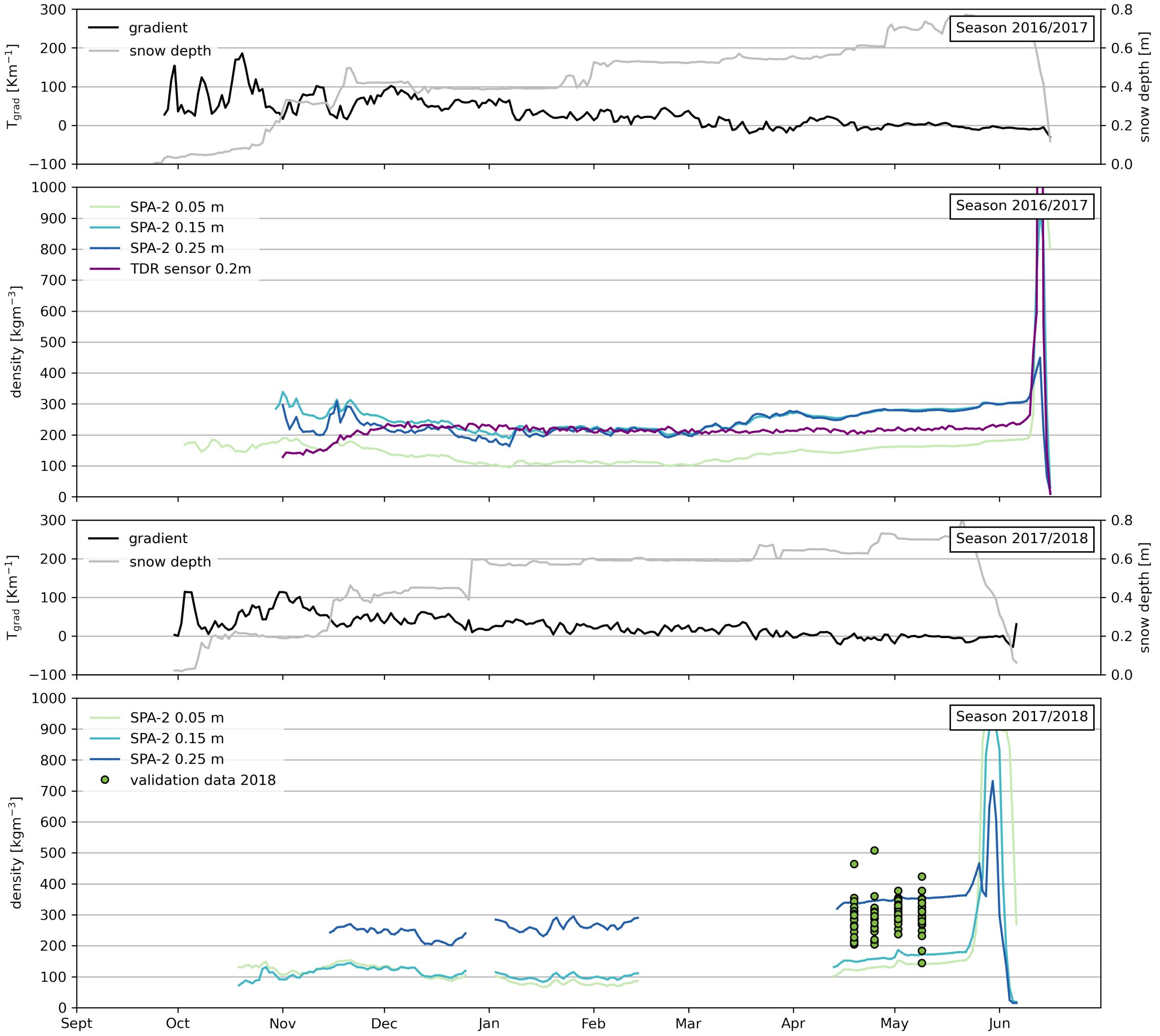

Figure 17: Snow density profile (SPA-2 strap sensors in 0.05, 0.15 and 0.25 m height and TDR sensor in 0.2 m height at the soil station) and temperature gradient (between 0.8 m air temperature and −0.05 m soil temperature) for the snow seasons 2016/2017 and 2017/2018. The values are daily averages. Green dots are the manual bulk density measurements obtained during the 2018 spring campaign (Tab.7 and Tab.8). The field observations were not located in the snow station's the LCP complex.

Five manual measurements were higher (380 to 500 kg m^{-3}) than the automated measurements. They were obtained in profiles with a snow depth less than 0.16 m. Nevertheless, overall the SPA-2 data set was in the same range as the manual measurements in 2019 and also showed a good agreement with the TDR data set from the soil station in 2016/2017. The comparison of the two seasons particularly revealed a high inter-annual variability of the basal low density layer, which did not exceed 0.05 m in 2016/2017, but was about 0.15 m in 2017/2018. In context of the snow profile picture of a grass-centre in Fig.6 (b) I identify the basal layers which had a density between 100 and 200 kg m^{-3} as depth hoar.

3.3.2 Snow - soil interactions

In this section, I am providing the results which show the snow-soil interactions i.e. processes that potentially had an influence on the deviation in the basal depth hoar layer thickness. In detail, I investigated the seasonal variability of the uppermost soil temperature (0.05 m depth) in combination with the snow density evolution for the two seasons 2016/2017 and 2017/2018.

Furthermore, I studied the connection between the soil VWC and the density evolution of the lower SPA-2 strap sensor (0.05 m) for the season in 2016/2017. In the relationship between the soil temperature in 0.05 m depth and the snow density evolution for the three SPA-2 straps, there was a two-step decrease pattern starting in December (Fig.18). First, along with a decrease in soil temperature to –12.5 ℃, the density decreased (about 50 kg m^{-3}) until the end of December where in all plots I found a short stagnation period. Then the second decrease in temperature (to –16 ℃) started, and also the density decreased (less than 30 kg m^{-3}) until it reached a steady state again in January.

For the snow season 2016/2017 the major part of this two-step decrease in snow density and soil temperature took place in December, whereas in the 2017/2018 season it was in extended throughout January. This was probably because of a different snow depth evolution. In beginning-January in 2017/2018 the snow depth increased from about 0.4 m to 0.6 m and extended the decreasing period. The snow depth during the same period in 2016/2017 was constant with about 0.4 m Fig.17). Both seasons showed similar patterns towards the melting period. From February to March the snow density stayed constant with low soil temperatures between –17.5 and –15 ℃. The increase in both variables started again in the end of March with warming soil temperatures. At the end of each season, the soil temperatures were around –10 ℃.

In order to study a possible connection between soil moisture and snow density, I analysed the volumetric water content in combination with the snow density for the snow season 2016/2017 (Fig.19). I plotted the VWC at 0.14 and 0.44 m depth, together with

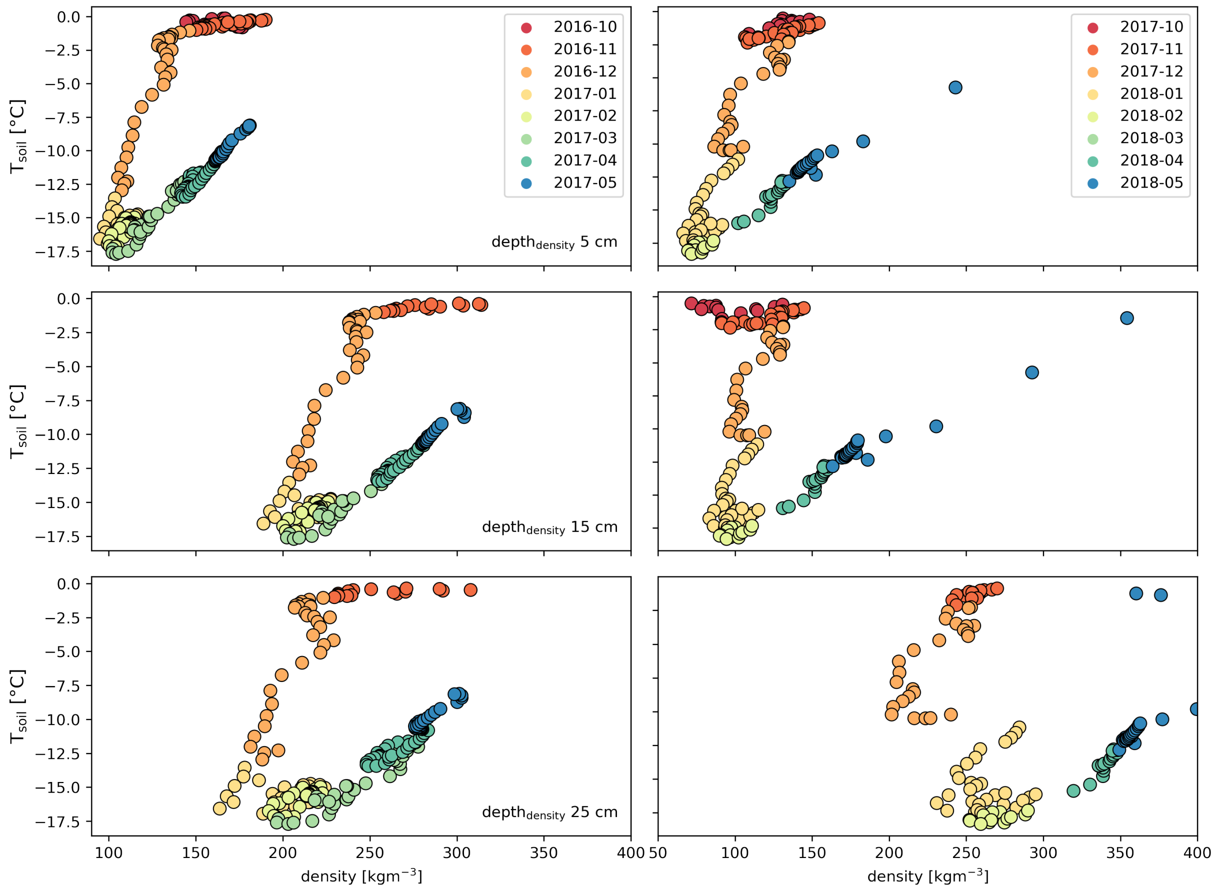

Figure 18: Scatter plot of soil temperature at –0.05 m depth and all three SPA-2 density sensors (0.05, 0.15 and 0.25 m above the soil surface), in the season 2016/2017 (left) and 2017/2018 (right). The colours represent the months of each season.

the snow density at 0.05 m above the ground, from October to April. In October the VWC close to the surface was about 90 % whereas it was only 70 % in 0.44 m depth. The density fluctuated between 150 and 190 kg m^{-3}. With beginning-November, the VWC in both layers abruptly decreased, to about 5 % for the sensor close to the surface and to about 20 % for the sensor deeper in the soil domain in mid-November. In contrast, the snow density did not start to decrease before December. The density decrease down to 100 kg m^{-3} lasted until the soil freeze-back was completed in mid-January. From mid-January to March, the snow density was steady at around 110 kg m^{-3} and then increased up to 150 kg m^{-3} at the end of April.

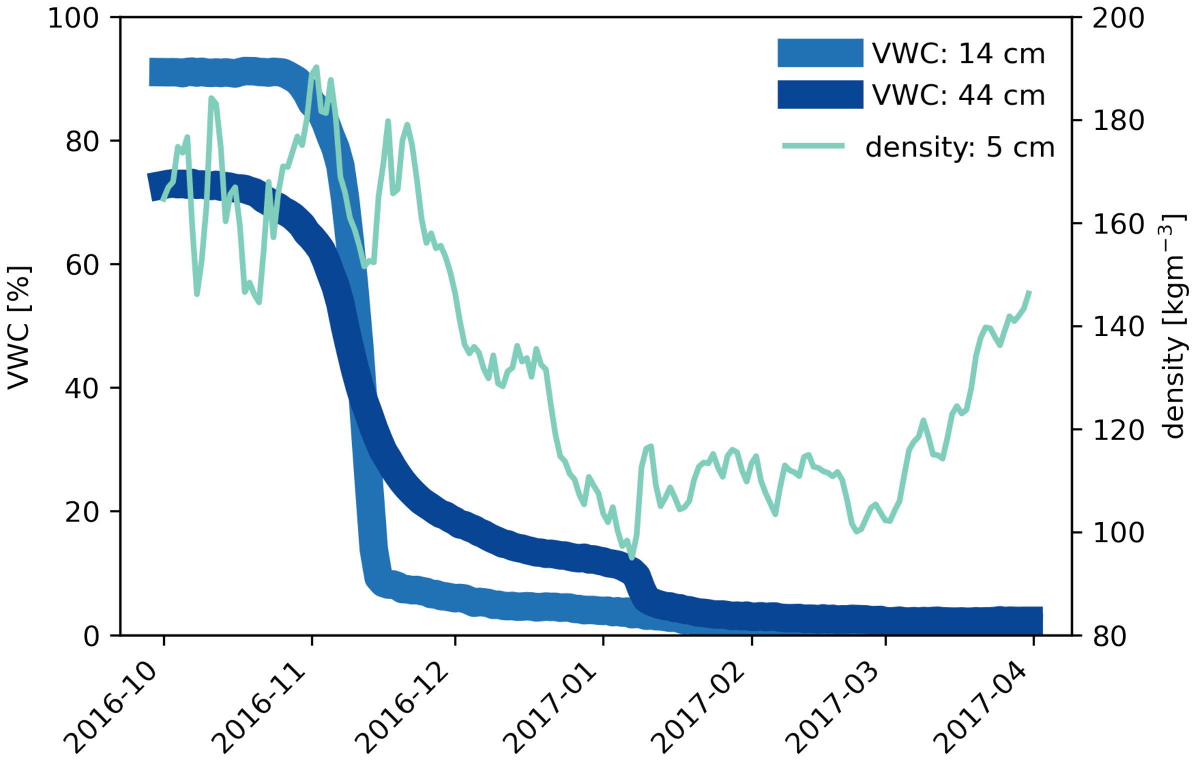

Figure 19: Volumetric water content at 0.14 and 0.44 m soil depth and basal snow density 0.05 m above the ground surface for the snow season 2016/2017.

3.4 Validation model results

The processes described in the upper section are highly complex and unique snow-soil interactions, which are challenging to reproduce with models. Within the following section, I am providing the results of three different ‹CG Community› model runs for an LCP centre. Furthermore, I am presenting the comparison of the model output with the field measurement with what I am assessing the models' ability to process the complex interactions mentioned above. In Fig.20 I displayed the ALTD measurements from 2014 to 2017 and the influence of the different settings for θ_{fc} on the modelled ALTD in the CG Standard Crocus ERA19 run.

The ALTD field data set showed a slight decrease within the four years with a median ALTD of about 0.5 m in 2014 and 2015 and a median of about 0.45 m in 2016 and 2017. The range of about 0.2 m in each year was due to the spatial variability of the measurement grid, which covered a wide range of topographical features (150-point calm grid with 1 m spacing). The inter-annual variability was reproduced by the model

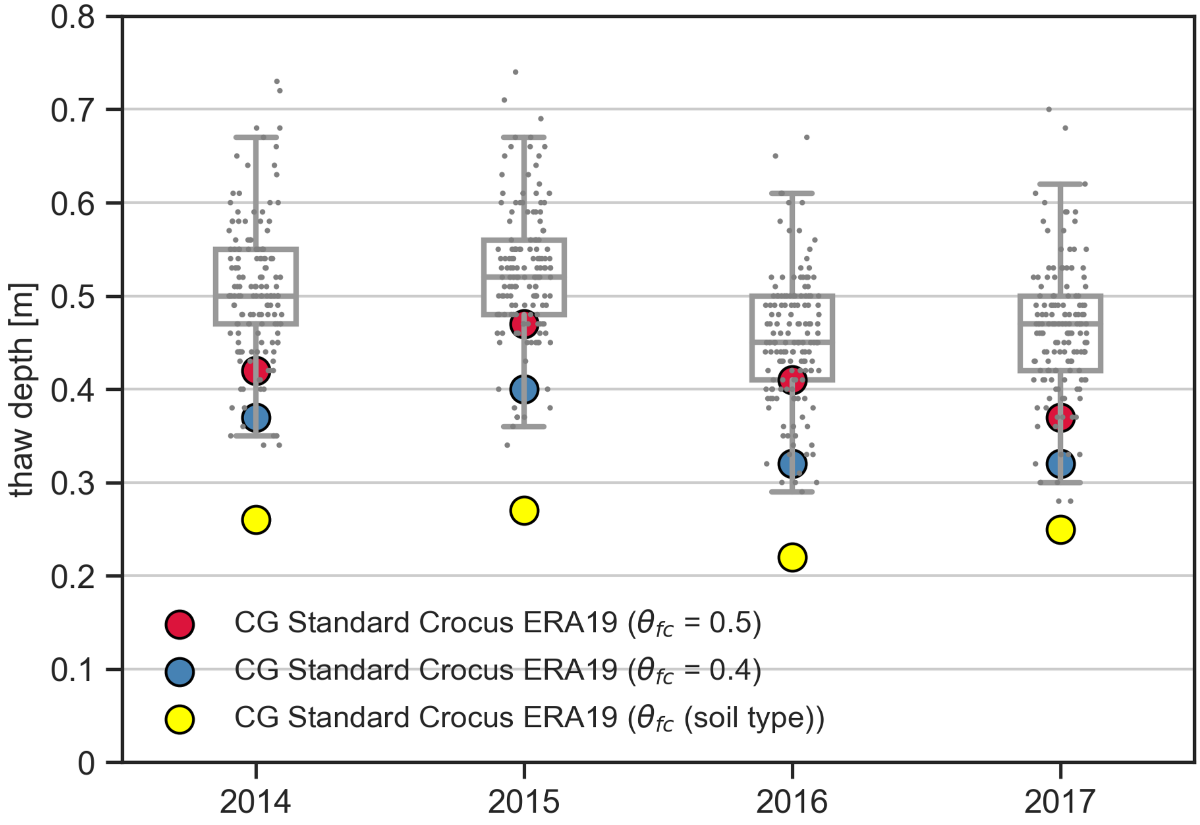

Figure 20: Validation of the modelled EOS ALTD (coloured dots) with manual measurements (grey points and box plots) located in a 150-point grid. The manual measurements cover a wide range of landscape features, whereas the modelled data points only referred to an LCP centre.

independent of the θ_{fc}. If I set θ_{fc} dependent of the soil type (Tab.2) the ALTD was significantly underestimated. A constant θ_{fc} of 0.4 still led to an underestimation of the ALTD but was still within the minimum range of the validation measurements. I achieved the best results setting θ_{fc} to 0.5. Because of this good agreement, I used the value in all three model runs (CG Standard Crocus ERA19, CG Standard Crocus ERA44 and CG Arctic Crocus ERA19).

To investigate if the model runs were able to generate the snow cover extent, I plotted all snow depth courses against the mean snow depth measured with the five sensors located in the LCP centre of the snow station (Fig.21). In all four years, the CG Standard Crocus ERA19 model run best matched the measured snow depth, even briefly following the inter-annual variability of the measured snow depth. The CG Standard

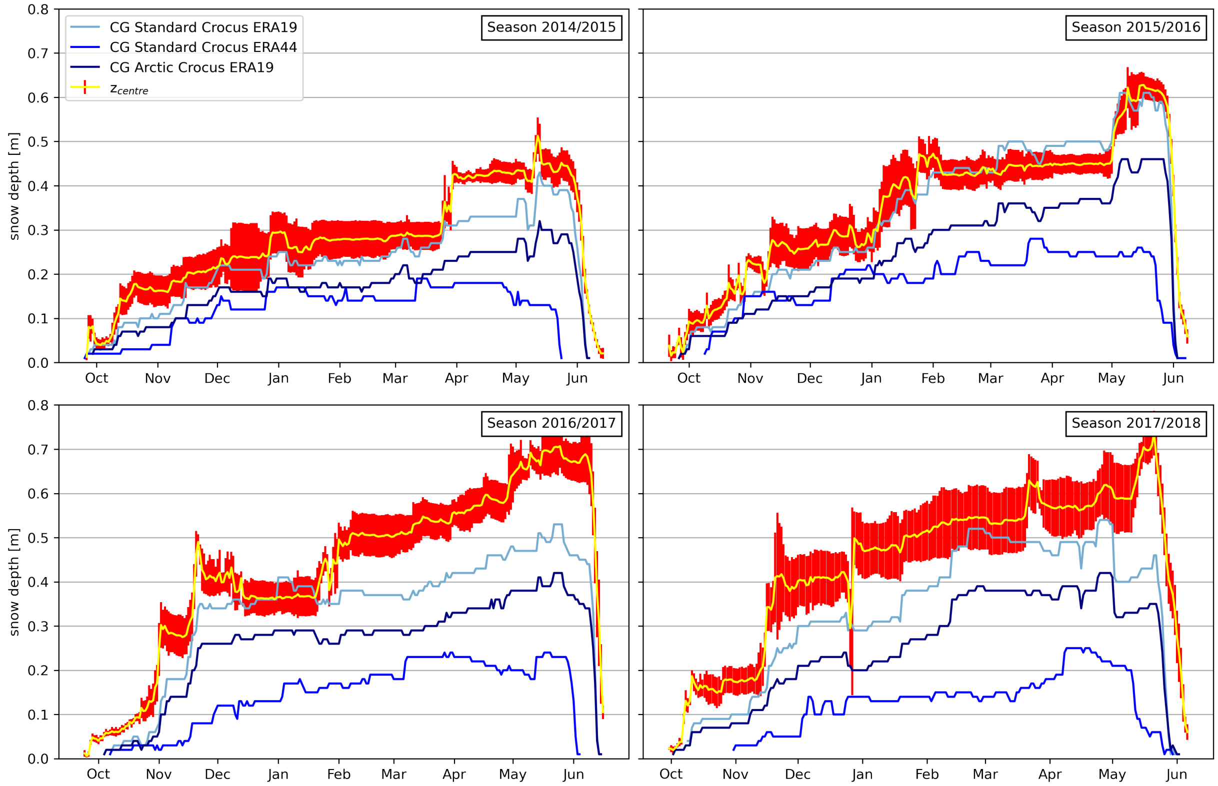

Figure 21: Validation of the modelled snow depth with the average snow depth measured by the five snow depth sensors in the LCP centre (daily averages). The yellow line indicates the average of the five centre sensor measurements and red is the standard deviation.

Crocus ERA44 and CG Arctic Crocus ERA19 model runs showed a poor agreement as the snow depth was too shallow by a factor of three for the seasons 2016/2017 and 2017/2018 and a factor of two for these season, respectively. Also the EOS snow depth was underestimated by the model runs. Only in the 2015/2016 season, the CG Standard Crocus model run produced similar values (0.54±0.05 m) as measured with the sensors (0.51±0.03 m).

I summarized the results of the modelled EOS snow depth in comparison to the measured EOS snow depth in Tab.5. In terms of the snow cover evolution the CG Standard Crocus ERA19 and the CG Arctic Crocus ERA19 model runs generated a better timing of the onset and melting period than the CG Standard Crocus ERA44 run. In the latter, not only was the onset in poor agreement with the sensor data (i.e. November instead October in 2017/2018) but also the melting period started to early in 2014/2015 and 2016/2017. In general, the modelled snow depth evolution (CG Standard Crocus

ERA19 and the CG Arctic Crocus ERA19) followed the course of the measured data but the inter-annual variability of the agreement was still high. In 2014/2015 the two runs were not only able to reproduce the seasonal evolution of the snow depth but also generated specific events such as the sudden decrease followed by an abrupt increase in May. Only in 2017/2018 the model runs produced inverted results for the last snow depth increase shortly before the melting started in June.

Table 5: EOS snow depth from the three model runs with standard deviation as well as the EOS snow depth from the snow depth sensors located in the LCP centre of the snow station.

season	**location**	sensor SD [m]	CG Corcus ERA19 [m]	CG Corcus ERA44 [m]	CG Arctic Corcus ERA19 [m]
14/15	centre	0.44±0.03	0.35±0.03	0.15±0.02	0.26±0.02
15/16	centre	0.51±0.03	0.54±0.05	0.25±0.01	0.4±0.04
16/17	centre	0.63±0.04	0.47±0.02	0.2±0.01	0.37±0.02
17/18	centre	0.6±0.06	0.46±0.06	0.21±0.05	0.36±0.04

3.4.1 CG Standard Crocus ERA19

In the following sections I am providing a more detailed comparison between the modeling results of the three different model runs and the automated measurements (snow depth, snow and soil temperature and density). The first CG Standard Crocus ERA19 run had the best agreement with the automated measurements in all compared parameters. There was a deviation in the snow depth of about 0.1 m (RMSE) with an underestimation in the generated snow depth (MBE: –0.1 m Tab.6).

Table 6: RMSE (MBE) for all three model runs for snow depth [m], density [kg m^{-3}], snow temperature [K] and soil temperature [K]. Time period depth and temperature: derived from the snow season begin and end dates from the automated snow measurements. Time period density: 15 October to 31 May of each season. Time period soil temperature: 1 September to 31 August of each season. Reference data: snow station.

snow parameter	period	CG Crocus Standard ERA19 RMSE (MBE)	CG Crocus Standard ERA44 RMSE (MBE)	CG Arctic Crocus ERA19 RMSE (MBE)
snow depth	2014 - 2018	0.1 (-0.1)	0.3 (-0.2)	0.2 (-0.1)
ρ	2016 - 2018	91 (39)	99 (51)	140 (104)
T	2014 - 2018	4.6 (-1.1)	7.8 (-4.9)	5.8 (-2.7)
T_{soil}	2014 - 2018	2.8 (-0.5)	5.0 (-2.6)	2.9 (-1)

The snow temperature deviation was 4.6 K (RMSE) with the model producing lower temperatures (MBE: –0.1 K). In the CG Standard Crocus ERA19 run the lowest snow surface temperatures between –50 to –60 ℃ were generated in the same months as they occurred in the measurements between December and April. The modelled temperatures were 10 ℃ lower than the measured values (Fig.22).

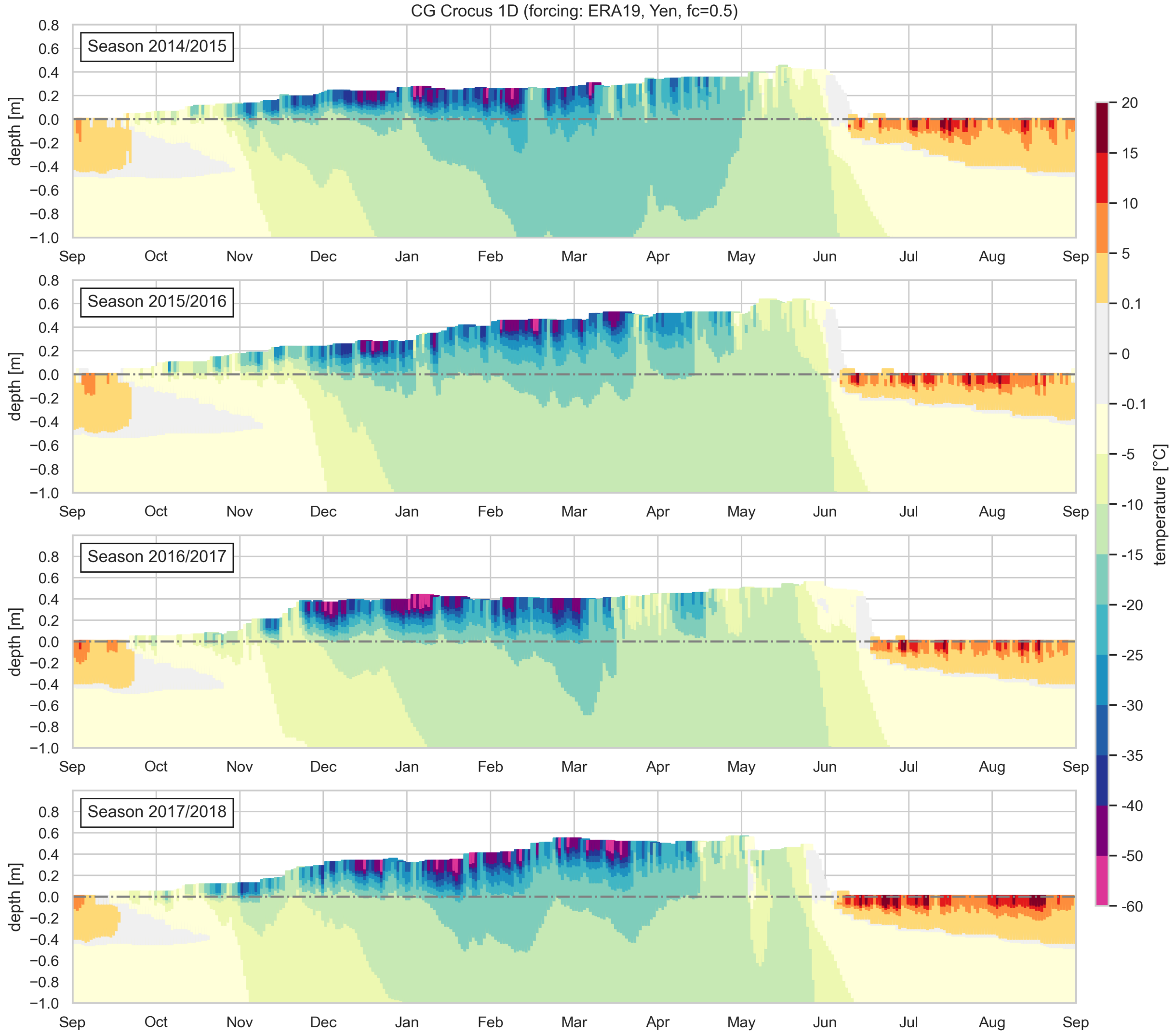

Figure 22: Thermal profile (snow and soil) for the model run CG Standard Crocus ERA19 for the years 2014 to 2018. The dashed grey line indicates the ground surface. The discrete colour bar was set up with the same steps as in Fig.14 with the thermal profile from automated measurements.

Short-term warming spells at the end of November in 2016/2017 and 2017/2018 were transferred through the snowpack and led to a delayed freeze-back of the soil regime. This effect was not observed with the soil temperatures sensors. The soil temperature deviation was about 3 K (RMSE) with a slight temperature underestimation in the modelled temperatures of −0.5 K (MBE). The modelled results showed the same general temperature pattern as the sensor data set with a delayed cooling of the ground during the onset of the snow season. However, the model generated a curtain structure within 0.1 to 0.45 m soil depth with temperatures between −0.1 to 0.1 ℃ (from mid-September to November) which did not occur up to this magnitude in the measured soil temperature data set for any of the four years. Also, the beginning of the freeze-back was almost a month earlier in all seasons except 2016/2017.

In contrast to the measured values, from January to May low temperatures between −15 to −20 ℃ only reached the deep soil layers below 1 m depth in the first modelled season (2014/2015). For all other years, soil temperatures in this range were only calculated above a soil depth of 0.7 m for this time period. The ALTD was between 0.4 and 0.5 m for all years, which was in good agreement with the measured values. However, in the upper soil layers, down to 0.2 m, scattered events with a temperature range significantly higher than the measured values, from 15 to 20 ℃ were produced. The largest temperature differences between 16 and 20 ℃ occurred in the upper snowpack down to 0.1 m below the snow surface (Fig.23) as the generated model temperatures were lower than the measured temperatures. Within the majority of the lower snowpack, the difference was only between 0 and 6 ℃.

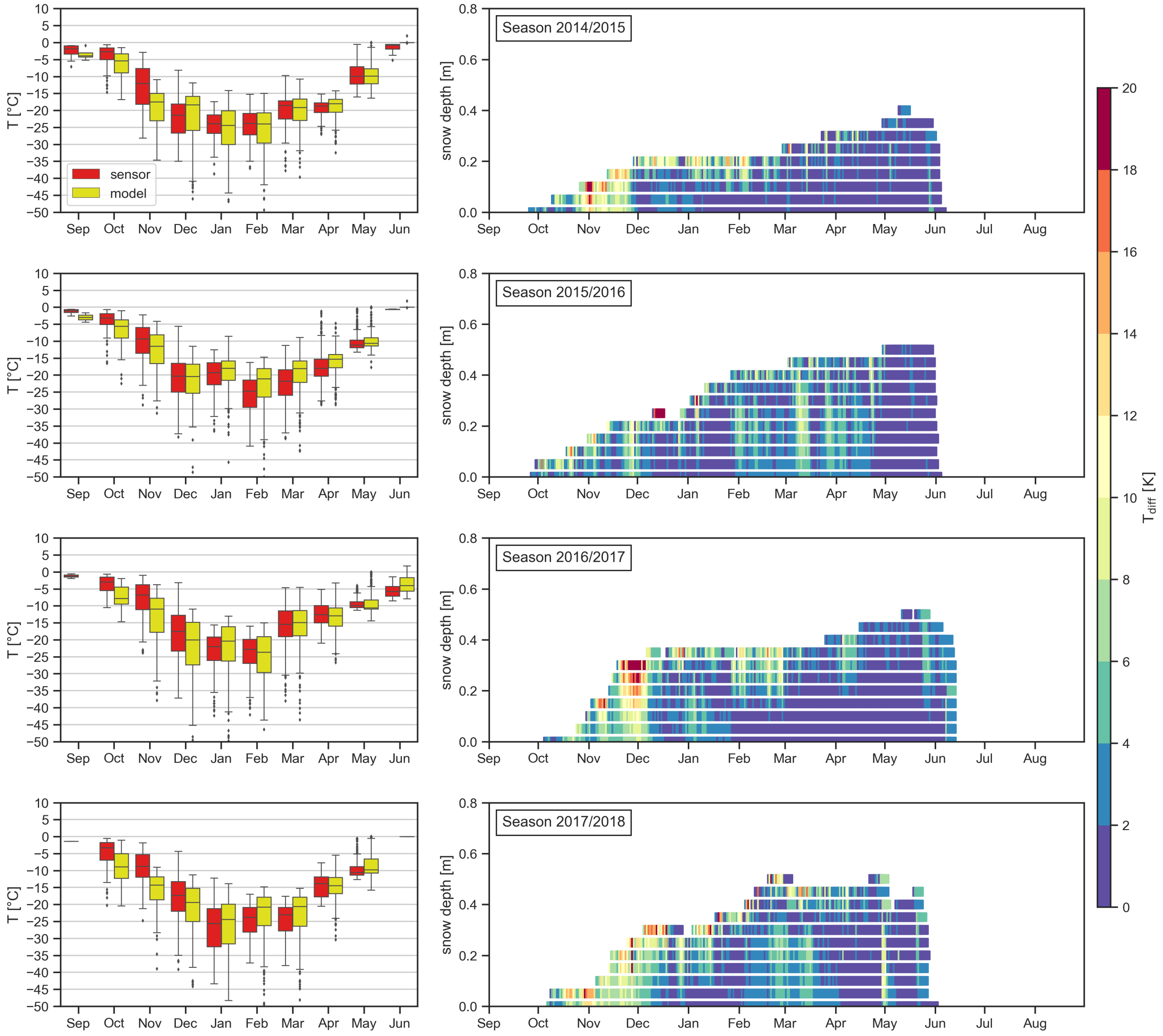

Figure 23: Comparison of temperatures generated by the CG Standard Crocus ERA19 model run and the automated temperature measurements for the years 2014 to 2018. The box plots on the left show the median temperature per month for the measured (red) and modelled temperatures (yellow). T_{diff} is the absolute temperature difference between measured and modelled temperatures within the installation heights of the thermocouples (0 to 0.5 m). The white horizontals are the 0.05 m steps between the thermocouple heights.

The density evolution generated by the CG Standard Crocus ERA19 run showed a deviation of 91 kg m^{-3} (RMSE) compared to the measurements with the SPA-2. The model produced higher densities (MBE: 39 kg m^{-3}). During the onset of the snow season the snow density fluctuated between 150 and 250 kg m^{-3} in all simulated seasons from mid-September to mid-October (Fig. 24). In general, the modelled density profile was characterized by basal layers with a higher density, between 150 and 300 kg m^{-3} and layers with a lower density, 200 to less than 100 kg m^{-3}, in the upper snowpack. During the snow melt period in June, the model generated densities above 600 kg m^{-3}.

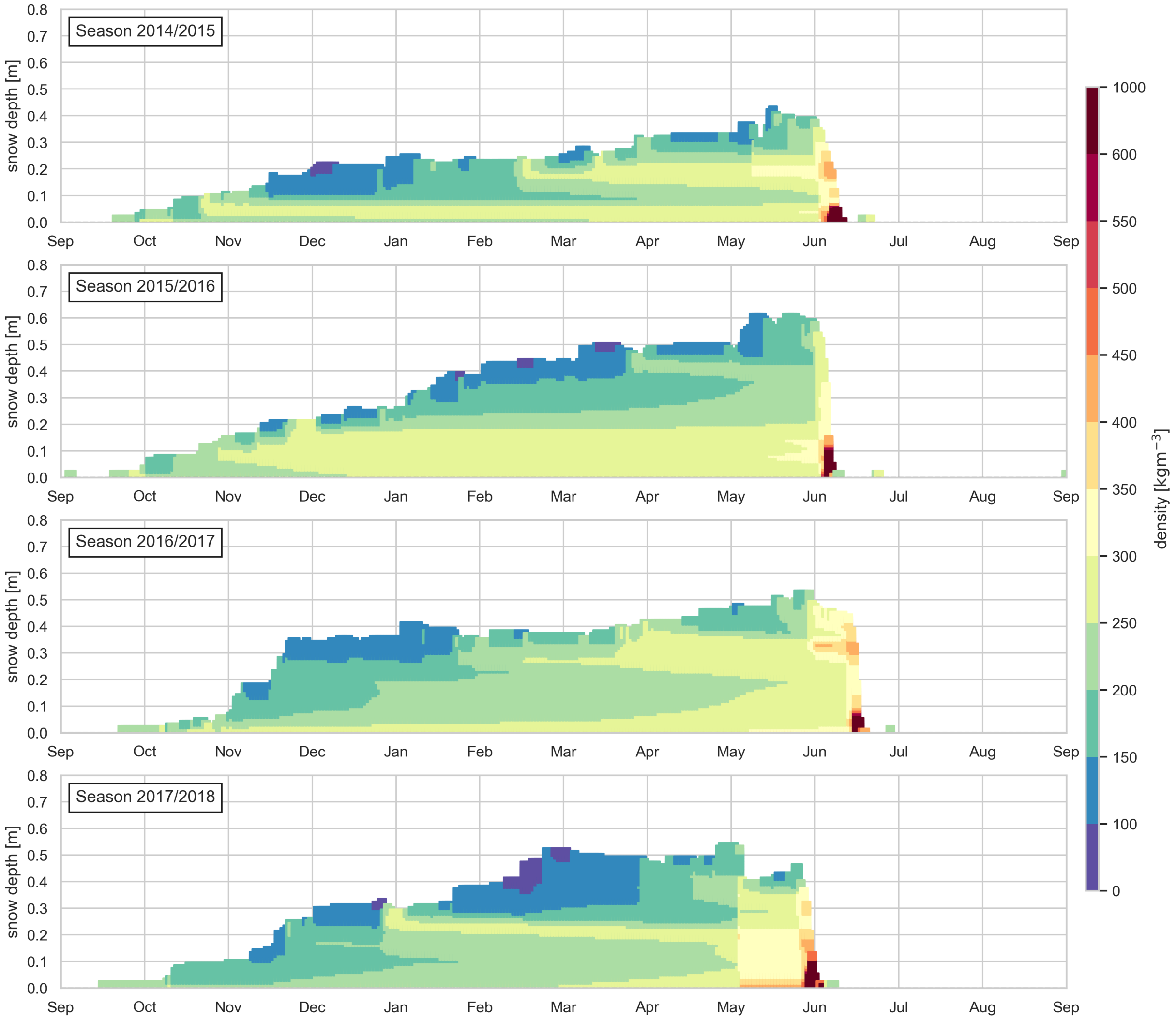

Figure 24: Density profiles for the CG Standard Crocus ERA19 model run for the years 2014 to 2018.

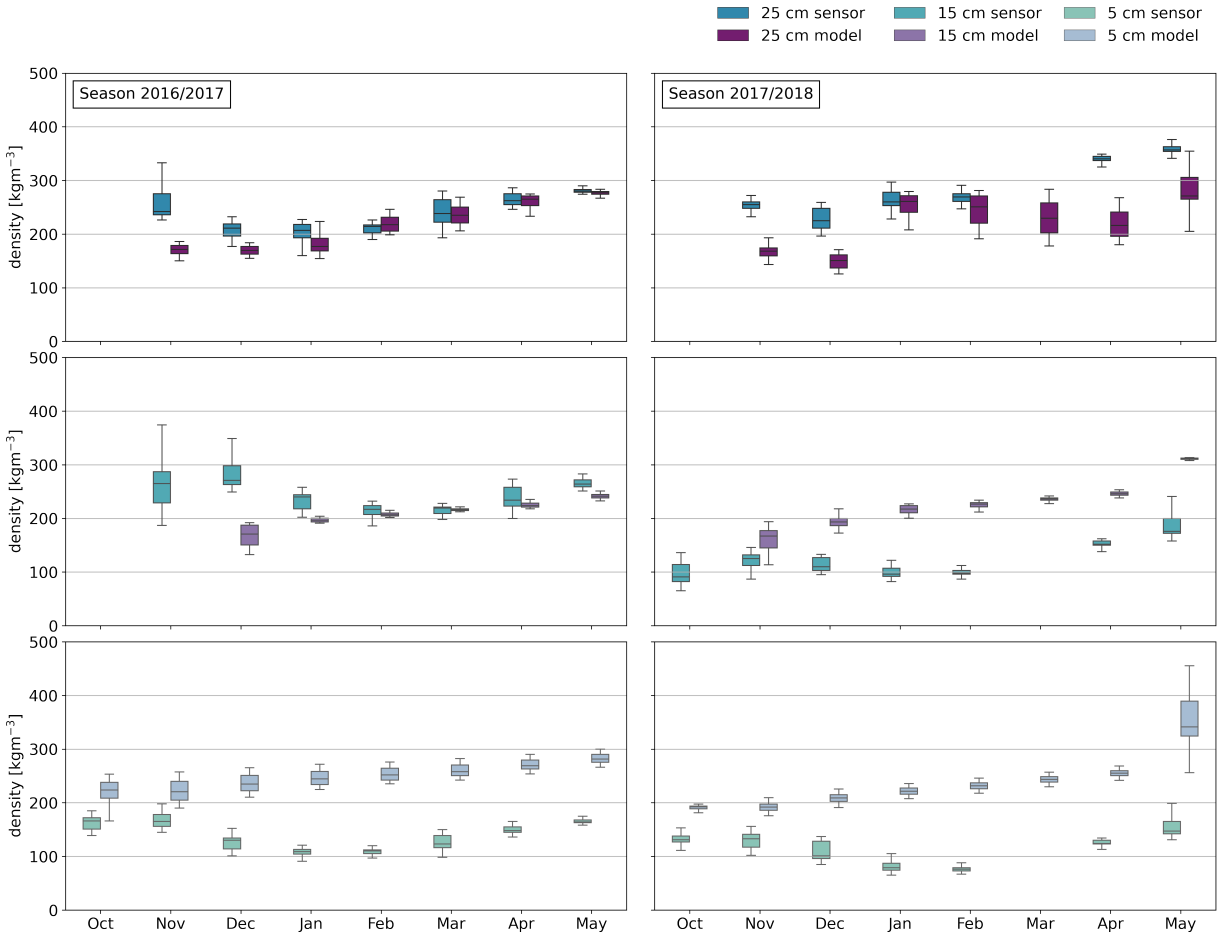

Figure 25: Comparison between the CG Standard Crocus ERA19 model run and automated density measurements from the SPA-2. The density was compared at 0.05, 0.15 and 0.25 m height. Box plots contain the daily averages.

I compared the modelled and measured (SPA-2) seasonal density variation in 0.05, 0.15 and 0.25 m height (Fig.25). In 2016/2017 the modelled density in 0.15 and 0.25 m height was in the same range as the measured density only during November and December there was a significant difference when the modelled density was about 100 kg m^{-3} lower than the measured density. In the lower snowpack in 0.05 m height, the agreement was only good during October and November. With December the model showed a poor performance with densities being twice as high as the automated measurements. The seasonal evolution was reproduced by the model in 0.15 and 0.25 m height but in 0.05 m height the decrease in density from December to February/March was not generated. In the second year, only the modelled density in the upper snowpack (0.25 m) showed a good agreement with the measured data, but significant deviations occurred during the onset of the snow cover in November/December as well as within the melting period in May/June. The deviations were about 100 kg m^{-3}. The densities in the lower snowpack differed significantly as the modelled values were at least twice as high compared to the measured densities from December to May.

3.4.2 CG Standard Crocus ERA44

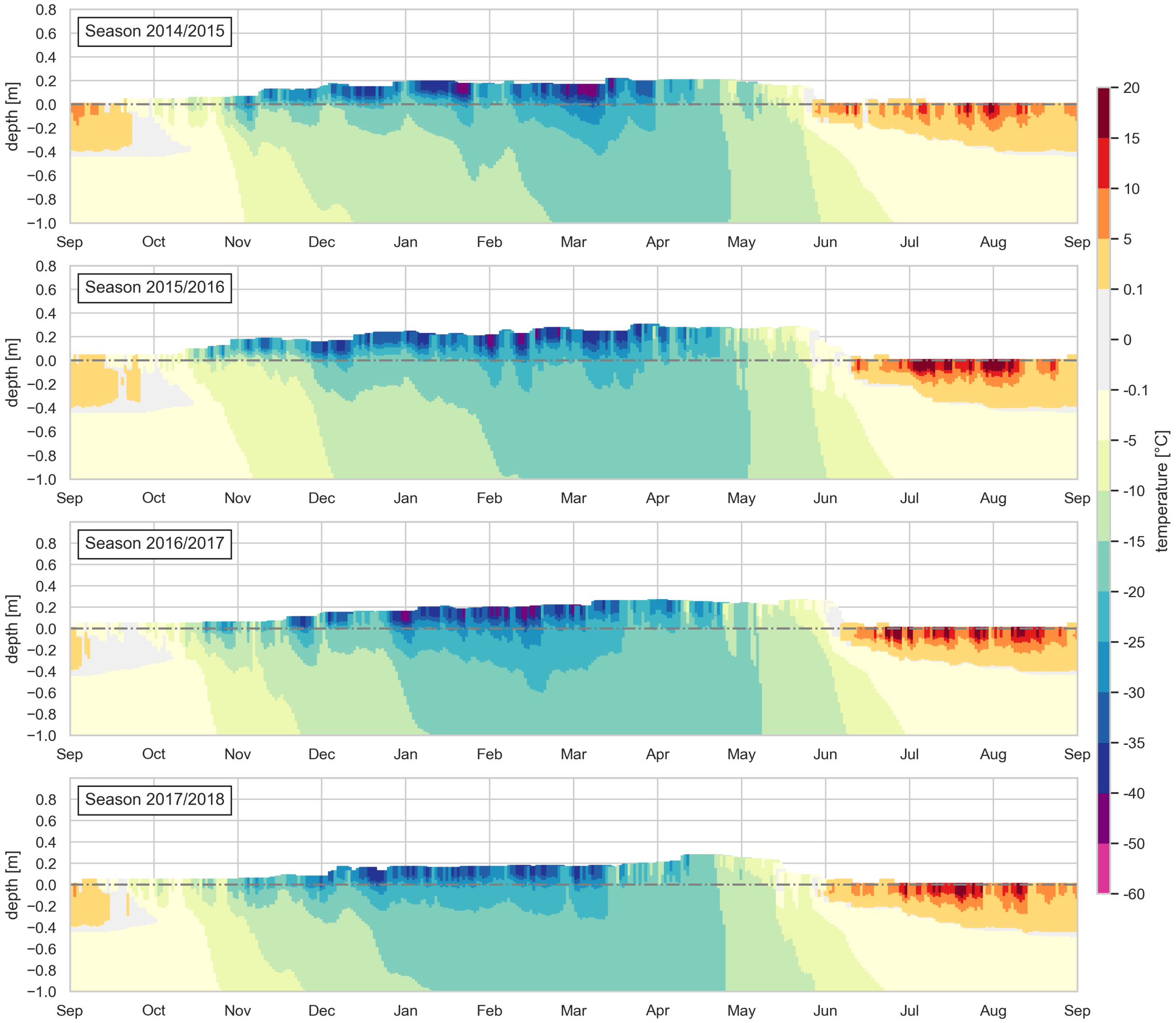

Figure 26: Thermal profile for the model run CG Standard Crocus ERA44 for the years 2014 to 2018. The discrete colour bar was set up with steps similar to Fig. 14.

The second CG Standard Crocus ERA44 run had the worst agreement with the automated measurements in all compared parameters. The deviation in snow depth was 0.3 m (RMSE) with an underestimation in the modelled snow depth (MBE: −0.2 m, Tab.6). The snow temperature deviation was 7.8 K (RMSE) with a large temperature underestimation of −4.9 K (MBE, Tab.6) in the modelled temperatures. In the CG Standard Crocus ERA44 run the lowest snow surface temperatures were in the same range as the measured surface temperatures (between −40 to −50 ℃) and also occurred between December and April (Fig.26). The range was 10 ℃ higher than in the CG Standard Crocus ERA19 runs and were also less abundant. The deviation between the modelled and measured soil temperatures was the highest of all three model runs (RMSE: 5 K, MBE: −2.6 K, Tab.6).

The CG Standard Crocus ERA44 model run had the biggest temperature differences (Fig.27) which was connected to the poor performance of the snow depth calculations. Temperature discrepancies between 6 to 20 ℃ occurred throughout the entire season. The modelled temperatures were lower than the measured temperatures in all month of every season. The density profile generated by the CG Standard Crocus ERA44 run showed a deviation of 99 kg m^{-3} (RMSE) compared to the SPA-2 measurements. The modelled densities were higher (MBE: 51 kg m^{-3}, Tab.6) and the deviation was similar to the CG Standard Crocus ERA19 model run. During the onset of the snow season the snow density fluctuated between 150 to 250 kg m^{-3} in all simulated seasons from mid-September to mid-October (Fig.28).

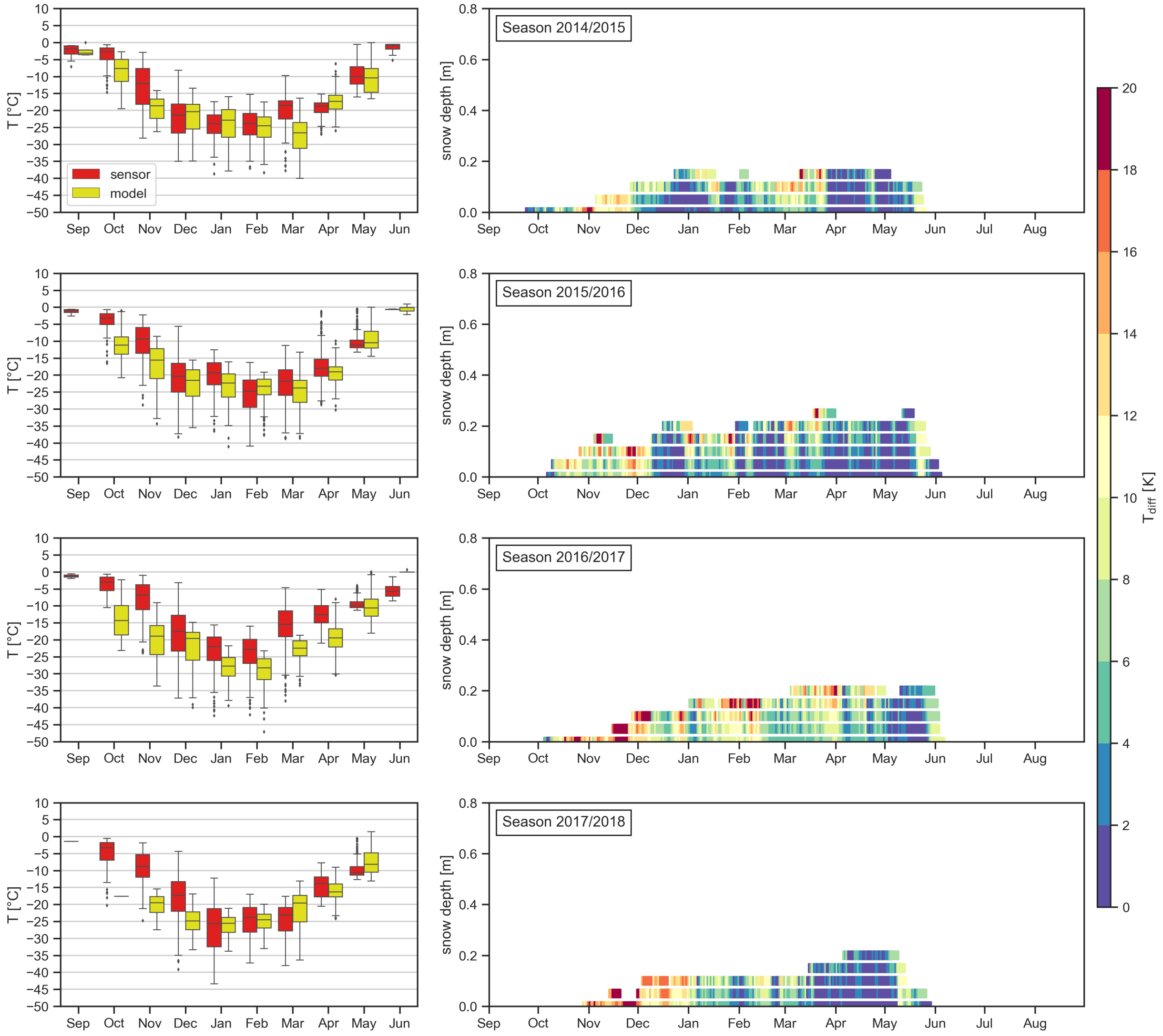

Figure 27: Comparison of temperatures generated by the CG Standard Crocus ERA44 model run and the automated temperatures measurements for the years 2014 to 2018. The box plot on the left show the median temperature per month for the measured (red) and modelled temperatures (yellow). T_{diff} is the absolute temperature difference between measured and modelled temperatures within the installation heights of the thermocouples (0 to 0.5 m). The white horizontals are the 0.05 m steps between the thermocouple heights.

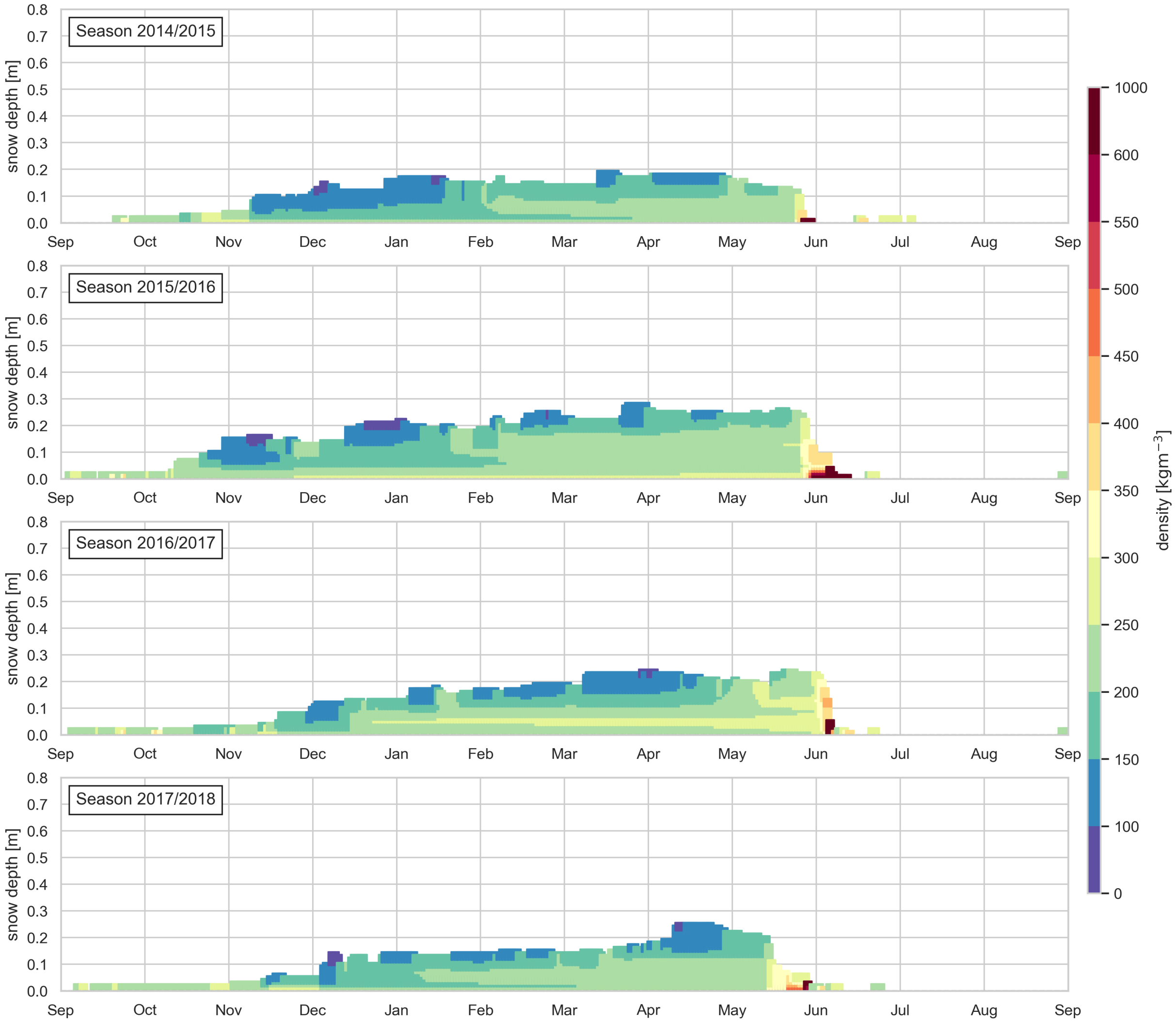

Figure 28: Density profile for the model run CG Standard Crocus ERA44 for the years 2014 to 2018.

In general, the modelled snowpack stratigraphy was as in the CG Standard Crocus ERA19 run characterized by basal layers with a higher density in range between 150 to 250 kg m^{-3} and layers with lower density in range of 200 to less than 100 kg m^{-3} in the upper layers. The temperature pattern of the ground thermal regime showed the start of the freeze-back already by beginning-November, which was about four weeks earlier than in the measured data set. Also in this run the model produced a curtain structure with temperatures around 0 ℃ in September to October which was not observed with the soil temperature sensors.

In the CG Standard Crocus ERA44 model run temperatures between −15 to −20 ℃ reached the soil down to a depth of 1 m from January to May, which was in good agreement with measured soil temperatures and a better fit than in the CG Standard Crocus ERA19 model run. The extent of this cold temperature area grew with each modelled year. The ALTD depth did not exceed 0.4 m for all years which was in good agreement with the measurements. Compared CG Standard Crocus ERA19 model run soil temperature between 15 to 20 ℃ were more frequent in the upper soil layers down to a depth of 0.2 m during the summer period.

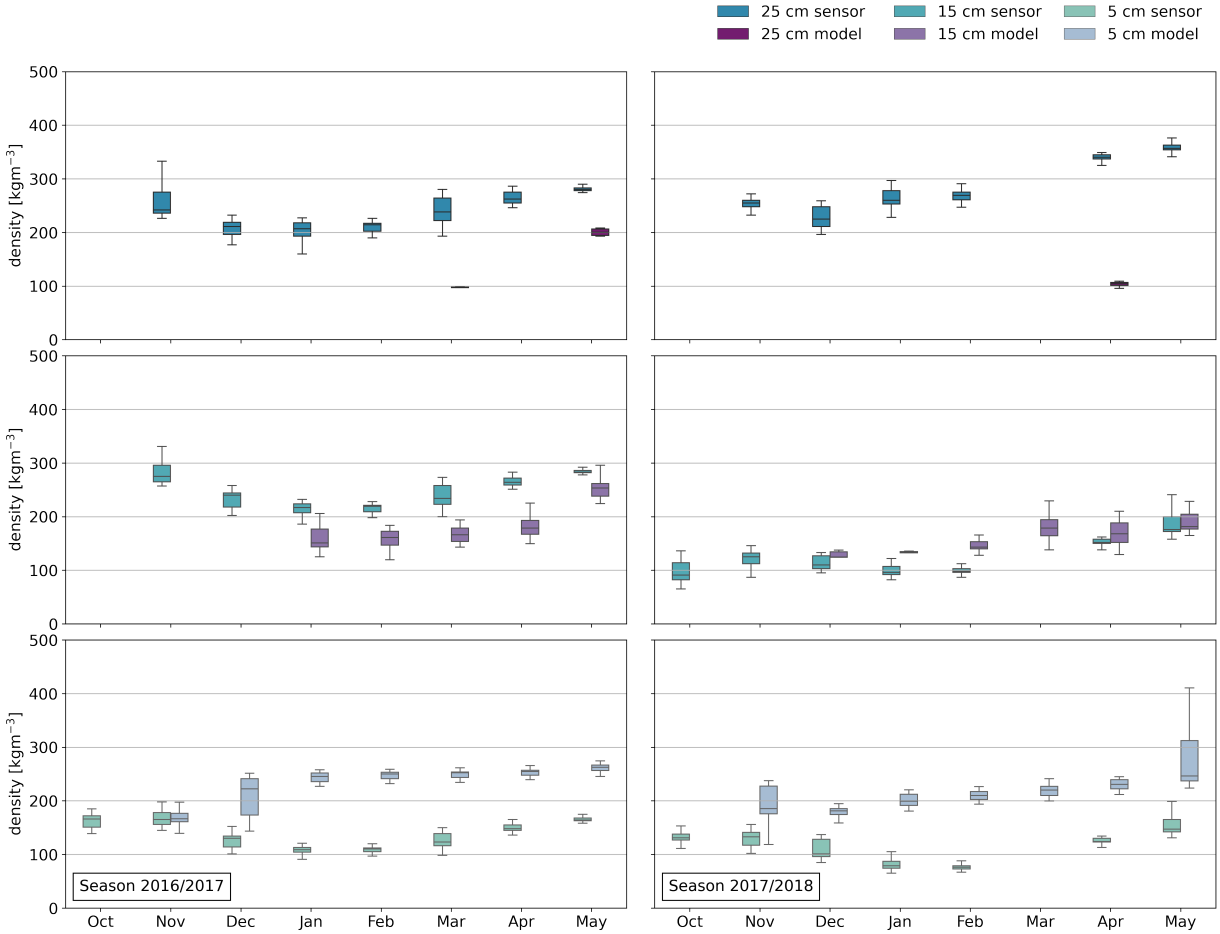

Figure 29: Comparison of the CG Standard Crocus ERA44 model run and automated density measurements from the SPA-2. The density was compared in 0.05, 0.15 and 0.25 m height.

The snow melt period in June was characterized by densities above 600 kg m^{-3}. I compared the seasonal density variation from the modelled and measured snow density (SPA-2) in 0.05, 0.15 and 0.25 m height. The generated density in 0.05 m height only agreed with the measured density in November in both years (Fig.29). The density at 0.15 m height showed good agreement in both years. For the upper sensors there was a very poor agreement as the snow depth in this model run was too shallow (EOS snow depth about 0.2 m, Tab.5) and density in 0.25 m height was barely generated.

3.4.3 CG Arctic Crocus ERA19

The third CG Arctic Crocus ERA19 run had the second-best agreement with the automated measurements in all compared parameters. The deviation in snow depth was 0.2 m (RMSE) with an underestimation in the model results (MBE: –0.1 m Tab.6). The snow temperature deviation was 5.8 K (RMSE) with the model producing lower temperatures (MBE: –2.7 K). In the CG Arctic Crocus ERA19 run the lowest snow surface temperatures between –50 to –60 ℃ were generated in the same month as they occurred in the measurements between December and April, but as in the CG Standard Crocus ERA19 run, the temperatures were about 10 ℃ lower in range (Fig.30).

The deviation of the modelled and measured soil temperatures was similar to the CG Standard Crocus ERA19 run –2.9 K (RMSE) with a MBE of –1 K. The modelled temperatures showed the same general pattern as the sensor data set with a delayed cooling of the ground during the onset of the season. However, as in the two other runs the curtain structure with temperatures close to 0 ℃ in the upper soil (from 0.1 to 0.4 m) from end-September until November was generated which was not observed in the sensor data set.

Also, the freeze-back (temperatures between –5 to –10 ℃) started about four weeks earlier in mid-November (mid-December in sensor data) and the soil thermal regime needed about twice the time the soil regime needed in the measured data set to cool down to –10 to –15 ℃. The CG Arctic Crocus ERA19 run was in better agreement with the measured data (than the CG Standard Crocus ERA19 run). Temperatures between –15 to –20 ℃ reached the soil regime down to 1 m from January to May in all seasons except 2016/2017. The EOS ALTD was about 0.4 m and the same pattern as in the CG Standard Crocus ERA44 model run occurred, with higher temperatures between 10 to 15 ℃ in the first 0.2 m of the soil.

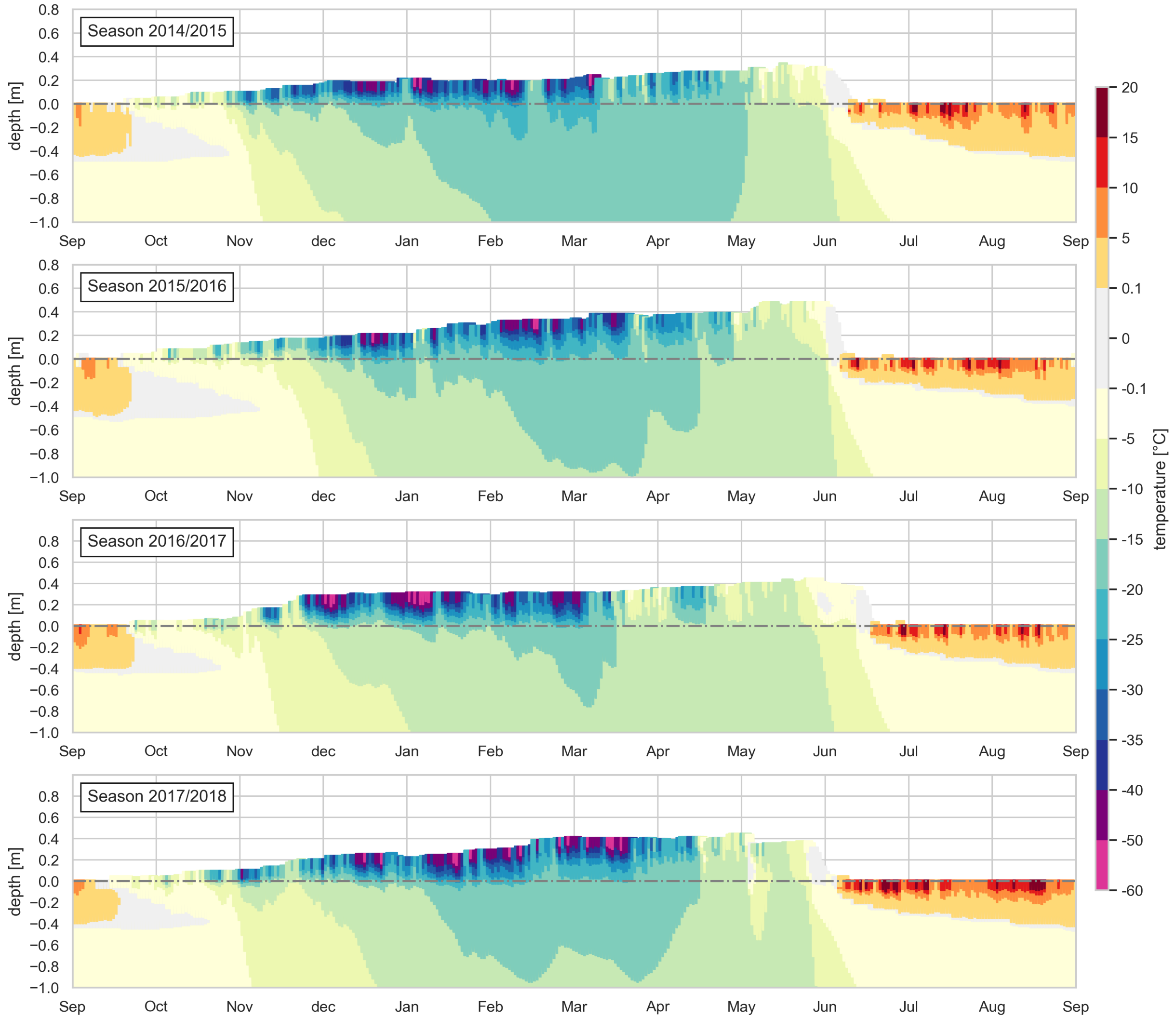

Figure 30: Thermal profile (snow and soil) for the model run CG Arctic Crocus ERA19 for the years 2014 to 2018. The dashed grey line indicates the ground surface. The discrete colourbar was set up with the same steps as in Fig. 14 with the thermal profile from automated measurements.

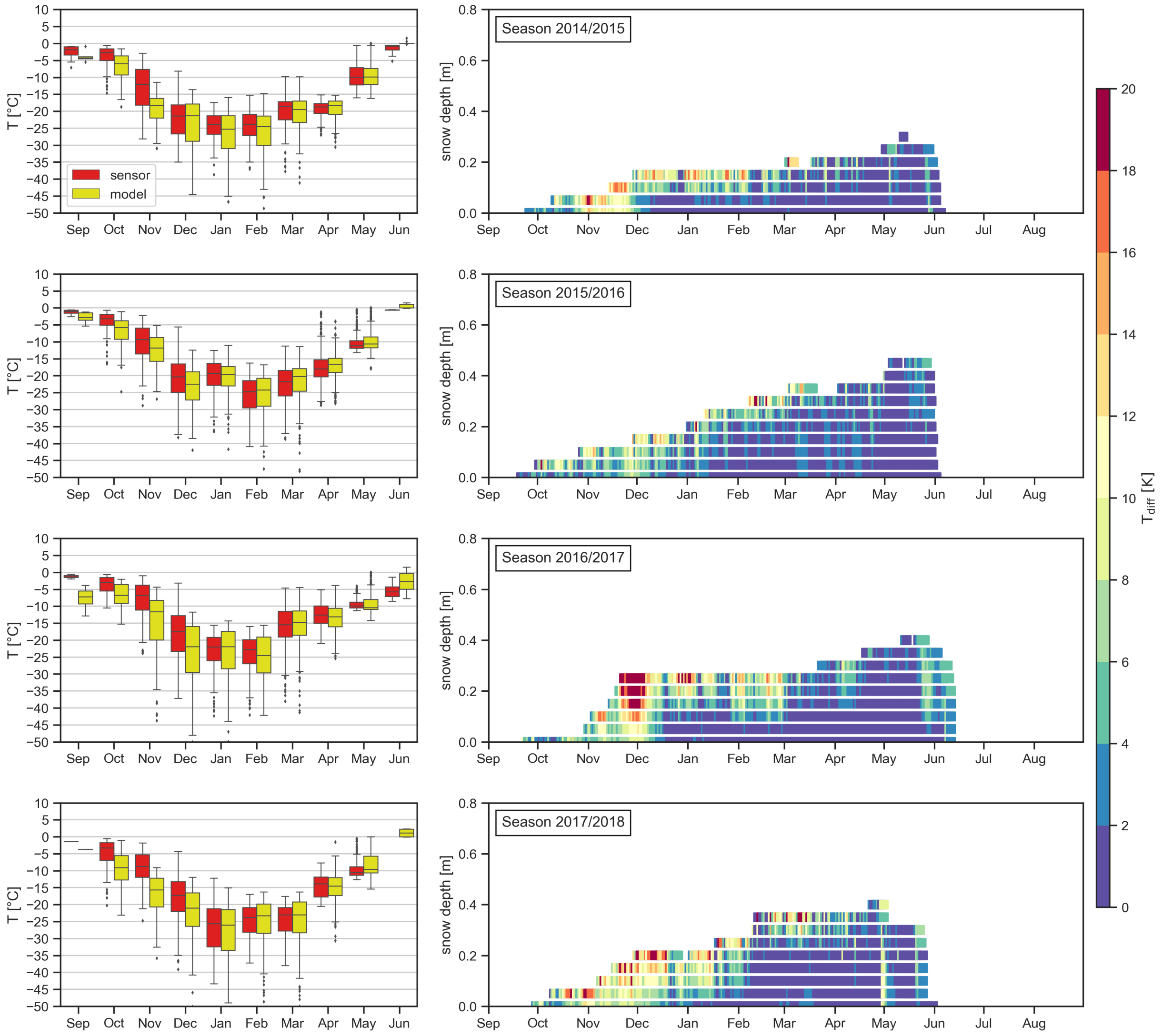

Figure 31: Comparison of temperatures generated by the CG Arctic Crocus ERA19 model run and the automated temperatures measurements for the years 2014 to 2018. The box plot on the left show the median temperature per month for the measured (red) and modelled temperatures (yellow). T_{diff} is the absolute temperature difference between measured and modelled temperatures within the installation heights of the thermocouples (0 to 0.5 m). The white horizontals are the 0.05 m steps between the thermocouple heights.

The largest temperature discrepancies between 16 to 20 ℃ occurred in the upper 0.2 m of the snowpack, mostly during the onset period from October to December. Especially, the 2016/2017 season showed a large deviation in December (Fig. 31). The deviation depth was about 0.1 m larger than in the CG Standard Crocus ERA19 run. Within the majority of the lower snowpack, the temperature deviation was only between 0 to 6 ℃.

The modelled temperatures were lower than the measured temperatures. The density evolution generated with the CG Arctic Crocus ERA19 run showed a deviation of 140 kg m^{-3} (RMSE) compared to the measurements with the SPA-2. The model produced higher densities (MBE: 104 kg m^{-3}, Tab.6). This was the highest deviation within the three model runs. During the onset of the snow season, the snow density fluctuated between 200 and 300 kg m^{-3} in all simulated seasons from mid-September to mid-October (Fig.32). This was up to 50 kg m^{-3} higher than the density evolution in the other model runs during this period. Overall, the modelled snowpack stratigraphy was characterized by basal layers with a higher density and layers with lower density in the

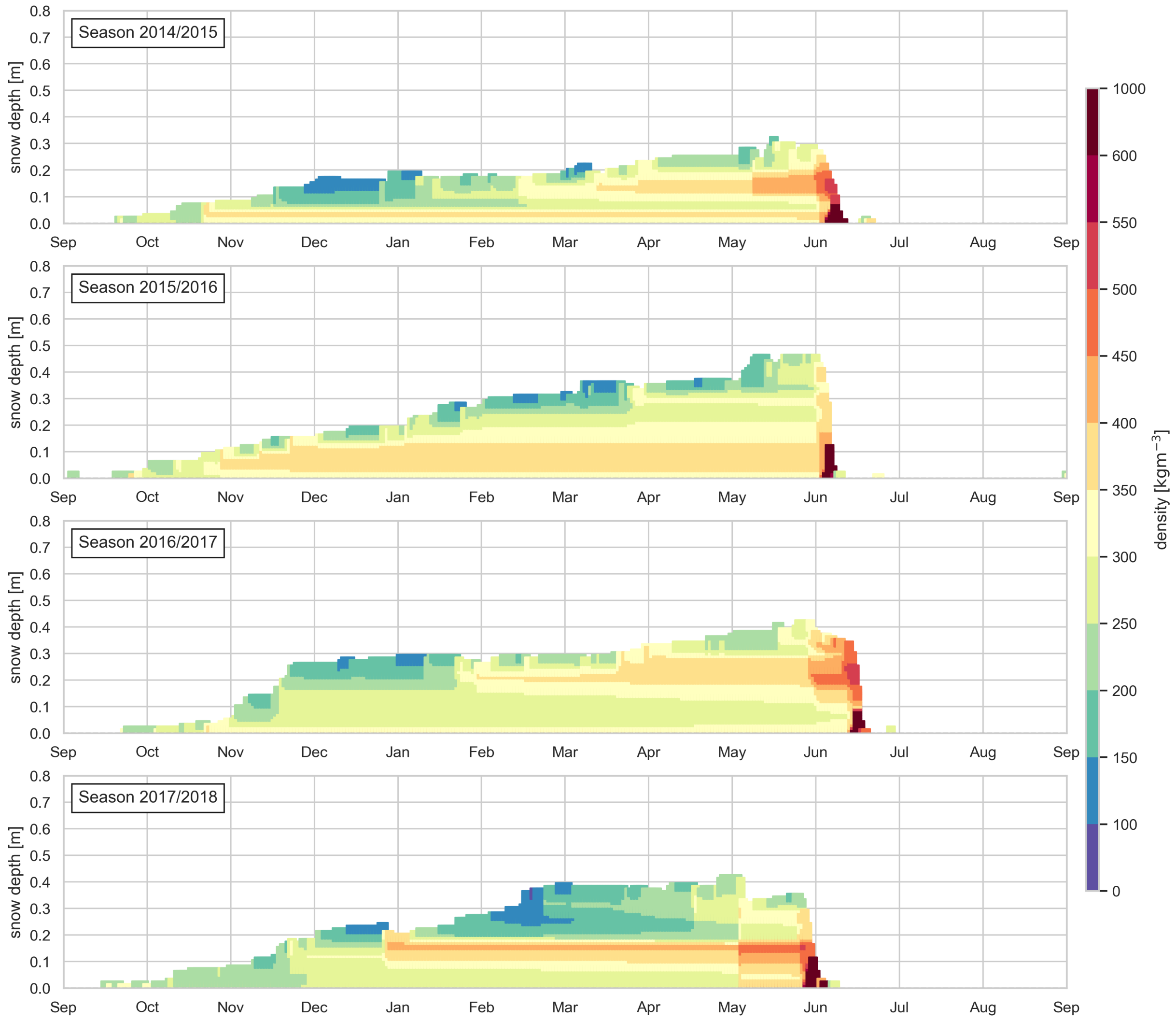

Figure 32: Density profile for the model run CG Arctic Crocus ERA19 for the years 2014 to 2018.

most upper layers, similar to the other model runs. However, there were differences in the density profile of the snowpack in this model run. In the first two modelled seasons, a basal layer with low density between 300 to 350 kg m^{-3} was modelled, which endured through the entire season.

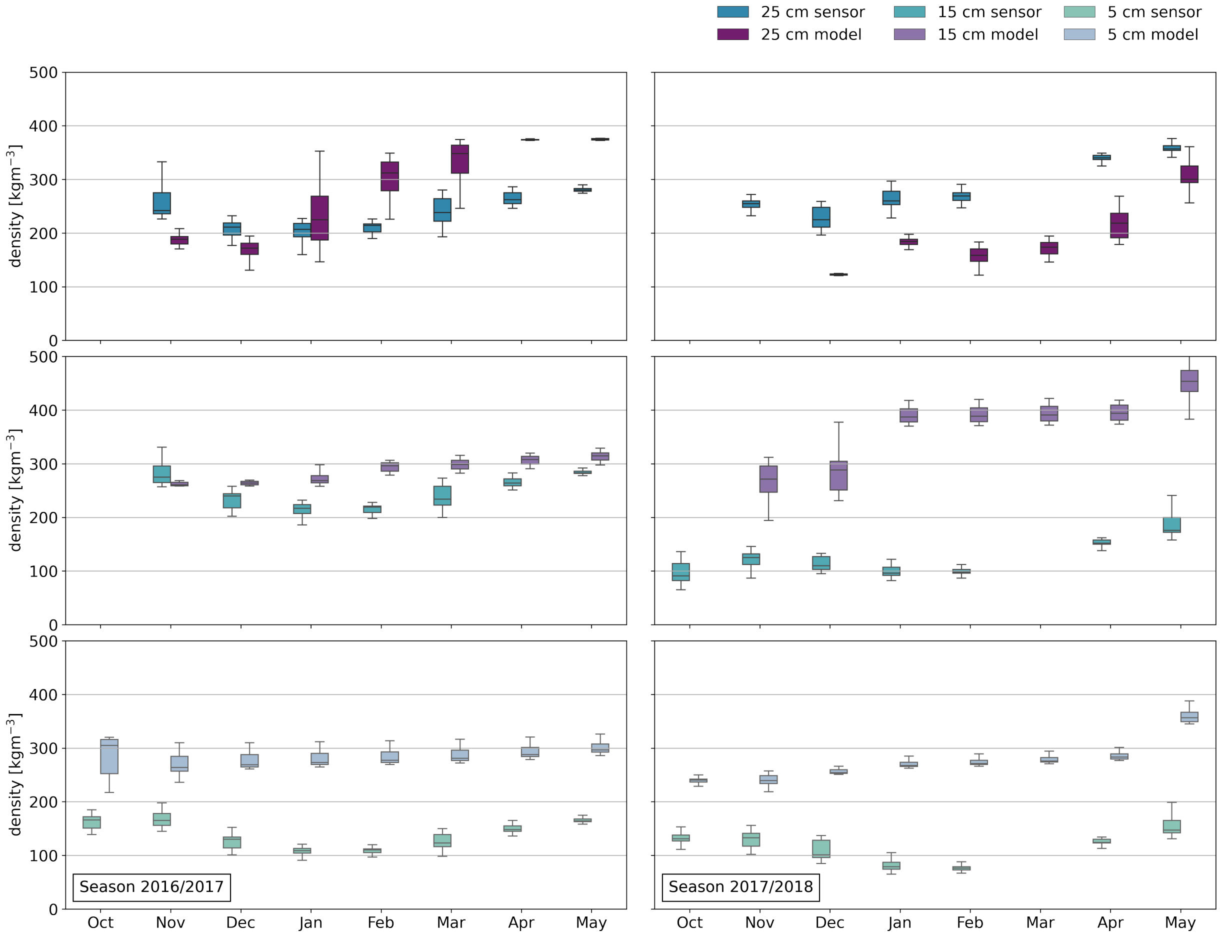

Figure 33: Comparison between the CG Arctic Crocus ERA19 model run and automated density measurements from the SPA-2. The density was compared at 0.05, 0.15 and 0.25 m height. box plot contain the daily averages.

On top, a layer with higher density between 350 to 400 kg m^{-3} developed during the beginning of November. This layer was more massive in 2015/2016 than 2014/2015. In the snow seasons 2016/2017 a basal layer (up to 0.15 m thick) with a density between 250 to 300 kg m^{-3} was modelled and was overlain by alternating layers with higher densities (300 to 400 kg m^{-3}). The upper snowpack in all seasons was characterized by alternating density layers between 100 to 400 kg m^{-3} with the lowest densities appearing on the snow surface like in the other two model runs. The snow column was more heterogeneous than in the other model runs. The snowmelt period in June was characterized by densities above 600 kg m^{-3}.

I compared the modelled and measured (SPA-2) seasonal density variation 0.05, 0.15 and 0.25 m height (Fig.33). In 2016/2017 the modelled densities in 0.25 m height were in the same range as the measured densities except for the onset and melting period. The model reproduce the seasonal evolution in this height. The modelled density in 0.15 m was higher than the measured density during the majority of the time from January to April, with deviation in February up to 50 kg m^{-3}.

In 0.05 m there was a significant deviation between the modelled and measured values. The modelled density was constant about 290 kg m^{-3} whereas the measured density was below 200 kg m^{-3} and showed a decrease up to 50 kg m^{-3} from November to February. In the second year, the modelled data was significantly different for all heights. However, the density profile followed the stratigraphy observed in Arctic snowpacks with a low density basal layer (250 to 290 kg m^{-3}) covered by a layer with higher density (250 to 400 kg m^{-3}).

In summary, the CG Standard Crocus ERA19 model run showed the best agreement with the sensor data set as it had the smallest RMSE among the three runs (Tab.6) for all compared parameters (snow depth, snow and soil temperature, snow density). However, the snowpack was still not reproduced to a satisfying degree. Not only was the snow depth 0.1 m too shallow (Fig.21) but especially the density profile was generated with a stratigraphy inverted to the observations (Fig.25). The snow thermal regime was overall colder than in the measurements. The largest deviations occurred during the onset of the seasons. Throughout the season, the deviations especially occurred in the upper part of the snowpack (Fig.23). Consequently the ground thermal regime also showed major deviations compared to the measured data set (Fig.22). The freeze-back period started too early already in mid-November whereas the measurements showed the beginning of the freeze-back, not to happen before mid-December. Also, the soil temperatures between January to May were higher than in the measurements. Low temperatures between –15 to –20 °C only exceeded a depth below –0.6 m in 2014/2015. In the measurements, this depth was exceeded in all years except the 2016/2017 season. The CG Standard Crocus ERA44 run had the lowest agreement with the measurements as the generated snow depth was the thinnest (0.2 m) and the temperatures were lowest (–4.9 °C). The CG Arctic Crocus ERA19 model run also did not generate a snow depth in range of the measurements as it was too shallow (0.1 m). The temperature agreement was similar to the CG Standard Crocus ERA19 run with slightly better calculations for the soil thermal regime, as the area with low soil temperatures between −15 to −20 ℃ exceeded a depth of 0.6 m in all years except in the 2016/2017 season. The density evolution was only generated partially correct in the 2016/2017 season, when basal low density layers were overlain with high density layers in 0.05 and 0.15 metre height but the densities were at least twice as high as values detected by the SPA-2 sensors (Fig.33). The model results revealed the following key points:

- The modelled snow depth was too shallow in all three model runs, but a better agreement was achieved with the ERA19 forcing.
- The model runs generated the low snow surface temperatures between −60 and −50 ℃ whereas the observation minimum was between −50 and −40 ℃.
- Only in the CG Arctic Crocus model run the Arctic density stratigraphy with basal low density layers overlain by high density layers was partially reproduced for the 2016/2017 but densities were twice the measured values.
- The calculations of the soil temperatures were in good agreement with the measurements, but the cooling pattern of the ground thermal regime was different with an earlier begin of the freeze-back period.

4 Discussion

4.1 Snow depth

My analyses of the 6-year record (2014 to 2020) of snow depth showed a strong spatial variability within the LCP complex. The snow depth in all years was the deepest in the centre and trough location (EOS 0.39 to 0.63 m) and the shallowest on rims (EOS 0.22 to 0.43 m).

The same micro-topographic snow depth distribution pattern was observed by Boike et al. (2013) who measured the snow depth in 8 different polygons (72 measurements per micro-topographic location) during the field campaign in April 2008. They found the deepest mean snow depth in centres (0.46 m) and the shallowest on polygon rims (0.17 m). In comparison with their data set, my results suggest an increase in the EOS snow depth at least by a factor of two. My findings partially agree with the investigations done by Gouttevin et al. (2018) who found the deepest snow depth on slopes (0.27 m) during the field campaign in 2013. As stated by Gouttevin et al. (2018) the shallow snow depth on rims and the deep snow cover on slopes is explained by wind processes blowing away snow from rims and accumulating the snow on the lee site of slopes as described by Wainwright et al. (2017). Although, this description is accurate for a snow depth which does not exceed the rim height, the results in my thesis lead to the assumption, that once the snow depth exceeds the height of the micro-topographical relief it is the deepest in the centre of the polygon. Nevertheless, the results of my thesis strongly underline the role of the micro-topographical classes in the polygonal tundra as drivers for the spatial variability of snow physical properties, as highlighted by Gouttevin et al. (2018).

The maximum centre snow depth obtained in my thesis was 0.74 m in the snow season 2017/2018. This is 0.2 m higher than the maximum centre snow depth in the 9-year record published by Boike et al. (2013) who measured a maximum centre snow depth of 0.56 m in the snow season 2003/2004. It agrees well with the 16-year record published by Boike et al. (2019) who observed a maximum snow depth of 0.7 m in the snow season 2016/2017.

In fact, the snow depth record presented in my thesis can be treated as an extension of the 16-year record (Boike et al., 2019) and suggests an increase in snow depth from 2014 with a climax in the 2017/2018 snow season, followed by another decrease in snow depth until 2019/2020. The data reveals the high annual variability of the snow depth (Fig.13). Additionally, the accumulation pattern of the snow cover in the setup period from October to November showed a yearly variability. In three seasons 2014/2015, 2015/2016 and 2017/2018 the snow accumulation was rapid and reached a snow depth of about 0.2 m by mid-October. On the contrary, in 2016/2017 snow accumulated slower and reached 0.2 m not before beginning-November. This shows that huge variations occurred in the setup period. This period is crucial as this is the time when the initial snowpack stratigraphy is determined i.e. the depth hoar formation. My analyses of the snow depth data revealed the following key findings:

- There was a general increase in snow depth within the analysed years compared to the past (2002 to 2011).
- The snow depth showed an inter-annual variability.
- The snow accumulation pattern during setup period also showed an inter-annual variability.
- The spatial variability of the snowpack on Samoylov Island is strongly influenced by the micro-topography of the polygon complex.

4.2 Thermal profile

As for the snow depth, my analyses of the snow and soil temperatures from 2014 to 2018 showed inter-annual variations in the temperature range and depths into the snow and soil regime. In 2014/2015, 2015/2016 and 2017/2018 low temperatures (between −15 to −20 ℃) reached the soil regime down to 0.1 m. The season 2014/2015 with the shallowest maximum snow depth of 0.51 m not only had the longest period of deep low soil temperatures but it also was the only year when soil temperatures reached −20 to −25 ℃ (Fig.14). As the air temperature was not significantly lower (Tab.9) than in the other years, it is reasonable to assume that the shallower total snow depth led to a lower insulating power of the snow and with that a better transmission of low air temperatures into the soil regime. This agrees with research conducted by Sokratov and Barry (2002) who showed the relationship between snow depth and the thermo-insulation effect on the soil-surface energy balance from October to April (stage II to III).

My assumption is also supported by the higher temperatures in the deeper soil layers in the season 2016/2017. Here, with a maximum snow depth of 0.71 m only the soil up to

0.8 m had low temperatures (between −15 to −20 ℃) and the soil below 0.8 m did not experience the cooling (but did in the other seasons). Furthermore, the period of these low soil temperatures was also the shortest, only lasting for two months from January to March. Interestingly, the season 2017/2018 with a similar maximum snow depth of 0.74 m did not show this pattern. Both seasons experienced an air temperature cold spell in January (temperatures in the upper snowpack between −35 to −50 ℃) but the low temperatures in 2017/2018 were able to reached the soil down to 1 m.

The difference between those two seasons seems to be connected to the different initial snow accumulation pattern during the setup period of the two season rather than the snow depth. In 2016/2017 the snow accumulation slowly started to increase over a period of two months whereas in 2017/2018 (and also all other years) snow accumulated more abruptly. Hence, the thermal data set revealed the effects of the snow depth variability and outlines the importance of the setup period:

- The snow depth is a driver of the snowpacks' insulation power.
- A thin snow cover (0.51 m) led to a deeper penetration depth and duration of low temperatures (−15 to −20 ℃) and hence, had a lower insulation power.
- Given the same snow depth the initial snow conditions and with that the internal snowpack structure influences the insulation power.

4.3 Snow density

Following the thought, that snow depth influences the insulation power the question arises why the snow seasons 2016/2017 and 2017/2018 showed a different insulating behaviour. As mentioned previously, both seasons had a snow depth exceeding 0.7 m with only minor deviation in the snow depth evolution. A major difference was found in the accumulation pattern during the setup period. It is, therefore, necessary to look into the snow micro-structure, especially the density evolution to further understand the snowpacks' influence on the ground thermal regime and the internal processes which occurred during the setup period. As with the snow depth and snow/soil temperatures, the snow density and SWE respectively also showed annual variability. For the period of four years (2016 to 2020) the median EOS bulk density calculated from the SPA-2 strap sensors in the polygon centre was between 204 $\mathrm{kg\,m^{-3}}$ (2019/2020) to 236 $\mathrm{kg\,m^{-3}}$ (2016/2017).

Furthermore, the comparison (Fig.17 2016/2017) of the upper SPA-2 measurements with the density calculated from the TDR probe in 0.2 m height at the nearby soil station showed a good agreement from December to March in the 2016/2017 season. The deviation from March to June of about 100 kg m^{-3} was probably due to the spatial variability of the snow cover as the two data sets were not obtained in the same LCP complex. The SPA-2 density measurements agree well with the manual density measurements done by Boike et al. (2013) who measured 225 kg m^{-3} as the average for the centre locations (in range of 150 to 320 kg m^{-3}) during the 2008 spring measurement campaign.

My results are also in good agreement with the study done by Gouttevin et al. (2018) who measured a density of 236 kg m^{-3} for the basal depth hoar layer during their campaign in 2013. Even by taking into account the error of the density cutter, which can lead to an overestimation of up to 6 % for snow with a density below 296 kg m^{-3} (Proksch et al., 2016), the agreement between the automated measurements and the field observations was good. However, it seems to be questionable that the SPA-2 measurements indeed represent the bulk density of the snowpack in the background of the earlier emphasized disagreement in snow depth with the two studies. Also the fact, that Gouttevin et al. (2018) measured higher densities for wind slabs in the upper snowpack requires a detailed look at the density measurements in my study. The here processed density measurements actually were not a bulk parameter representative for the entire snowpack, but rather only represented the bulk density of the lower snowpack up to 0.3 m due to the setup of the SPA-2 unit (the same needs to be taken into account for the SWE estimation as it was calculated with the bulk density from the three SPA-2 sensors).

4.3.1 Performance Snow Pack Analysing System (SPA-2)

The SPA-2 setup at the snow station only measured density in three heights up to 0.25 m. Taking into account the signal penetration depth of each strap sensor which was about 0.04 m it can be assumed, the SPA-2 measurements are not representative for the snowpack above 0.3 m. However, the snow depth exceeded this height in all analysed years. According to (Gouttevin et al., 2018) the density of the upper snowpack is about 356 kg m^{-3} as it consists out of hard wind slabs. Also the here processed field data from the field campaign in 2018 revealed an average density of 297 kg m^{-3}, but maximum densities up to 500 kg m^{-3} were obtained. Certainly, this data set had an enormous spatial variability (Tab.7 and Tab.8) which in great part is able to explain the disagreement with the SPA-2 data. The SPA-2 measured only once in May 2018

(Fig.17) densities up to 350 kg m^{-3} in 0.25 m height. There were no density measurements exceeding 350 kg m^{-3} although the field data (Tab.7 and Tab.8) show that high densities (above 350 kg m^{-3}) occurred frequently in the snowpack on Samoylov. High densities i.e. of wind slab layers were not measured by the SPA-2 unit due to the limited measurement height of 0.3 m. In my point of view there are two solutions for this measurement gap. To obtain the bulk density, it is either necessary to adjust the current installation height of the SPA-2 straps to i.e. 0.1, 0.25 and 0.45 m height or to mount one of the SPA-2 straps with an angle (e.g. 45°) as done by Staehli et al. (2004).

When discussing the setup of the SPA-2 unit, it is necessary to elaborate two features leading to an underestimation of the density measurements that were found in this thesis. The formation of air gaps around the SPA-2 straps is a known problem. Air gaps along the SPA-2 straps can falsify the electronic signal but also can act as preferential melt water pathways (Proksch et al., 2016). In the snowpack on Samoylov Island, the latter issue is negligible as liquid water is prominent only during the melting season and no rain events occur during the winter period (so far). The SPA-2 strap in 0.05 m height is strongly embedded by the vegetation (Fig.9) which can lead to a disturbed snow settling (formation of air gaps) and also can support depth hoar formation around the straps similar as observed in shrub-rich tundra (Domine et al., 2016a). Vegetation protects the snow from wind speeds during the onset of the snow season, and it also increases the amount of soil moisture and with that delaying the freezing (Royer et al., 2021a) which provides more water for depth hoar formation. Those effects are most notable with shrubs (Domine et al., 2016b) but I here suggest, that the partly overgrown SPA-2 strap might experience similar effects. The lower SPA-2 strap most likely underestimated the snow density due to the air gap formation and consequently a falsified electronic signal. The mathematical air gap correction described by Huebner (1999) is implemented in the SPA-2 software, but it is not possible to comprehend nor to adapt the calculations in detail (Sommer Messtechnik, 2016).

Furthermore, in Fig.10 the only winter validation attempt is shown which was done with the SPA-2 system in 2012. The cross-section shows the SPA-2 sensors in 0.05 and 0.15 m height and around both straps a different snow grain shape (probably hoar crystals) can be observed. This hoar formation because of the SPA-2 strap - vegetation environment was probably artificial. It would not have occurred up to this magnitude in a grass-centre polygon without the SPA-2 unit i.e. the depth hoar layer in Fig.6 (b) did not show spots like the ones around the 0.15 m SPA-2 strap sensor in Fig.10 (b).

Those areas around the straps look similar to the basal depth hoar chains (high stage of metamorphism) which are unlikely to occur in upper parts of the snow. The patches did not have a great lateral extent (Fig.10 (b)) and hence, evolved artificially due to strap-snow-interaction. This artificial depth hoar formation implied a falsified electronic signal and most likely also contributed to an underestimation in density. Nevertheless, as to my knowledge, the measurements from the SPA-2 unit are the only continuous data series of snow density for the Siberian snowpack which makes them highly valuable. In summary, my results lead to the following key points:

- The performance of the SPA-2 density straps was overall satisfying and produced reasonable data sets.
- It is very important to relate the density measurements with the snow depth to estimate how much of the total snowpack density was captured by the SPA-2 straps.
- The vegetation embedding of the lowest strap (0.05 m) benefits air gap and artificial depth hoar formation which probably lead to an underestimation of the density measurements (and SWE respectively).
- Artificial depth hoar formation is most likely to occur at least on the lower two SPA-2 straps and leads to an underestimation of the density to an unknown extent.

4.3.2 Snow - soil interactions

The analyses of the density data in context of the SPA-2 system performance revealed that the lower snowpack on Samoylov Island, up to a snow depth of about 0.3 m is dominated by snow with a density lower than 350 kg m^{-3}. My detailed seasonal analyses for 2016/2017 and 2017/2018 showed, that within the 0.3 m, a stratigraphy occurs dividing the snowpack in basal snow with a density between 100 to 200 kg m^{-3} and snow with a density between 200 to 350 kg m^{-3} (Fig.17). Considering the elaborated sources of density underestimation of the SPA-2 unit I assume the basal snow layer to be depth hoar. The density range is in good agreement with the study conducted by Benson and Sturm (1993) who found depth hoar densities between 150 to 250 kg m^{-3}.

The formation of depth hoar is (among other parameters) connected to the soil moisture content (Davesne et al., 2021; Domine et al., 2018; Woo, 1982). After the snow settled on the ground, the high temperature gradient between the cold air and the warmer ground induced a vertical water vapour flux. This initiated snow metamorphism and the grains started to transform from a rounded grain shape into facets with very poor bonding. The soil-snow vapour flux as well as layer-to-layer vapour fluxes were observed by Sturm and Benson (1997) for their study site in Fairbanks, Alaska. Their detailed analyses showed peak values in the vapour flux, especially in the early season when the snow cover was thin and the temperature gradient high. They also observed grain growth (transformation into depth hoar) in the basal layers throughout the entire season. My analyses of the soil VWC and density evolution in 2016/2017 demonstrated concomitant process for Samoylov Island. The soil VWC began to decrease with beginning-November and with beginning-December als, the basal density started to decrease (SPA-2 strap in 0.05 m Fig.19). The decrease in density stagnated with the complete freeze back of the soil throughout February. The increase in density in March after the soil freeze-back was probably a combination of compaction (snow depth increase throughout the season) maybe snow accumulation (lack of data) and could demonstrate the thermal-controlled end of grain growth, suggested by (Sturm and Benson, 1997).

Within my two-year-record for the detailed analyses of density, the depth hoar layer showed a huge variability in its extent which has been observed in the past. The depth hoar fraction can be up to 80 % (Sturm and Johnson, 1991). Between the two analysed years, there is a difference in the extent of the depth hoar layer by a magnitude of three (2016/2017 up to 0.05 m and 2017/2018 up to 0.15 m). This deviation in depth hoar formation is probably connected with the different initial snow depth conditions during the October-November period. The snow depth determines how much snow is available to undergo the depth hoar formation. In 2016/2017 with the gradual increase in snow depth during October, only half the amount of snow accumulated compared to the 2017/2018 season in the same time period. The depth hoar extent of each year was about the size of the respective initial snow depth. This leads to the assumption, that within the two seasons the snow accumulation pattern between October to November determined the amount of depth hoar. The difference in depth hoar extent led to a different insulation power of the snowpack.

Depth hoar has a low thermal conductivity compared to the upper layers in the snow (Gouttevin et al., 2018). Hence, the depth hoar fraction in the snowpack influences the ground thermal regime, potentially leading to an increase in ground surface temperatures (Zhang et al., 1996). The here analysed data suggests otherwise though. In 2017/2018 a higher depth hoar fraction (compared to 2016/2017) was associated with deeper low temperature penetration depth and a longer duration of the penetration within the soil regime. I speculate that the anisotropy of depth hoar could be identified as the reason for this counter-intuitive thermal insulation behaviour. Research about the relationship between snow density and the thermal conductivity of snow by Riche and Schneebeli (2013); Calonne et al. (2011) showed that the latter is connected to the anisotropy of the snow sample. In their study, Calonne et al. (2011) computed the full tensor of the effective thermal conductivity and found the vertical component of i.e. depth hoar samples to be up to 1.5 times larger than the horizontal component. Furthermore, Riche and Schneebeli (2013) pointed out the importance of considering the anisotropy of snow when measuring the thermal conductivity. They outlined the importance of the anisotropic character of the thermal conductivity of snow for the heat flow and energy-balance of the snowpack. This could be the clue to explain the thermal insulation behaviour of the snowpack on Samoylov. I suspect, that the higher initial snow depth in the 2017/2018 season supplied snow which underwent depth hoar formation and grain growth to an extent where the crystals got highly anisotropic, more than in 2016/2017. Eventually, the lower snowpack was highly permeable, providing better conduction paths for low temperatures. A similar effect is observed underneath rock-glaciers, where the active layer composition includes coarse blocks with airspace which allow better (vertical) air convection (Wicky and Hauck, 2020). In summary, the two-year-record density evolution on Samoylov Island highlights the following points:

- The effectiveness of depth hoar formation is connected to the snow accumulation pattern (snow depth) during the setup period of the snow season (October to December). In my thesis, the basal depth hoar layer thickness of 0.05 m and 0.15 m was formed by a gradual and abrupt snow depth increase, respectively.

- It is also connected to the soil VWC in the active layer during the freeze-back (October to December) until the complete freeze-up in February/March.

- The depth hoar fraction has an influence on the insulation power of the snowpack and determines (among other parameters) how deep low reach into the soil. Here, in presence of a 0.05 m thick depth hoar layer, in the soil regime below 0.8 m temperatures between –15 to –20 °C were not obtained, whereas in presence of a 0.15 m thick depth hoar layer, in the soil regime below 0.8 m temperatures between –15 to –20 °C were obtained.

- Contrary to the general knowledge about the insulation properties of Arctic depth hoar, my results suggest that given the same snow depth a bigger depth hoar fraction can lead to a smaller insulation power as shown for the season 2017/2018.

4.4 Model output

To evaluate the ‹CG Community› models' ability to generate snow physical properties and the influence on the ground thermal regime, I compared the results of the three model runs with the automated measurements.

4.4.1 Forcing sensitivity

The model results generated near surface snow temperatures which were frequently 10 ℃ lower than the measured temperatures. The observed snow temperatures were only measured up to a height of 0.5 m which means for a snow depth exceeding this height no temperatures were included in the data set which were potentially colder. Furthermore, the deviation is connected to the forcing data as the air temperatures were colder than the measured air temperatures (MBE: up to –1.6 ℃, A.3, Fig.34 and Fig.34). In a follow-up analyses I found a sensitivity of the model to the forcing data set which had the greatest influence on the snow depth calculations. The snowfall rate in the ERA19 was higher than in the ERA44 (A.3Fig.34) which conversely led to the underestimation of snow depth in the CG Standard Crocus ERA44 model run. The same ERA44 forcing data was also used by Westermann et al. (2016) who did not report an underestimation in snow depth. However, they configured the CG 3 model code with a restricted snow depth of 0.45 m. This was based on the measurements done by (Boike et al., 2013) where the snow depth rarely exceeded 0.45 m height due to wind redistribution. This outlines the importance of site-specific forcing data. Furthermore, it emphasizes a need to compare forcing data with recent (automated) snow measurements. Outdated forcing may not contain recent events, e.g. the snow depth increase of about 0.3 m for the winter seasons of 2016/2017 and 2017/2018 analysed in this work.

4.4.2 Modelled snow physical properties

The CG Arctic Crocus ERA19 model run also generated snow depths that were too shallow, 0.1 m less than in the automated measurements (Tab.6). This was not connected to the forcing file as the same ERA19 forcing data was used for the CG Standard Crocus ERA19 model run, which generated the best fitting snow depths. Consequently, the mismatch must be connected to the snow scheme itself. In the CG Arctic Crocus snow scheme, the maximum wind impacted density was raised to 600 kg m^{-3}, the effect of wind on fresh snow density was doubled and the effect of wind on the snowpack density was tripled compared to the parameterization of the original (Standard) Crocus publication (Royer et al., 2021b). This was done to better represent Arctic conditions where wind compaction plays an important role (Gouttevin et al., 2018). Hence, the wind compaction process is not only faster but also stronger in effect, which leads to an over-compaction effect within the snowpack. The snow has no time to change and to stabilize, even with a low density. Furthermore, new snow initially has a higher density, leading to an overestimation of the densification for the snowpack and thus to an insufficient snow depth compared to the automated snow depth measurements presented in this work. In this thesis, the Standard Crocus snow scheme led to snow depths results in better agreement with the automated measurements (Tab.6). This is not in agreement with the results by Royer et al. (2021b) who were able to decrease the RMSE in snow depth with the Arctic Crocus version compared to the Standard Crocus. However, they analyses were focused on long-term simulations (1979 to 2018).

The impact of the snow cover on the ground thermal regime is not only determined by the snow depth but also by the internal structure of the snowpack as revealed in this work and discussed above. In the Crocus snow scheme of the ‹CG Community› model the thermal conductivity is directly related to the density as it is calculated using the equations by Yen (1981) (Eqn.(4) in Standard Crocus) or Sturm et al. (1997) (Eqn.(5) in Arctic Crocus). In my thesis neither the Standard nor the Arctic Crocus version were able to generate the density profile as obtained with the SPA-2 unit to a satisfying degree. Especially, the basal depth hoar layer was not generated. With the CG Standard Crocus ERA19 run in all seasons the modeled lower snowpack had higher density values than densities in the upper snowpack (Fig.24). This inverted stratigraphy was already emphasized by Domine et al. (2019) who came across the same issue of a reversed snow density profile using the Crocus model compared to field measurements. They specifically pinpointed at the missing implementation of the upward water vapour mass transfer. In the Crocus snow scheme, the depth hoar growth is predicted through empirical functions based on cold room simulations and the layer evolution is connected to the snow density, temperature, liquid water content and grain type (Vionnet et al., 2012). Also, the CG Arctic Crocus ERA19 did not generate the density profile which was measured with the SPA-2 unit. Although, this model run was able to generate the general stratigraphy in 2017/2018 the densities in the lower snowpack (0.15 m) were significantly higher than measured and in the upper snowpack (0.25 m) significantly lower than measured. Efforts were made to improve the depth hoar simulation in the Arctic Crocus version by Royer et al. (2021b) who introduced the vegetation height parameter. In the Arctic Crocus version below this vegetation height wind compaction is decreased, and snow viscosity is increased. This simulates a basal depth hoar layer without implementing the depth hoar formation due to water vapour mass transfer. The vegetation height parameter is not yet included in the Arctic Crocus snow scheme implemented in the ‹CG Community› model.

4.4.3 Influence on the ground thermal regime

The inverted density profile impacts the ground thermal regime because in either of the snow schemes (Arctic or Standard Crocus) which are implemented in the ‹CG Community› model the density is the crucial parameter for the heat flow calculations within the snowpack (Westermann et al., 2022). Admittedly, soil temperatures were in better agreement with the automated measurements in the CG Arctic Crocus model ERA19 run (Fig.30) than in the CG Standard Crocus ERA19 model run (Fig.22) but given the underestimation in snow depth that occurred in the CG Arctic Crocus ERA19 run due to the overestimation of wind compaction effects still further studies with different parameter adjustment need to be done. It is necessary to conduct more sensitivity analyses, e.g. with lower wind compaction effects for the Samoylov site. In contrast to the limited performance for the snow domain, the soil domain calculations during the summer month were in overall good agreement with the automated measurements. I was able to model realistic ALTD and soil temperatures by using a constant θ_{fc} of 0.5 as done by Nitzbon et al. (2019). Different from the sensitivity studies done by Nitzbon et al. (2020) a reduced θ_{fc} of 0.4 resulted in an underestimation of the on simulated ALTD depth (Fig.20). In general, the higher θ_{fc} reproduces a higher thaw depth, as it increases the thermal conductivity. This offsets the additional heat that is required to thaw more ice. The model sensitivity to θ_{fc} suggests that it can be used as a tuning parameter rather than a parameter derived from field conditions for the here conducted model runs. In general, the use of θ_{fc} as a tuning parameter can lead to unrealistic water balance, but this issue was neglected here, as I did not model lateral processes. Other considered tuning factors which interact with θ_{fc} are the evaporation depth and a parameter termed root depth. Both adjust the extraction of soil water content due to evaporation and transpiration and an adjustment is worth considering. The soil stratigraphy in particular is another factor affecting the thaw depth as the composition (mineral, organic and ice content) determines the hydrological regime of the soil, which is especially important in the upper soil layers. In summary, I emphasize the following points:

- In terms of the snow cover evolution, it is necessary to examine the forcing data; especially the wind speed and snowfall rates should be in range of site observations (if validation facilities exists).
- Snow schemes implemented in the ‹CG Community› model failed to reproduce the snow-soil interactions observed from field measurements in this work, especially the depth hoar formation.
- I was not able to generate the basal depth hoar densities in range of the automated measurements from 2014 to 2018 with the parameterizations used in this work as the depth hoar formation.
- Depth hoar formation is not based on the underlying physical process but rather preserved phenomenologically, i.e. the compressibility of the snow decreases when there are large temperature gradients and thus lower densities are generated. This is just a simulation and the actual density loss as observed in my analyses, can not be realized with the current snow scheme.
- To still improve the model abilities, I recommend implementing the vegetation height parameter in the Arctic Crocus snow scheme of the ‹CG Community› model to at least improve the simulation of a basal depth hoar layer formation.

4.5 Outlook

My thesis points out several topics that require further investigations. For one thing more validation measurements are necessary to better understand the depth hoar formation during the early snow season on Samoylov Island. It is not only important to capture the end-of-season snow physical properties but to actually observe and understand the snow cover build-up in the early snow season between October and December. Even though, logistics are difficult, especially in the Russian Arctic at the time of writing, it would be beneficial to perform an additional validation of the SPA-2 unit during these months. Obtaining the grade of artificial depth hoar formation and air gap occurrence around the SPA-2 straps would help to better estimate the measurement accuracy. This would provide an enhanced credibility of the measurements. Also the snow-soil interactions require further research, especially during the onset of the snow season, when the soil freeze-back is concomitanted by depth hoar formation as shown in this work. An approach could be to perform isotope analyses of the soil water and snow during the season onset to determine the origin of the water-mass.

The soil temperature data set revealed a high inter-annual variability which was likely connected to the depth hoar layer thickness. Current snow schemes as the Crocus model have no proper implementation of the depth hoar formation process and hence, have difficulties to reproduce the snowpack evolution. Either it is possible to better adjust the implemented parameterizations which would lead to a site-specific tailoring of the model, or it is necessary to invest resources to generate a new snow-soil model which includes upward water vapour fluxes and depth hoar density decrease. Another approach would be to examine the potential of using a bulk annual ‹effective snow depth›, as proposed by Slater et al. (2017), but I would strongly recommend that such a scheme be compared with snow-soil data sets such as presented in this work.

5 Conclusion

Snow on the ground is a complex variable and its properties and evolution show a high inter-annual and seasonal variability. The snow cover evolution is driven by various parameters such as air temperature, wind speed, soil moisture and the soil thermal regime. Vice versa, snow impacts the soil thermal regime, depending on its internal composition it acts as an insulator, shielding the ground from low winter temperatures. This thesis aimed to document this complexity and variability of the snow cover for Samoylov Island. My time series analysis revealed how the snow cover varies within just a couple of years and points out the importance to set up automated measurement facilities to monitor the Arctic snow cover. My results emphasize the need for future field campaigns during the snow season onset to better understand snow metamorphism processes e.g. the depth hoar formation which greatly can influences the heat flux in the snowpack throughout the entire season. Furthermore, this work highlights the need to not only expand the knowledge that was gathered in past studies but also to reevaluate measured properties to see if they are still valid for recent conditions. Especially the inter-annual variation of the depth hoar layer thickness and the here emphasized enhanced ground cooling in presence of a thick depth hoar layer definitely needs further investigations. Not much is known about the anisotropy-effects on thermal conductivity of depth hoar as this snow type is very delicate to quantify and measure.

I also emphasize how challenging it is to model this high magnitude of complexity with current snow and permafrost models. I was able to produce major snow physical properties and their influence on the soil thermal regime on Samoylov Island with the current ‹CG Community › permafrost model but failed to simulate the correct micro-structural realization of the snowpack. My work underlines the importance of snow as a driving parameter for the ground thermal regime which can not be neglected. The current approach of parameter adjustment is suitable for a wide scope, but this approach has its limits, especially when it comes to modelling the Arctic snowcover. Those limitations and connected uncertainties have to be considered in future modelling attempts as micro-scale limitations lead to limitations on a circum-Arctic scale. I think it is important to implement the correct underlying physical processes such as upward water vapour flux for the depth hoar formation in current snow schemes or to program a new snow scheme which also could include the possibility of being trained with automated data sets such as presented in this thesis.

References

Are, F. and Reimnitz, E. (2000). An Overview of the Lena River Delta Setting: Geology, Tectonics, Geomorphology, and Hydrology. Journal of Coastal Research, 16(4):1083–1093.

Barrere, M., Domine, F., Decharme, B., Morin, S., Vionnet, V., and Lafaysse, M. (2017). Evaluating the performance of coupled snow-soil models in SURFEXv8 to simulate the permafrost thermal regime at a high Arctic site. Geoscientific Model Development, 10(9):3461–3479.

Bartelt, P. and Lehning, M. (2002). A physical SNOWPACK model for the Swiss avalanche warning Part I: Numerical model. Cold Regions Science and Technology, 35(3):123–145.

Benson, C. S. and Sturm, M. (1993). Structure and wind transport of seasonal snow on the Arctic slope of Alaska. Annals of Glaciology, 18:261–267.

Biskaborn, B. K., Smith, S. L., Noetzli, J., Matthes, H., Vieira, G., Streletskiy, D. A., Schoeneich, P., Romanovsky, V. E., Lewkowicz, A. G., Abramov, A., Allard, M., Boike, J., Cable, W. L., Christiansen, H. H., Delaloye, R., Diekmann, B., Drozdov, D., Etzelmüller, B., Grosse, G., Guglielmin, M., Ingeman-Nielsen, T., Isaksen, K., Ishikawa, M., Johansson, M., Johannsson, H., Joo, A., Kaverin, D., Kholodov, A., Konstantinov, P., Kröger, T., Lambiel, C., Lanckman, J. P., Luo, D., Malkova, G., Meiklejohn, I., Moskalenko, N., Oliva, M., Phillips, M., Ramos, M., Sannel, A. B. K., Sergeev, D., Seybold, C., Skryabin, P., Vasiliev, A., Wu, Q., Yoshikawa, K., Zheleznyak, M., and Lantuit, H. (2019). Permafrost is warming at a global scale. Nature Communications, 10(1).

Boike, J., Chadburn, S., Martin, J., Zwieback, S., Althuizen, I. H., Anselm, N., Cai, L., Coulombe, S., Lee, H., Liljedahl, A. K., Schneebeli, M., Sjöberg, Y., Smith, N., Smith, S. L., Streletskiy, D. A., Stuenzi, S. M., Westermann, S., and Wilcox, E. J. (2021). Standardized monitoring of permafrost thaw: a user-friendly, multiparameter protocol. Arctic Science, 8(1):153–182.

Boike, J., Grau, T., Heim, B., Günther, F., Langer, M., Muster, S., Gouttevin, I., and Lange, S. (2016). Satellite-derived changes in the permafrost landscape of central Yakutia, 2000-2011: Wetting, drying, and fires. Global and Planetary Change, 139:116–127.

Boike, J., Juszak, I., Lange, S., Chadburn, S., Burke, E., Paul Overduin, P., Roth, K., Ippisch, O., Bornemann, N., Stern, L., Gouttevin, I., Hauber, E., and Westermann, S. (2018). A 20-year record (1998-2017) of permafrost, active layer and meteorological conditions at a high Arctic permafrost research site (Bayelva, Spitsbergen). Earth System Science Data, 10(1):355–390.

Boike, J., Kattenstroth, B., Abramova, K., Bornemann, N., Chetverova, A., Fedorova, I., Fröb, K., Grigoriev, M., Grüber, M., Kutzbach, L., Langer, M., Minke, M., Muster, S., Piel, K., Pfeiffer, E. M., Stoof, G., Westermann, S., Wischnewski, K., Wille, C., and Hubberten, H. W. (2013). Baseline characteristics of climate, permafrost and land cover from a new permafrost observatory in the Lena River Delta, Siberia (1998-2011). Biogeosciences, 10(3):2105–2128.

Boike, J., Nitzbon, J., Anders, K., Grigoriev, M., Bolshiyanov, D., Langer, M., Lange, S., Bornemann, N., Morgenstern, A., Schreiber, P., Wille, C., Chadburn, S., Gouttevin, I., Burke, E., and Kutzbach, L. (2019). A 16-year record (2002-2017) of permafrost, active-layer, and meteorological conditions at the Samoylov Island Arctic permafrost research site, Lena River delta, northern Siberia: An opportunity to validate remote-sensing data and land surface, snow, and permafrost models. Earth System Science Data, 11(1):261–299.

Boike, J., Roth, K., and Ippisch, O. (2003). Seasonal snow cover on frozen ground: Energy balance calculations of a permafrost site near Ny-Ålesund, Spitsbergen. Journal of Geophysical Research: Atmospheres, 108(2):1–11.

Brun, E., David, P., Sudul, M., and Brunot, G. (1992). A numerical model to simulate snow-cover stratigraphy for operational avalanche forecasting. Journal of Glaciology, 38(128):13–22.

Burke, E. J., Ekici, A., Huang, Y., Chadburn, S. E., Huntingford, C., Ciais, P., Friedlingstein, P., Peng, S., and Krinner, G. (2017). Quantifying uncertainties of permafrost carbon-climate feedbacks. Biogeosciences, 14(12):1–42.

Calonne, N., Flin, F., Morin, S., Lesaffre, B., Du Roscoat, S. R., and Geindreau, C.

(2011). Numerical and experimental investigations of the effective thermal conductivity of snow. Geophysical Research Letters, 38(23):L23501.

Clark, M. P., Hendrikx, J., Slater, A. G., Kavetski, D., Anderson, B., Cullen, N. J., Kerr, T., Örn Hreinsson, E., and Woods, R. A. (2011). Representing spatial variability of snow water equivalent in hydrologic and land-surface models: A review. Water Resources Research, 47(7):W07539.

Davesne, G., Domine, F., and Fortier, D. (2021). Effects of meteorology and soil moisture on the spatio-temporal evolution of the depth hoar layer in the polar desert snowpack. Journal of Glaciology, 68(269):457–472.

Domine, F., Barrere, M., and Morin, S. (2016a). The growth of shrubs on high Arctic tundra at Bylot Island: Impact on snow physical properties and permafrost thermal regime. Biogeosciences, 13(23):6471–6486.

Domine, F., Barrere, M., and Sarrazin, D. (2016b). Seasonal evolution of the effective thermal conductivity of the snow and the soil in high Arctic herb tundra at Bylot Island, Canada. The Cryosphere, 10(6):2573–2588.

Domine, F., Belke-Brea, M., Sarrazin, D., Arnaud, L., Barrere, M., and Poirier, M. (2018). Soil moisture, wind speed and depth hoar formation in the Arctic snowpack. Journal of Glaciology, 64(248):990–1002.

Domine, F., Cabanes, A., and Legagneux, L. (2002). Structure, microphysics, and surface area of the Arctic snowpack near Alert during the ALERT 2000 campaign. Atmospheric Environment, 36:2753–2765.

Domine, F., Gallet, J.-C., Bock, J., and Morin, S. (2012). Structure, specific surface area and thermal conductivity of the snowpack around Barrow, Alaska. Journal of Geophysical Research: Atmospheres, 117(D14).

Domine, F., Picard, G., Morin, S., Barrere, M., Madore, J. B., and Langlois, A. (2019). Major Issues in Simulating Some Arctic Snowpack Properties Using Current Detailed Snow Physics Models: Consequences for the Thermal Regime and Water Budget of Permafrost. Journal of Advances in Modeling Earth Systems, 11(1):34–44.

Fierz, C., Armstrong, R., Durand, Y., Etchevers, P., Greene, E., McClung, D., Nishimura, K., Satyawali, P., and Sokratov, S. (2009). The international classification for seasonal snow on the ground. IHP-VII Technical Documents in Hydrology, 83(1):90.

Frolov, A. D. and Macheret, Y. Y. (1999). On dielectric properties of dry and wet snow. Hydrological Processes, 13(12-13):1755–1760.

Fuchs, M., Bolshiyanov, D., Grigoriev, M., Morgenstern, A., Pesttryakova, L., Tsibizov, L., and Dill, A. (2021). Russian-German Cooperation: Expeditions to Siberia in 2019. Technical Report April, Alfred-Wegener-Institut Helmholtz-Zentrum fuer Polar- und Meeresforschung.

Gisnås, K., Etzelmüller, B., Farbrot, H., Schuler, T. V., and Westermann, S. (2013). CryoGRID 1.0: Permafrost Distribution in Norway estimated by a Spatial Numerical Model. Permafrost and Periglacial Processes, 24:2–19.

Gouttevin, I., Langer, M., Löwe, H., Boike, J., Proksch, M., and Schneebeli, M. (2018). Observation and modelling of snow at a polygonal tundra permafrost site: Spatial variability and thermal implications. The Cryosphere, 12(11):3693–3717.

Gouttevin, I., Menegoz, M., Dominé, F., Krinner, G., Koven, C., Ciais, P., Tarnocai, C., and Boike, J. (2012). How the insulating properties of snow affect soil carbon distribution in the continental pan-Arctic area. Journal of Geophysical Research: Biogeosciences, 117(2).

Grigoriev, M. (1993). Cryomorphogenesis in the Lena Delta (in Russian). Permafrost Institute Press, Yakutsk.

Grünberg, I., Wilcox, E. J., Zwieback, S., Marsh, P., and Boike, J. (2020). Linking tundra vegetation, snow, soil temperature, and permafrost. Biogeosciences, 17(16):4261–4279.

Huebner, C. (1999). Forschungszentrum Karlsruhe Entwicklung hochfrequenter Meeverfahren zur Boden-und Schneefeuchtebestimmung. Technical report, Institut für Meteorologie und Klimaforschung.

Jorgenson, M. T., Romanovsky, V., Harden, J., Shur, Y., O'Donnell, J., Schuur, E. A., Kanevskiy, M., and Marchenko, S. (2010). Resilience and vulnerability of permafrost to climate change. Canadian Journal of Forest Research, 40:1219–1236.

Jorgenson, M. T. and Shur, Y. (2007). Evolution of lakes and basins in northern Alaska and discussion of the thaw lake cycle. Journal of Geophysical Research, 112(F2):F02S17.

Koven, C. D., Schuur, E. A., Schädel, C., Bohn, T. J., Burke, E. J., Chen, G., Chen, X., Ciais, P., Grosse, G., Harden, J. W., Hayes, D. J., Hugelius, G., Jafarov, E. E., Krinner, G., Kuhry, P., Lawrence, D. M., MacDougall, A. H., Marchenko, S. S., McGuire, A. D., Natali, S. M., Nicolsky, D. J., Olefeldt, D., Peng, S., Romanovsky, V. E., Schaefer, K. M., Strauss, J., Treat, C. C., and Turetsky, M. (2015). A simplified, data-constrained approach to estimate the permafrost carbon-climate feedback. Philosophical Transactions of the Royal Society A: Mathematical, Physical and Engineering Sciences, 373(2054).

Krinner, G., Derksen, C., Essery, R., Flanner, M., Hagemann, S., Clark, M., Hall, A., Rott, H., Brutel-Vuilmet, C., Kim, H., Ménard, C. B., Mudryk, L., Thackeray, C., Wang, L., Arduini, G., Balsamo, G., Bartlett, P., Boike, J., Boone, A., Chéruy, F., Colin, J., Cuntz, M., Dai, Y., Decharme, B., Derry, J., Ducharne, A., Dutra, E., Fang, X., Fierz, C., Ghattas, J., Gusev, Y., Haverd, V., Kontu, A., Lafaysse, M., Law, R., Lawrence, D., Li, W., Marke, T., Marks, D., Ménégoz, M., Nasonova, O., Nitta, T., Niwano, M., Pomeroy, J., Raleigh, M. S., Schaedler, G., Semenov, V., Smirnova, T. G., Stacke, T., Strasser, U., Svenson, S., Turkov, D., Wang, T., Wever, N., Yuan, H., Zhou, W., and Zhu, D. (2018). ESM-SnowMIP: Assessing snow models and quantifying snow-related climate feedbacks. Geoscientific Model Development, 11(12):5027–5049.

Langer, M., Westermann, S., Heikenfeld, M., Dorn, W., and Boike, J. (2013). Satellite-based modeling of permafrost temperatures in a tundra lowland landscape. Remote Sensing of Environment, 135:12–24.

Mackay, J. R. (2000). Thermally induced movements in ice-wedge polygons, western arctic coast: A long-term study. Geographie Physique et Quaternaire, 54(1):41–68.

Meredith, M., M. Sommerkorn, S. Cassotta, C. Derksen, A. Ekaykin, A. Hollowed, G. Kofinas, A. Mackintosh, J. Melbourne-Thomas, M.M.C. Muelbert, G. Ottersen, H. Pritchard, and and E.A.G. Schuur (2019). IPCC Special Report on the Ocean and Cryosphere in a Changing Climate.

Mudryk, L., Santolaria-Otín, M., Krinner, G., Ménégoz, M., Derksen, C., Brutel-Vuilmet, C., Brady, M., and Essery, R. (2020). Historical Northern Hemisphere snow cover trends and projected changes in the CMIP6 multi-model ensemble. The Cryosphere, 14(7):2495–2514.

Muster, S., Langer, M., Heim, B., Westermann, S., and Boike, J. (2012). Subpixel heterogeneity of ice-wedge polygonal tundra: a multi-scale analysis of land cover and evapotranspiration in the Lena River Delta, Siberia. Tellus B: Chemical and Physical Meteorology, 64(1):17301.

Nitzbon, J., Langer, M., Martin, L. C., Westermann, S., Schneider Von Deimling, T., and Boike, J. (2021). Effects of multi-scale heterogeneity on the simulated evolution of ice-rich permafrost lowlands under a warming climate. The Cryosphere, 15(3):1399–1422.

Nitzbon, J., Langer, M., Westermann, S., Martin, L., Aas, K. S., and Boike, J. (2019). Pathways of ice-wedge degradation in polygonal tundra under different hydrological conditions. The Cryosphere, 13(4):1089–1123.

Nitzbon, J., Westermann, S., Langer, M., Martin, L. C., Strauss, J., Laboor, S., and Boike, J. (2020). Fast response of cold ice-rich permafrost in northeast Siberia to a warming climate. Nature Communications, 11(1):2201.

Obu, J. (2021). How Much of the Earth's Surface is Underlain by Permafrost? Journal of Geophysical Research: Earth Surface, 126(5):e2021JF006123.

Obu, J., Westermann, S., Bartsch, A., Berdnikov, N., Christiansen, H. H., Dashtseren, A., Delaloye, R., Elberling, B., Etzelmüller, B., Kholodov, A., Khomutov, A., Kääb, A., Leibman, M. O., Lewkowicz, A. G., Panda, S. K., Romanovsky, V., Way, R. G., Westergaard-Nielsen, A., Wu, T., Yamkhin, J., and Zou, D. (2019). Northern Hemisphere permafrost map based on TTOP modelling for 2000 - 2016 at 1km2 scale. Earth-Science Reviews, 193:299–316.

Olefeldt, D., Goswami, S., Grosse, G., Hayes, D., Hugelius, G., Kuhry, P., Mcguire, A. D., Romanovsky, V. E., Sannel, A. B., Schuur, E. A., and Turetsky, M. R. (2016). Circumpolar distribution and carbon storage of thermokarst landscapes. Nature Communications, 7:13043.

Osterkamp, T. E., Jorgenson, M. T., Schuur, E. A., Shur, Y. L., Kanevskiy, M. Z., Vogel, J. G., and Tumskoy, V. E. (2009). Physical and ecological changes associated with warming permafrost and thermokarst in Interior Alaska. Permafrost and Periglacial Processes, 20:235–256.

Outcalt, S. I., Nelson, F. E., and Hinkel, K. M. (1990). The zero-curtain effect: Heat and mass transfer across an isothermal region in freezing soil. Water Resources Research, 26(7):1509– 1516.

Overduin, P. P., Schneider von Deimling, T., Miesner, F., Grigoriev, M. N., Ruppel, C., Vasiliev, A., Lantuit, H., Juhls, B., and Westermann, S. (2019). Submarine Permafrost Map in the Arctic Modeled Using 1-D Transient Heat Flux (SuPerMAP). Journal of Geophysical Research: Oceans, 124(6):3490–3507.

Pepin, N., Bradley, R. S., Diaz, H. F., Baraer, M., Caceres, E. B., Forsythe, N., Fowler, H., Greenwood, G., Hashmi, M. Z., Liu, X. D., Miller, J. R., Ning, L., Ohmura, A., Palazzi, E., Rangwala, I., Schöner, W., Severskiy, I., Shahgedanova, M., Wang, M. B., Williamson, S. N., and Yang, D. Q. (2015). Elevation-dependent warming in mountain regions of the world. Nature Climate Change, 5:424–430.

Proksch, M., Rutter, N., Fierz, C., and Schneebeli, M. (2016). Intercomparison of snow density measurements: bias, precision, and vertical resolution. The Cryosphere, 10:371–384.

Riche, F. and Schneebeli, M. (2013). Thermal conductivity of snow measured by three independent methods and anisotropy considerations. The Cryosphere, 7(1):217–227.

Roth, K., Schulin, R., Flühler, H., and Attinger, W. (1990). Calibration of Time Domain Reflectometry for Water Content Measurement Using a Composite Dielectric Approach. Water Resources Research, 26(10):2267–2273.

Royer, A., Domine, F., Roy, A., Langlois, A., Marchand, N., and Davesne, G. (2021a). New northern snowpack classification linked to vegetation cover on a latitudinal mega-transect across northeastern Canada New northern snowpack classification linked to vegetation cover on a latitudinal mega-transect across northeastern Canada. Écoscience, 28(3-4):225–242.

Royer, A., Picard, G., Vargel, C., Langlois, A., Gouttevin, I., and Dumont, M. (2021b). Improved Simulation of Arctic Circumpolar Land Area Snow Properties and Soil Temperatures. Frontiers in Earth Science, 9:2296–6463.

Schennen, S., Schwamborn, G., Zubrzycki, S., and Bornemann, N. (2016). Orthomosaic of Samoylov Island (south), Siberia, Spring 2015, University of Potsdam. PANGAEA.

Schneider, J., Grosse, G., and Wagner, D. (2009). Land cover classification of tundra environments in the Arctic Lena Delta based on Landsat 7 ETM+ data and its application for upscaling of methane emissions. Remote Sensing of Environment, 113(2):380–391.

Schwamborn, G., Rachold, V., and Grigoriev, M. N. (2002). Late Quaternary sedimentation history of the Lena Delta. Quaternary International, 89:119–134.

Slater, A. G., Lawrence, D. M., and Koven, C. D. (2017). Process-level model evaluation: A snow and heat transfer metric. Cryosphere, 11(2):989–996.

Smith, M. W. and Burn, C. R. (1987). Outward flux of vapour from frozen soils at Mayo, Yukon, Canada: Results and interpretation. Cold Regions Science and Technology, 13:143–152.

Sokratov, S. A. and Barry, R. G. (2002). Intraseasonal variation in the thermoinsulation effect of snow cover on soil temperatures and energy balance. Journal of Geophysical Research: Atmospheres, 107(D10):ACL 13 1–ACL 13 6.

Sommer Messtechnik (2016). Snow Pack Analyser SPA-2 Analysing system User Manual. Technical report, SOMMER GmbH.

Stacheder, M. (2005). TDR and low-frequency measurements for continuous monitoring of moistureand density in a snow pack. International Agrophysics, 19:75–78.

Staehli, M., Stacheder, M., Gustafsson, D., Schlaeger, S., Schneebeli, M., and Brandelik, A. (2004). A new in situ sensor for large-scale snow-cover monitoring. Annals of Glaciology, 38:273–278.

Stiegler, C., Lund, M., Christensen, T. R., Mastepanov, M., and Lindroth, A. (2016). Two years with extreme and little snowfall: Effects on energy partitioning and surface energy exchange in a high-Arctic tundra ecosystem. The Cryosphere, 10(4):1395–1413.

Sturm, M. and Benson, C. (2004). Scales of spatial heterogeneity for perennial and seasonal snow layers. Annals of Glaciology, 38:253–260.

Sturm, M. and Benson, C. S. (1997). Vapor transport, grain growth and depth-hoar development in the subarctic snow. Journal of Glaciology, 43(143):42–58.

Sturm, M., Holmgren, J., Konig, M., and Morris, K. (1997). The thermal conductivity of seasonal snow. Journal of Glaciology, 43(143):26–41.

Sturm, M. and Johnson, J. B. (1991). Natural convection in the subarctic snow cover. Journal of Geophysical Research, 96(B7):11657–11671.

Sturm, M. and Johnson, J. B. (1992). Thermal conductivity measurements of depth hoar. Journal of Geophysical Research: Solid Earth, 97(B2):2129– 2139.

Sturm, M., McFadden, J. P., Liston, G. E., Stuart Chapin, F., Racine, C. H., and Holmgren, J. (2001). Snow-shrub interactions in Arctic Tundra: A hypothesis with climatic implications. Journal of Climate, 14(3):336–344.

Van Everdingen, R. O. (1998). Multi-language glossary of permafrost and related ground-ice terms (Rev. ed. 2005). International Permafrost Association.

Vionnet, V., Brun, E., Morin, S., Boone, A., Faroux, S., Le Moigne, P., Martin, E., and Willemet, J. M. (2012). The detailed snowpack scheme Crocus and its implementation in SURFEX v7.2. Geoscientific Model Development, 5(3):773–791.

Wainwright, H. M., Liljedahl, A. K., Dafflon, B., Ulrich, C., Peterson, J. E., Gusmeroli, A., and Hubbard, S. S. (2017). Mapping snow depth within a tundra ecosystem using multiscale observations and Bayesian methods. The Cryosphere, 11(2):857–875.

Westermann, S., Aalstad, K., Zweigel, R. B., Renette, C., Schmidt, L. S., Aga, J., Nitzbon, J., Angelopoulos, M., Stuenzi, S. M., Chaudhary, N., Miesner, F., Martin, L., Morard, S., Ben-Asher, M., Kääb, A., Ingeman-Nielsen, T., Groenke, B., Boike, J., Scheer, J., Overduin, P., Filhol, S., and Langer, M. (2022). The CryoGrid community model (version 1.0) – a multi-physics toolbox for climate-driven simulations in the terrestrial cryosphere. The Cryosphere, 2022:1–61.

Westermann, S. and Langer, M. (2014). CryoGrid 3-Model description.

Westermann, S., Langer, M., Boike, J., Heikenfeld, M., Peter, M., Etzelmüller, B., and Krinner, G. (2016). Simulating the thermal regime and thaw processes of ice-rich permafrost ground with the land-surface model CryoGrid 3. Geoscientific Model Development, 9(2):523–546.

Westermann, S., Schuler, T. V., Gisnas, K., and Etzelmüller, B. (2013). Transient thermal modeling of permafrost conditions in Southern Norway. The Cryosphere, 7(2):719–739.

Wicky, J. and Hauck, C. (2020). Air Convection in the Active Layer of Rock Glaciers. Frontiers in Earth Science, 8:335.

Woo, M.-K. (1982). Upward flux of vapor from frozen materials in the high Arctic. Cold Regions Science and Technology, 5:269–274.

Yen, Y. C. (1981). Review of thermal properties of snow, ice and sea ice. CRREL Report (US Army Cold Regions Research and Engineering Laboratory), 81-10.

Yershov, E. D., Kondrat'yeva, K. A., Loginov, V. F., and Sychev, I. K. (1991). Geocryological Map of Russia and Neighbouring Republics, Faculty of Geology, Chair of Geocryology, LomonosovMoscow State University.

Zhang, T. (2005). Influence of the seasonal snow cover on the ground thermal regime: An overview. Reviews of Geophysics, 43.

Zhang, T., Barry, R. G., Knowles, K., Heginbottom, J. A., and Brown, J. (2008). Statistics and characteristics of permafrost and ground-ice distribution in the Northern Hemisphere. Polar Geography, 31:47–68.

Zhang, T., Osterkamp, T. E., and Stamnes, K. (1996). Influence of the depth hoar layer of the seasonal snow cover on the ground thermal regime. Water Resources Research, 32(7):2075–2086.

Zubrzycki, S., Kutzbach, L., Grosse, G., and Desyatkin, A. (2013). Organic carbon and total nitrogen stocks in soils of the Lena River Delta. Biogeosciences, 10(6):3507–3524.

Zweigel, R. B., Westermann, S., Nitzbon, J., Langer, M., Boike, J., Etzelmüller, B., and Vikhamar Schuler, T. (2021). Simulating Snow Redistribution and its Effect on Ground Surface Temperature at a High-Arctic Site on Svalbard. Journal of Geophysical Research: Earth Surface, 126(3):e2020JF005673.

Zyungo Yosida (1955). Physical Studies on Deposited Snow. 1.* Thermal Properties. Contributions from the Institute of Low Temperature Science, 7:19–74.

A Appendices

A.1 Validation data 2018

Table 7: Field measurements snow density spring campaign 2018 (part 1). Measurements were conducted in a 25 m polygon complex located at 72°22.223′ N and 126°28.956′ E. Data deployment: Dr. Hanno Meyer (AWI).

UTC	snow depth [cm]	density [kgm^{-3}]	UTC	snow depth [cm]	density [kgm^{-3}]
19.04.18	19	314	25.04.18	44	259
19.04.18	30	355	25.04.18	48	299
19.04.18	20.5	344	25.04.18	37.5	316
19.04.18	17	267	25.04.18	28	246
19.04.18	29	217	25.04.18	50	0
19.04.18	30	288	25.04.18	58	322
19.04.18	28	283	25.04.18	47	287
19.04.18	28.5	325	25.04.18	46.5	257
19.04.18	31	261	25.04.18	55	219
19.04.18	32	263	25.04.18	50	293
19.04.18	33.1	260	25.04.18	47	295
19.04.18	28	265	25.04.18	50	323
19.04.18	26	205	25.04.18	45.5	274
19.04.18	24	210	25.04.18	43	309
19.04.18	23.5	312	25.04.18	46	310
19.04.18	24.5	303	25.04.18	47	307
19.04.18	27	245	25.04.18	46	296
19.04.18	20	0	25.04.18	29	214
19.04.18	17	262	25.04.18	10	205
19.04.18	10	228	25.04.18	10	220
19.04.18	9	299	25.04.18	14.5	508
19.04.18	10	464	25.04.18	13	360

Table 8: Field measurements snow density spring campaign 2018 (part 2). Measurements were conducted in a 25 m polygon complex located at 72°22.223′ N and 126°28.956′ E. Data deployment: Dr. Hanno Meyer (AWI).

UTC	**snow depth** [cm]	**density** [kgm^{-3}]	**UTC**	**snow depth** [cm]	**density** [kgm^{-3}]
02.05.18	39	298	09.05.18	41	249
02.05.18	44	324	09.05.18	41	271
02.05.18	30	355	09.05.18	33	268
02.05.18	26	345	09.05.18	24	316
02.05.18	49.5	351	09.05.18	46	271
02.05.18	62	317	09.05.18	59	287
02.05.18	54	290	09.05.18	52	296
02.05.18	54	325	09.05.18	52	353
02.05.18	56.5	319	09.05.18	54	294
02.05.18	51	323	09.05.18	50	326
02.05.18	50	346	09.05.18	46	350
02.05.18	51	332	09.05.18	53	325
02.05.18	47.5	333	09.05.18	47	325
02.05.18	46	329	09.05.18	44	309
02.05.18	50	254	09.05.18	48	311
02.05.18	55.5	310	09.05.18	56	338
02.05.18	53	302	09.05.18	49	279
02.05.18	26.5	281	09.05.18	26	232
02.05.18	7	272	09.05.18	9	145
02.05.18	9	238	09.05.18	4.5	183
02.05.18	13	286	09.05.18	7	423
02.05.18	15	378	09.05.18	16	378

A.2 Air temperature

Table 9: Two-tailed t-test for significant differences in the measured air temperatures in 2014/2015 compared to all other seasons. Testing period from 1 September to 15 June of each season.

Testing period (01.10-15.06.)	**p-value**	**significance at p <.05**
1415/1516	0.64	no
1415/1617	0.49	no
1415/1718	0.96	no

A.3 Forcing data

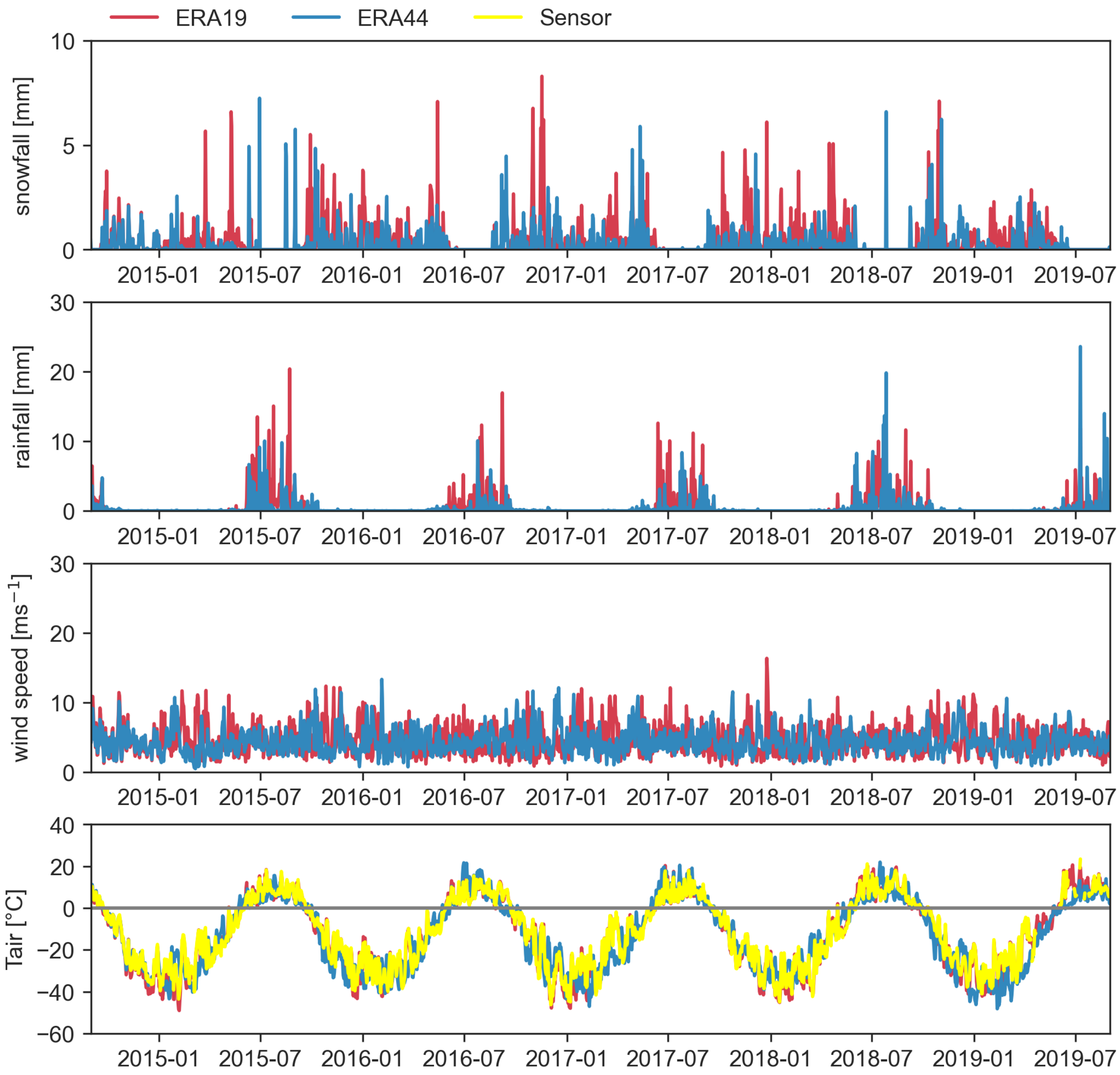

Figure 34: Comparison of the forcing data ERA19 (red) and ERA44 (blue) for snowfall, rainfall and wind speed from 2014 to 2019. The temperature plot also includes measured air temperatures at the snow station in 0.8 m height. The grey line indicates 0 °C. The RMSE (MBE) in air temperature for the ERA19 forcing was 2.7 (–0.7) K. The RMSE (MBE) in air temperature for the ERA44 forcing was 7.8 (–1.6) K. Reference data: T_{air} from the sensor in 0.8 m height.

A.4 Lists of data sets, scripts and parameters

Data sets: data_scripts_thesis

- **Full data sets:** available on request (julia.boike@awi.de)

- snow station (A_SENSOR_DATA_snow_station_2012_2021.csv)
- soil station (B_SENSOR_DATA_SaSoil2012_2021_lv1_vwc_offset.txt)
- field campaign 2019 (C_SENSOR_DATA_validation_2019.csv)
- field campaign 2018 (D_SENSOR_DATA_validation_2018.csv9
- ALTD measurements CALM grid (E_CALM_DATA_Complete_SaCalm2002_2021_lv1_final.txt)

Data processing: data_scripts_thesis

- 00_SENSOR_SCRIPT_snow_temperature_gradient.ipynb
- 01_SENSOR_SCRIPT_snowdepth_2014_2020.ipynb
- 02_SENSOR_SCRIPT_Tgrad_and_density_2016_2020.ipynb
- 03_SENSOR_SCRIPT_density_SWE_keff_2014_2020.ipynb
- 04_SENSOR_SCRIPT_density_Tsoil_scatter.ipynb
- 05_SENSOR_SCRIPT_thermal_profile_snow_soil.ipynb
- 06_SENSOR_MODEL_CALM_grid_ALT

CG runs: CG_Output

- CG Standard Crocus ERA19 parameter file (12_1D_yen_ERA19_Samoylov_cen.xlsx)
- CG Standard Crocus ERA44 parameter file (15_1D_yen_ERA44_Samoylov_FC05.xlsx)

- CG Arctic Crocus ERA19 parameter file
  (17_1D_arctic_ERA19_Samoylov_FC05.xlsx)
- constants file: same for each run (CONSTANTS_excel.xlsx)
- forcing data ERA19 (Samoylov_T0_ERAint_1979_2019.mat)
- forcing data ERA44
  (samoylov_ERA_obs_fitted_1979_2014_spinup_extended2044.mat)

CG Output: CG_Output
(xx needs to be replaced with run number 12, 15 or 17)

- read out Matlab output
  (00_READ_OUT_CG_OUTPUT_MATLAB.txt)
- density (xx_CG_density.ipynb)
- temperature (xx_CG_temperature.ipynb)

Model validation: CG_VS_sensor
(xx needs to be replaced with run number 12, 15 or 17)

- RMSE and MBE: density, depth, temperature
  (01_xx_RMSE_modelVSsensor.ipynb)
- density model/sensor
  (02_xx_DENSITY_CG_vs_sensor.ipynb)
- snow depth model/sensor
  (03_snowdepth_model_sensor.ipynb)
- temperature model/sensor
  (xx_TEMPERATURE_CG_vs_sensor.ipynb)

Table 10: List of parameters with units and descriptions. Only modelling parameters were listed which were adjusted for each model run.

symbol	unit	description
snow depth	m	snow depth
EOS snow depth	m	end-of-season snow depth (15 April to 15 May)
z_{centre}	m	snow depth LCP centre (only the five centre depth sensors)
thaw depth	m	ALTD; end-of-season active layer thaw depth
ρ	$\mathrm{kg\,m^{-3}}$	snow density
ρ_{bulk}	$\mathrm{kg\,m^{-3}}$	average bulk density in 0.05, 0.15 and 0.25 m height (SPA-2 strap sensors)
EOS ρ_{bulk}	$\mathrm{kg\,m^{-3}}$	end-of-season ρ_{bulk} (15 April to 15 May)
$\mathrm{SWE_{bulk}}$	mm	average bulk SWE calculated with ρ_{bulk}
EOS $\mathrm{SWE_{bulk}}$	mm	end-of-season $\mathrm{SWE_{bulk}}$ (15 April to 15 May)
ρ_{TDR}	$\mathrm{kg\,m^{-3}}$	snow density calculated from TDR measurements
ϵ	$\mathrm{F\,m^{-1}}$	dielectric permittivity
T	℃	snow temperature
T_{grad}	K	temperature gradient between T_{air} (0.8 m height) and T_{soil} (0.05 m depth)
T_{soil}	℃	soil temperature
T_{air}	℃	air temperature
T_{diff}	K	difference measured snow temperature and modeled snow temperature

symbol	**unit**	**description**
k_{yen}	$W\,m^{-1}\,K^{-1}$	thermal conductivity following equation by Yen (1981)
k_{sturm}	$W\,m^{-1}\,K^{-1}$	thermal conductivity following equation by Sturm et al. (1997)
θ_m		volumetric mineral content
θ_o		volumetric organic content
θ_w		volumetric water content
θ_i		volumetric ice content
θ_{fc}		field capacity
Φ		porosity

Erklärung gem. §10 Abs. 11 Allg. Teil d. Master-PO vom 27.10.2010

Ich versichere hiermit, dass ich meine Masterarbeit selbständig verfasst und keine anderen als die angegebenen Quellen und Hilfsmittel benutzt habe. Wörtliche oder dem Sinn nach aus anderen Werken entnommene Stellen sind unter Angabe der Quellen kenntlich gemacht.

Die Arbeit wurde nicht in einem anderen Prüfungsverfahren eingereicht.

Weiterhin erkläre ich, dass die Masterarbeit in unveränderter Fassung der Öffentlichkeit **zur Verfügung** / nicht zur Verfügung* gestellt werden kann.

*Zutreffendes bitte markieren

Ort/Datum: **Berlin, 2022-07-22**

Unterschrift: Julia Martin